



NAVAL
POSTGRADUATE
SCHOOL

MONTEREY, CALIFORNIA

THESIS

**GRAIN SIZE CONTROL IN AA5083 BY
THERMOMECHANICAL PROCESSING (TMP): THE
ROLE OF DISPERSED PARTICLES**

by

Ramiro E. Orellano, Jr.

September 2003

Thesis Advisor:

Terry R. McNelley

Approved for public release; distribution is unlimited

THIS PAGE INTENTIONALLY LEFT BLANK

REPORT DOCUMENTATION PAGE			<i>Form Approved OMB No. 0704-0188</i>	
Public reporting burden for this collection of information is estimated to average 1 hour per response, including the time for reviewing instruction, searching existing data sources, gathering and maintaining the data needed, and completing and reviewing the collection of information. Send comments regarding this burden estimate or any other aspect of this collection of information, including suggestions for reducing this burden, to Washington headquarters Services, Directorate for Information Operations and Reports, 1215 Jefferson Davis Highway, Suite 1204, Arlington, VA 22202-4302, and to the Office of Management and Budget, Paperwork Reduction Project (0704-0188) Washington DC 20503.				
1. AGENCY USE ONLY (Leave blank)		2. REPORT DATE September 2003	3. REPORT TYPE AND DATES COVERED Master's Thesis	
4. TITLE AND SUBTITLE: Grain Size Control in AA5083 by Thermomechanical Processing (TMP): The Role of Dispersed Particles			5. FUNDING NUMBERS	
6. AUTHOR(S) Ramiro E. Orellano, Jr.				
7. PERFORMING ORGANIZATION NAME(S) AND ADDRESS(ES) Naval Postgraduate School Monterey, CA 93943-5000			8. PERFORMING ORGANIZATION REPORT NUMBER	
9. SPONSORING /MONITORING AGENCY NAME(S) AND ADDRESS(ES) General Motors Corp., Research and Development Center, Warren, MI (Dr. Paul E. Krajewski, Technical Program Monitor), under subcontract with Univ. of Texas-Austin (Prof. Eric Taleff)			10. SPONSORING/MONITORING AGENCY REPORT NUMBER	
11. SUPPLEMENTARY NOTES The views expressed in this thesis are those of the author and do not reflect the official policy or position of the Department of Defense or the U.S. Government.				
12a. DISTRIBUTION / AVAILABILITY STATEMENT Approved for public release; distribution is unlimited			12b. DISTRIBUTION CODE	
13. ABSTRACT (maximum 200 words) <p>Superplasticity in Aluminum alloys allows for the economical forming of components of complex shapes while retaining the high-strength and stiffness-to-weight ratios characteristic of alloys used in automotive, aerospace and military applications. Superplastic materials require fine grains with high-angle boundaries having resistance to failure by cavitation. This study was designed to achieve improved control of microstructure of Continuously Cast (CC) AA 5083 utilizing the Particle Stimulated Nucleation (PSN) model as a guide. The studies included a variety of overaging parameters in the thermomechanical process (TMP), followed by a constant processing strain and a subsequent recrystallization annealing treatment. The resulting material was analyzed using optical microscopy, and backscatter electron (BSE) and orientation imaging microscopy (OIM) methods to evaluate the effect of the processing on the grain size and the dispersion of particles.</p>				
14. SUBJECT TERMS Superplasticity, Grain Size Control, Second Phase Particles, Grain Boundary Sliding, Particle Stimulated Nucleation (PSN), AA 5083			15. NUMBER OF PAGES 109	
			16. PRICE CODE	
17. SECURITY CLASSIFICATION OF REPORT Unclassified	18. SECURITY CLASSIFICATION OF THIS PAGE Unclassified	19. SECURITY CLASSIFICATION OF ABSTRACT Unclassified	20. LIMITATION OF ABSTRACT UL	

NSN 7540-01-280-5500

Standard Form 298 (Rev. 2-89)
Prescribed by ANSI Std. Z39-18

THIS PAGE INTENTIONALLY LEFT BLANK

Approved for public release; distribution is unlimited

**GRAIN SIZE CONTROL BY THERMOMECHANICAL PROCESSING (TMP):
THE ROLE OF DISPERSED PARTICLES**

Ramiro E. Orellano, Jr.
Lieutenant, United States Navy
B.S., San Diego State University, 1997

Submitted in partial fulfillment of the
requirements for the degree of

MASTER OF SCIENCE IN MECHANICAL ENGINEERING

from the

**NAVAL POSTGRADUATE SCHOOL
September 2003**

Author: Ramiro E. Orellano, Jr.

Approved by: Terry R. McNelley
Thesis Advisor

Anthony J. Healey
Chairman, Department of Mechanical and Astronautical
Engineering

THIS PAGE INTENTIONALLY LEFT BLANK

ABSTRACT

Superplasticity in Aluminum alloys allows for the economical forming of components of complex shapes while retaining the high-strength and stiffness-to-weight ratios characteristic of alloys used in automotive, aerospace and military applications. Superplastic materials require fine grains with high-angle boundaries having resistance to failure by cavitation. This study was designed to achieve improved control of microstructure of Continuously Cast (CC) AA 5083 utilizing the Particle Stimulated Nucleation (PSN) model as a guide. The studies included a variety of overaging parameters in the thermomechanical process (TMP), followed by a constant processing strain and a subsequent recrystallization annealing treatment. The resulting material was analyzed using optical microscopy, and backscatter electron (BSE) and orientation imaging microscopy (OIM) methods to evaluate the effect of the processing on the grain size and the dispersion of particles.

THIS PAGE INTENTIONALLY LEFT BLANK

TABLE OF CONTENTS

I.	INTRODUCTION.....	1
II.	BACKGROUND	5
	A. SUPERPLASTICITY AND DEFORMATION MECHANISMS	5
	B. COMMON FEATURES OF SUPERPLASTICITY	10
	C. PARTICLE STIMULATED NUCLEATION (PSN) THEORY	11
	D. RESEARCH AT NPS	15
III.	EXPERIMENTAL PROCEDURE.....	17
	A. MATERIAL.....	17
	B. PROCESSING.....	17
	C. METALLOGRAPHIC SAMPLE PREPARATION	21
	D. OPTICAL MICROSCOPY.....	23
	E. ORIENTATION IMAGING MICROSCOPY	23
	F. BACKSCATTER ELECTRON IMAGING	25
IV.	RESULTS AND DISCUSSION	27
	A. ROLE OF PARTICLES IN PSN.....	27
	1. G1CC Texture and Grain-to-grain Orientations.....	27
	2. Optical Microscopy	30
	3. Backscatter Electron (BSE) Imaging	32
	4. Particle Fractions and Particle Size Studies.....	34
	B. EFFECTS OF ANNEALING ON GRAIN SIZE CONTROL.....	39
	1. Backscatter Electron (BSE) Imaging	39
	2. Grain Size Study	41
	3. Orientation Imaging Microscopy (OIM)	44
	C. PARTICLES AND GRAINS WITHIN THE SCHEME OF PSN.....	47
	1. Heat Treatments and the Al-Mn Binary Phase Diagram.....	47
	2. Volume Fraction Studies	48
	3. Particle Spacing within the PSN Model.....	52
	4. Particle Distributions and the Critical Particle Size.....	52
V.	CONCLUSION	55
	A. CONCLUSION	55
	B. RECOMMENDATIONS FOR FURTHER STUDY	56
APPENDIX A.	OPTICAL MICROSCOPY.....	57
APPENDIX C.	PARTICLE FRACTION CHARTS (PARTICLES)	69
APPENDIX D.	BSE IMAGES (GRAINS).....	73
APPENDIX E.	BSE GRAIN SIZE CHARTS.....	77
APPENDIX G.	OIM GRAIN SIZE CHARTS	85
	LIST OF REFERENCES	89
	INITIAL DISTRIBUTION LIST	93

THIS PAGE INTENTIONALLY LEFT BLANK

LIST OF FIGURES

Figure 1.	Gas-pressure Forming of Superplastic Aluminum Sheet Material [Ref. 55].....	3
Figure 2.	Schematic plot of log (strain rate) vs. log (stress) [Ref. 56]	6
Figure 3.	Al-Mg Phase Diagram [Ref. 45]	9
Figure 4.	Al-Mn Phase Diagram [Ref. 45]	9
Figure 5.	Particles of diameter d_p (Region 1) and Deformation Zones (Region 2).....	12
Figure 6.	Deformation width, critical particle size and interval λ	12
Figure 7.	Recrystallized grain size formed by PSN of grains given as $d_g \approx \lambda/2$	13
Figure 8.	Effect of cold-rolling reduction on the critical particle size	14
Figure 9.	Thermomechanical Processing Steps.....	18
Figure 10.	AA 5083 Heat Treatment History	20
Figure 11.	Sample Orientation and Camera position	23
Figure 12.	Euler Angle Orientation and Direction	24
Figure 13.	KBD Pattern (before and after indexing).....	26
Figure 14.	Textures of Sample R and Sample Z	28
Figure 15.	Misorientation Angles for Sample R and Sample Z	29
Figure 16.	G1CC, As-Cast and Hot Band materials prior to TMP	31
Figure 17.	Optical Micrographs of G1CC As-cast and Hotband Materials	31
Figure 18.	BSE images. Second Phase. Samples R and Z	33
Figure 19.	Particle Fractions for Samples R and Z	35
Figure 20.	Particle Sizes for all samples with standard error bars	37
Figure 21.	Grain Size measurements along major and minor diameters.....	39
Figure 22.	BSE images of Grains in Samples R and Z	40
Figure 23.	Grain Size Results of BSE Imaging.....	42
Figure 24.	OIM images. Grayscaled Grain Maps. Samples R and Z	45
Figure 25.	Grain Size Results of OIM Scans	46
Figure 26.	Al-Mn Phase Diagram with Aging Temperatures	47
Figure 27.	Phase Diagram Volume Fraction of Particles	49
Figure 28.	Volume Fraction vs. Final Grain Size.....	49
Figure 29.	Increased strain to decrease d_p^*	52
Figure 30.	Theoretical Precipitate Distributions	53
Figure 31.	Superimposed Particle Fractions.....	54
Figure 32.	Sample T. Aged 500° C, 100 hours. 750X.....	57
Figure 33.	Sample U. Aged 525° C, 1 hour. 750X.....	58
Figure 34.	Sample V. Aged 525° C, 10 hours. 750X	58
Figure 35.	Sample W. Aged 525° C, 10 hour. 750X.....	59
Figure 36.	Sample X Aged 550° C, 1 hour. 750X.....	59
Figure 37.	Sample Y. Aged 550° C, 10 hours. 750X	60
Figure 38.	Sample S. Aged 500° C, 10 hours, 80% CW, ReX. 1500X.....	60
Figure 39.	Sample T. Aged 500° C, 100 hours, 80% CW, ReX. 1500X.....	61
Figure 40.	Sample U. Aged 525° C, 1 hour, 80% CW, ReX. 1500X.....	61
Figure 41.	Sample V. Aged 525° C, 10 hours, 80% CW, ReX. 1500X	62

Figure 42.	Sample W. Aged 525° C, 100 hours, 80% CW, ReX. 1500X	62
Figure 43.	Sample X. Aged 550° C, 1 hour, 80% CW, ReX. 1500X.....	63
Figure 44.	Sample Y. Aged 550° C, 10 hours, 80% CW, ReX. 1500X	63
Figure 45.	Sample S. Aged 500° C, 10 hours. 1000X.....	65
Figure 46.	Sample T. Aged 500° C, 100 hours. 1000X.....	65
Figure 47.	Sample U. Aged 525° C, 1 hour. 1000X.....	66
Figure 48.	Sample V. Aged 525° C, 10 hours. 1000X	66
Figure 49.	Sample W. Aged 525° C, 10 hour. 1000X.....	67
Figure 50.	Sample X Aged 550° C, 1 hour. 1000X.....	67
Figure 51.	Sample Y. Aged 550° C, 10 hours. 1000X	68
Figure 52.	Sample S. Aged 500° C, 10 hours, 80% CW, ReX.....	69
Figure 53.	Sample T. Aged 525° C, 1 hour, 80% CW, ReX.	69
Figure 54.	Sample U. Aged 525° C, 1 hour, 80% CW, ReX.....	70
Figure 55.	Sample V. Aged 525° C, 10 hours, 80% CW, ReX	70
Figure 56.	Sample W. Aged 525° C, 100 hours, 80% CW, ReX.	71
Figure 57.	Sample X. Aged 550° C, 1 hour, 80% CW, ReX.....	71
Figure 58.	Sample Y. Aged 550° C, 10 hours, 80% CW, ReX.	72
Figure 59.	Sample S. Aged 500° C, 10 hours, 80% CW, ReX. 1000X.....	73
Figure 60.	Sample T. Aged 500° C, 100 hours, 80% CW, ReX	73
Figure 61.	Sample U. Aged 525° C, 1 hour, 80% CW, ReX. 1000X.....	74
Figure 62.	Sample V. Aged 525° C, 10 hours, 80% CW, ReX. 1000X	74
Figure 63.	Sample W. Aged 525° C, 100 hours, 80% CW, ReX. 1000X	75
Figure 64.	Sample X. Aged 550° C, 1 hour, 80% CW, ReX. 1000X.....	75
Figure 65.	Sample Y. Aged 550° C, 10 hours, 80% CW, ReX. 1000X	76
Figure 66.	Grain Size Comparison at 500° C, 80% CW, ReX.....	77
Figure 67.	Grain Size Comparison at 525° C, 80% CW, ReX.....	77
Figure 68.	Grain Size Comparison 550° C, 80% CW, ReX.....	78
Figure 69.	Grain Size Comparison for hour, 80% CW, ReX.....	78
Figure 70.	Grain Size Comparison for 10 hours, 80% CW, ReX	79
Figure 71.	Grain Size Comparison for 100 hours, 80% CW, ReX	79
Figure 72.	Sample S. Aged 500° C, 10 hours, 80% CW, ReX.....	81
Figure 73.	Sample T. Aged 500° C, 100 hours, 80% CW, ReX	81
Figure 74.	Sample U. Aged 525° C, 1 hour, 80% CW, ReX.....	82
Figure 75.	Sample V. Aged 525° C, 10 hours, 80% CW, ReX	82
Figure 76.	Sample W. Aged 525° C, 100 hours, 80% CW, ReX.	83
Figure 77.	Sample X. Aged 550° C, 1 hour, 80% CW, ReX.....	83
Figure 78.	Sample Y. Aged 550° C, 10 hours, 80% CW, ReX.....	84
Figure 79.	Sample S. Aged 500° C, 10 hours, 80% CW, ReX.....	85
Figure 80.	Sample T. Aged 500° C, 100 hours, 80% CW, ReX	86
Figure 81.	Sample U. Aged 525° C, 1 hour, 80% CW, ReX.....	86
Figure 82.	Sample V. Aged 525° C, 10 hours, 80% CW, ReX	87
Figure 83.	Sample W. Aged 525° C, 100 hours, 80% CW, ReX	87
Figure 84.	Sample X. Aged 550° C, 1 hour, 80% CW, ReX.....	88
Figure 85.	Sample Y. Aged 550° C, 10 hours, 80% CW, ReX	88

LIST OF TABLES

Table 1.	Aluminum Alloy AA 5083 (G1CC) Composition (Weight Percent)	17
Table 2.	Annealing Matrix	19
Table 3.	Mechanical Polishing.....	22
Table 4.	Volume Fractions acquired from Al-Mn Phase diagram.....	50
Table 5.	Particle Sizes and Grain Sizes from Volume Fraction Plot.....	50

THIS PAGE INTENTIONALLY LEFT BLANK

ACKNOWLEDGMENTS

The author wishes to extend his strongest appreciation to Professor Terry McNelley for his guidance during this work. The author would also like to thank Dr. Keichiro Oishi, Dr. Chan Park, Paul Green and Mary-Ann Kulas for their contributions.

Finally, the author wishes to recognize and thank his family, Karina, Andrew and Alexis Desiree, for their inspiration and support during the long hours dedicated to this project.

THIS PAGE INTENTIONALLY LEFT BLANK

I. INTRODUCTION

Superplasticity is a phenomenon whereby a polycrystalline metal exhibits extreme tensile ductility that is essentially isotropic, and deformation at relatively low stresses. An elongation of more than 200% is considered superplastic. An elongation of 1950% was first reported in 1934 for a Si-Bi alloy [Ref.1]. It was not until the 1960's, however, that research began in earnest in this field. Ductilities in excess of 5000% [Ref. 2] have been attained as the requirements for superplastic behavior and the associated processing and testing conditions have become better understood.

High tensile ductility suggests ease in forming and thus is the basis for practical application of this phenomenon. Superplasticity allows for complex shapes to be formed from a single sheet of superplastically processed material under specific fabricating conditions. This may enable designers to reduce the number of parts in an assembly by consolidation into fewer individual pieces. Forming methods are similar to gas-pressure molding of plastic sheet material; superplastic forming of an aluminum alloy sheet is illustrated in Figure 1. Parts consolidation may lead to a reduction in assembly time and lower manufacturing costs. Current military and space applications of superplastic forming include space shuttle external fuel tank components, landing gear doors for the B-1 bomber, various F/A-18A Hornet aircraft components, lightweight coolant piping, fire control radar dishes and aesthetic automotive parts.

Current processing methods to enable superplasticity are alloy specific and result in materials which require elevated temperatures with low forming rates. The most highly superplastic Al alloys require expensive alloy modifications and exhibit only moderate mechanical properties. Currently research seeks to devise superplastic processes that are economical and more widely applicable to existing commercially available Al alloys.

Weight reduction in structural components has also been of great concern. A reduction in weight while maintaining strength requirements generally results in a reduction in energy required to operate engineering systems. The substitution of aluminum alloys for steels is one method that will allow for weight savings. Ashby [Ref.

4] has developed methods for ranking and comparing materials for structural applications. For deflection-limited design of components subjected to flexure the substitution of aluminum for steel provides a theoretical 40% weight savings while the same substitution in a component subjected to a distributed load can provided a theoretical weight savings of 30%.

Commercial aluminum alloys are arguably the most important sheet material for superplastic forming operations. Some two-thirds of all gas-pressure-formed parts produced by Superform USA e.g., see [Ref. 5], a major producer of superplastically formed components, use AA 5083. This aluminum alloy has engendered great interest in the automotive industry due to its warm formability, corrosion resistance, weldability, and mechanical properties.

The initial part of this research is an investigation into the annealing response of continuously cast (CC) AA 5083 material in the hot band condition. Moderate superplastic behavior has been reported for this material. Several heat treatments were employed in an attempt to achieve controlled distributions of MnAl_6 constituent particles prior to deformation processing to enable a superplastic microstructure. The second part of the project attempts to create a microstructure through recrystallization treatments and achieve improved superplastic response with AA 5083. The heat treatments and deformation processing schedule were designed using Humphrey's particle stimulated nucleation (PSN) model as a guide. Analyzing the grain structures and the intermetallic particles, the material provided both qualitative and quantitative insights to engineering the desired material performance suitable for economical production.



Gas-pressure Forming of Superplastic Aluminum Sheet Material [Ref. 3]

THIS PAGE INTENTIONALLY LEFT BLANK

II. BACKGROUND

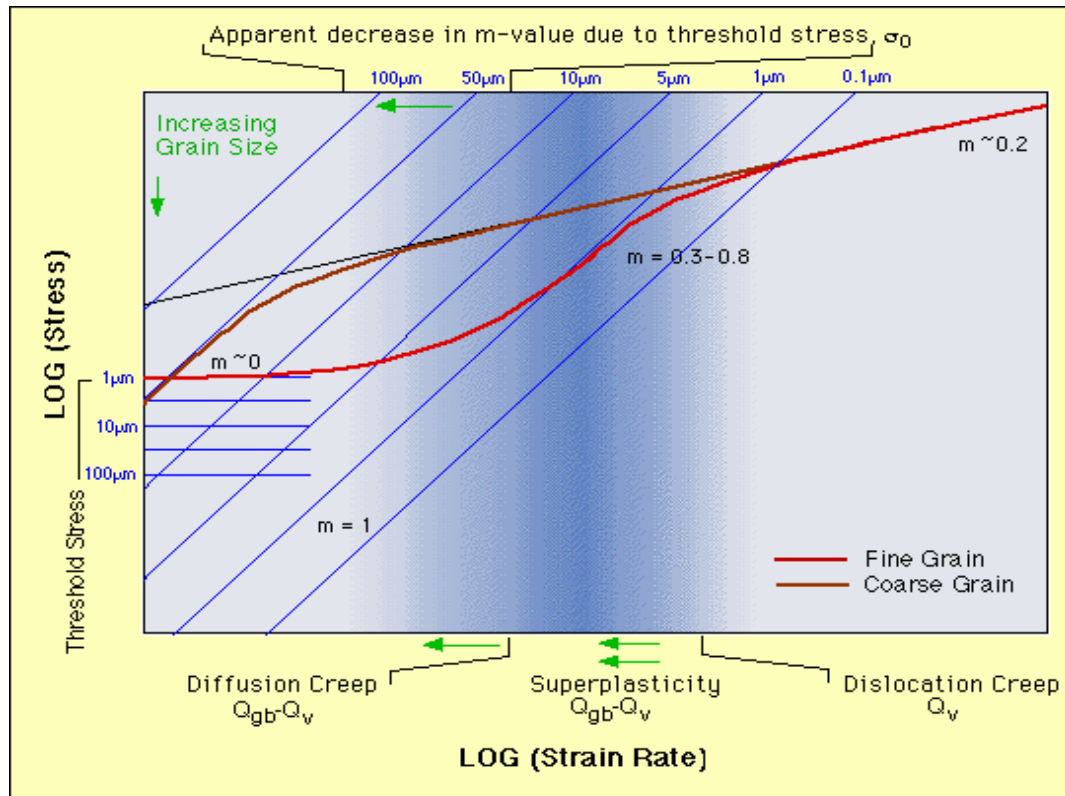
A. SUPERPLASTICITY AND DEFORMATION MECHANISMS

Superplasticity is the ability of a polycrystalline material to undergo extreme, neck-free tensile elongation. Engineering metals typically exhibit tensile elongations of 10% to 100%, depending mainly on temperature. Elongation values $\geq 200\%$ are considered superplastic and elongation values of 1000% or more are not uncommon. Superplastic behavior has been observed in ceramic and composite materials as well as metals [Ref. 5]. From the perspective of applied mechanics, superplasticity may be understood on the basis of the material's stress versus strain-rate relationship, which may be assumed to be of the form:

$$\sigma = K \dot{\epsilon}^m$$

σ is the flow stress, K is a material constant, $\dot{\epsilon}$ is the strain rate and m is the strain-rate sensitivity coefficient. At the onset of necking in the deforming gage section of a tensile sample the localized deformation results in a local increase in strain rate in the neck. A large value of the strain rate sensitivity coefficient, m , increases the resistance to further localized deformation in the neck. Large m -values tend to give uniform deformation and result in enhanced tensile ductility. Newtonian viscous behavior, which occurs in glass deformed near its melting point, corresponds to a value of $m = 1$, which, in turn, gives extreme resistance to localized necking and failure. Most polycrystalline metals exhibit $m \leq 0.2$ during elevated temperature deformation and elongation-to-failure values are generally $\leq 100\%$. For superplastic materials, m values are typically 0.33 – 0.5 [Ref. 5]; such values result in sufficient resistance to necking to enable superplastic response. Large values of the strain rate sensitivity coefficient, m , are necessary but not sufficient to assure superplastic response. The material must also resist the formation of cavities by separation along grain boundaries, which may lead to premature failure in superplastic materials.

Materials that have been processed for superplastic behavior often exhibit varying values of m as a function of strain rate during testing at a constant elevated temperature. Figure 2 shows a hypothetical material that exhibits an m value tending to 0.0 at the lowest strain rates, to values between 0.3 and 0.8 at intermediate strain rates and to a value of 0.2 at the highest strain rates [Ref. 5]. This circumstance may arise when two independent deformation mechanisms contribute to the elevated temperature deformation of the material. They include grain boundary sliding (GBS), which may be accommodated by slip, and dislocation creep that occurs independently of GBS.



Schematic plot of log (strain rate) vs. log (stress) [Ref. 6]

Because these mechanisms occur independently their effects are additive and the overall material response is determined by the sum of the strain rate due to GBS and the strain rate due to dislocation creep. It is the mechanism that gives the fastest strain rate will ultimately dominate [Ref. 7]. The low m -values at very low rates may reflect grain

growth, or a threshold mechanism [Ref. 7]. As shown in Figure 2, GBS dominates at intermediate strain rates and the material exhibits superplastic ductility. At high strain rates, dislocation creep dominates, and this results in normal ductility. The region of transition from superplastic to normal ductility spans about one to two orders of magnitude in strain rate [Ref. 6].

At a constant temperature, there is typically a maximum strain rate at which superplastic behavior may be observed. This corresponds to the decrease in m -value as strain rate increases above the intermediate range, as identified in Figure 2. To increase the practicality of superplastic forming the strain rate at which this transition occurs should be as high as possible. This may be accomplished by processing to refine the grain size and, thus, reducing the grain size that would increase the contribution of GBS and allowing for the transition in strain rate from GBS to dislocation creep.

A refined and a stable grain structure, which is rich in high angle boundaries, is thus a prerequisite for superplasticity [Refs 8,9]. GBS is concentrated at the grain boundaries and in a mantle-like region in the vicinity of the boundaries [Refs. 10,11]. In general, the maximum strain rate at which GBS is possible is inversely proportional to the grain size raised to a power of two or three [Ref. 12]. For this reason it is necessary to control grain growth, which can be accomplished by addition of second phase particles to inhibit grain boundary migration. High-angle boundaries are also required to enable sliding [Ref. 13]. High-angle boundaries can slide more readily than low-angle boundaries, which do not slide readily due to lattice registry across the boundary plane. An equiaxed grain structure will enable GBS better than an elongated structure [Ref. 5]. A random texture is thought to favor GBS. Finally, mobile grain boundaries will allow the relaxation of stress concentrations at triple points and other obstructions and permit the structure to remain equiaxed and avoid the formation of cavities.

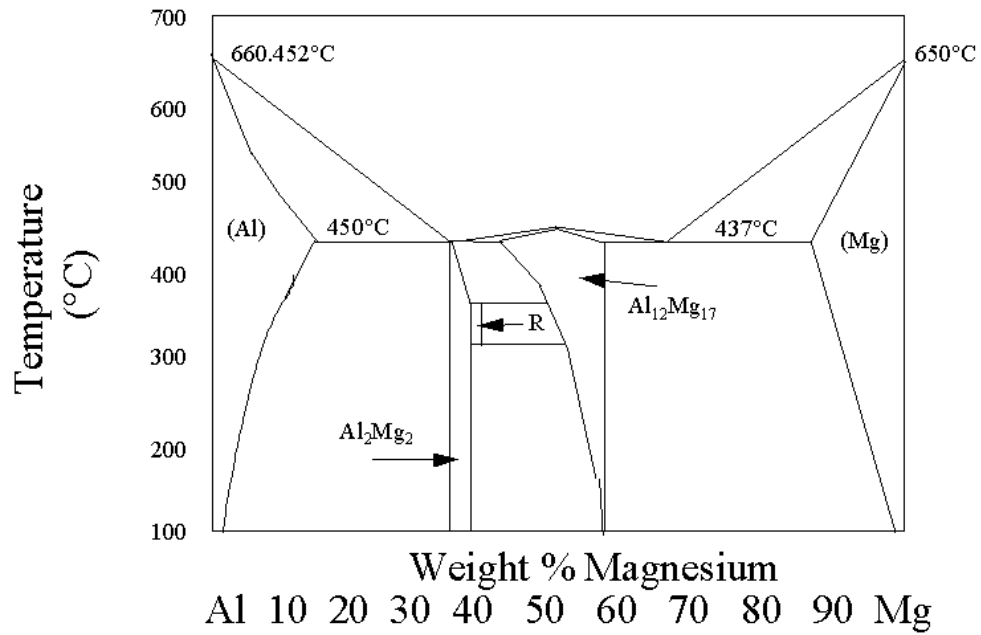
A fine-grained microstructure rich in high angle boundaries can be produced by introducing a dispersion of second phase particles sufficient in size to serve as sites for particle- stimulated nucleation (PSN) of recrystallization. In PSN, high angle boundaries are formed in deformation zones around the second phase particles, which must exceed a certain size, typically about 1.0 micron, in order to become nucleation sites [Refs. 14-17].

If the second phase particles are uniformly dispersed this will result in a fine, uniform and equiaxed microstructure. In general, PSN results in a randomly textured material due to the randomizing of lattice orientations within deformation zones around the second-phase particles [Ref. 14]. It has also been suggested that fine, dispersed particles possessing a higher hardness than the matrix can control cavitation by various recovery mechanisms in regions near the particle [Ref. 16].

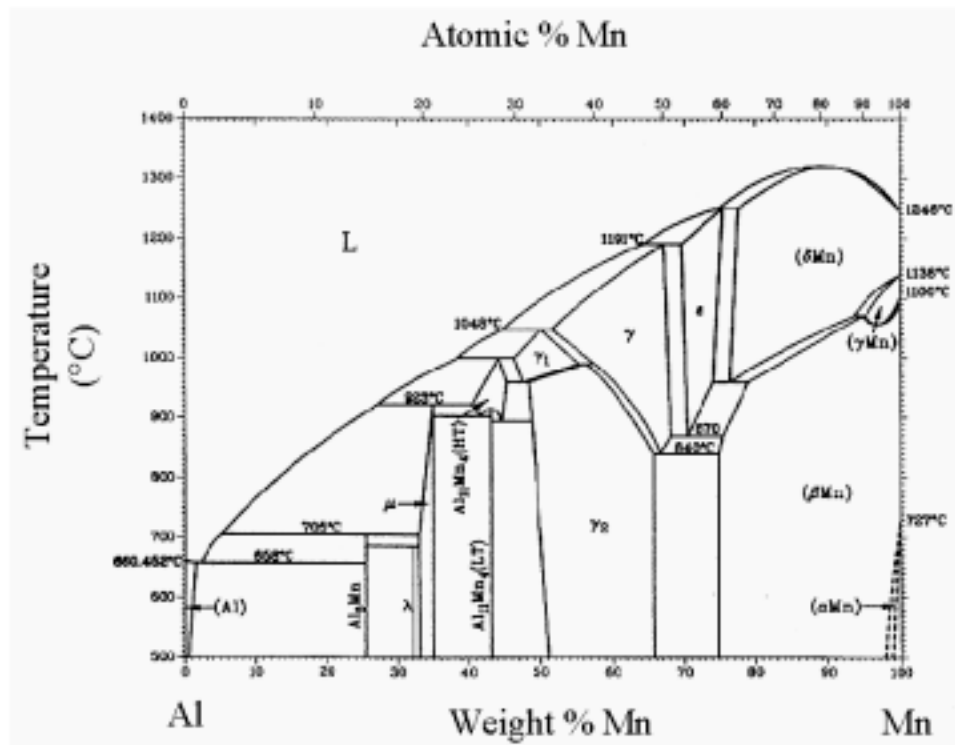
Aluminum is of interest in this research for its many desirable properties, which include low density, high weight-to-strength ratio, high thermal and electrical conductivities, corrosion resistance, and relatively high ductility. Military applications such as aircraft and light armor often require components that are strong and yet lightweight. These components are often fabricated from several individual parts often requiring extended manufacturing times, and thus higher cost, than if they were fabricated in the form of a single piece. Assemblies of separate parts also require fasteners, either bolts or rivets, which function as stress risers and lead to fatigue. Manufacturing of such strong, lightweight components in single units requires exceptional ductility.

AA 5083 alloy was designed specifically to be weldable and of intermediate strength. This wrought alloy contains nominally 4.70 weight percent Mg which facilitates weldability because the backfilling eutectic liquid can seal cracks that may develop during weld metal solidification. Also, a significant fraction of intermetallic particles can be dissolved in AA 5083 through homogenization treatments. This is because the solubility of Manganese in Aluminum at 550° C is approximately 1 weight percent, the maximum allowable in this alloy. The equilibrium phase diagram for Al-Mg and Al-Mn systems are shown in Figure 3 and Figure 4, respectively. The Manganese content exceeds the solubility limit of manganese in the aluminum solid solution up to the liquidus temperature for the Magnesium content of AA5083. There will thus be some insoluble second phase (MnAl_6) particles that will remain at all processing or deformation temperatures up to the liquidus temperature (574° C).

Al-Mg



Al-Mg Phase Diagram [Ref. 18]



Al-Mn Phase Diagram [Ref. 18]

Because dislocations are relatively mobile in a pure metal, plastic deformation usually occurs readily via dislocation motion. To increase the strength of a pure metal, it is necessary to restrict dislocation movement by creating as many barriers as possible. This is usually done by one of three procedures: strain hardening, solid solution strengthening, and precipitation hardening. Strain hardening results from plastic deformation where dislocations are created that interact with one another which restricts their subsequent movement. Solid solution strengthening results from local strain fields that develop around substitutional solute atoms within a host matrix. This occurs because of the greater size difference between the host and substitutional atom. Strength results from the strain field interacting with edge dislocation stress fields that inhibit dislocation motion. When the solubility limit of a solute in a host matrix is reached, precipitate particles form, which may lead to precipitation hardening.

B. COMMON FEATURES OF SUPERPLASTICITY

Analysis has revealed that there are certain common characteristics shared by most materials that exhibit superplastic behavior. First, most superplastic materials possess a fine, equiaxed grain size that is less than or equal to $10\mu\text{m}$. A fine grain size permits easier grain boundary sliding with associated grain rotation [Ref. 19]. The fine grain size may be stable when the volume fraction of second-phase precipitate particles is relatively high. Superplastic behavior also occurs only when the deformation temperature exceeds approximately one half the material's melting temperature, and the deformation strain-rate is between 10^{-2} and 10^{-4} sec^{-1} . Another common quality is a relatively high strain rate sensitivity coefficient, m , between 0.3 and 0.9. Higher values of m correspond to a finer grain size. Superplastic materials also exhibit a uniform reduction in thickness during deformation as a result of deformation by grain boundary sliding with accompanied grain rotation. Any texture remaining after large superplastic deformations is likely the result of slip occurring within individual grains as a consequence of the applied tensile stress. Failure occurs as a result of cavitation around the coarser precipitate particles.

C. PARTICLE STIMULATED NUCLEATION (PSN) THEORY

One of the common characteristics of superplastic materials is a grain size on the order of or less than $10\mu\text{m}$ [Ref. 1]. To produce a refined grain size, a material must have a high density of nucleation sites, and the presence of well-dispersed precipitates of a critical size in a matrix has been seen to promote recrystallization to a fine grain size. From observations involving materials containing non-deformable second-phase particles, Humphreys concluded that the precipitate particles must be a critical size for a given reduction in order that the particles act as nucleation sites. During deformation, the host matrix will flow around non-deforming, equiaxed particle if void formation does not occur. This creates a deformation zone containing a high density of dislocations. The overall density of these dislocations can be estimated from equation (1) [Ref. 20].

$$\rho_g = \frac{8f\gamma}{b d_p} \quad (1)$$

where f represents the volume of the precipitate phase, γ the shear strain, b the Burgers vector, and d_p the particle diameter. These dislocations provide strain energy in the deformation zone that is that is minimized by alignment of like-sign dislocations to create subgrains with local lattice rotations. The subgrain, or recrystallization embryo, that contains the highest dislocation density may form a recrystallized grain before neighboring embryos because it has the largest driving force. Humphreys observed that small particles ($d_p < 0.1\mu\text{m}$) and larger strains resulted in the dislocation structures necessary to produce sufficient local lattice disorientation. Theoretically, in order for the embryo to form a new grain and grow into the surrounding matrix it must be of sufficient size, δ_{crit} , defined by equation (2) [Ref. 20]:

$$\delta_{\text{crit}} = \frac{4\Gamma}{E} \quad (2)$$

where Γ is the boundary interfacial energy and E is the stored strain energy from deformation.

In addition, the critical size of the embryo, δ_{crit} , must also be smaller than the deformation zone, λ , that is created near the precipitate particle such that $\delta_{\text{crit}} < \lambda$ [Ref. 11].

Essential features in the creation of new grains by PSN of recrystallization are illustrated schematically in Figures 4 - 7. During straining, the size of the deformation zone is approximated by equation (3) [Ref. 20]:

$$\lambda = A d_p \varepsilon^{\frac{n}{n+1}} \quad (3)$$

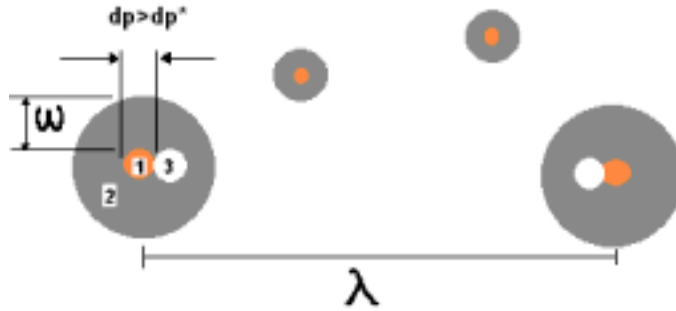
where λ is the width of the deformation zone, A is a material constant, ε the true axial strain, and n is the exponent from Holloman's strain hardening equation, equation (4):

$$\sigma = K \varepsilon^n \quad (4)$$

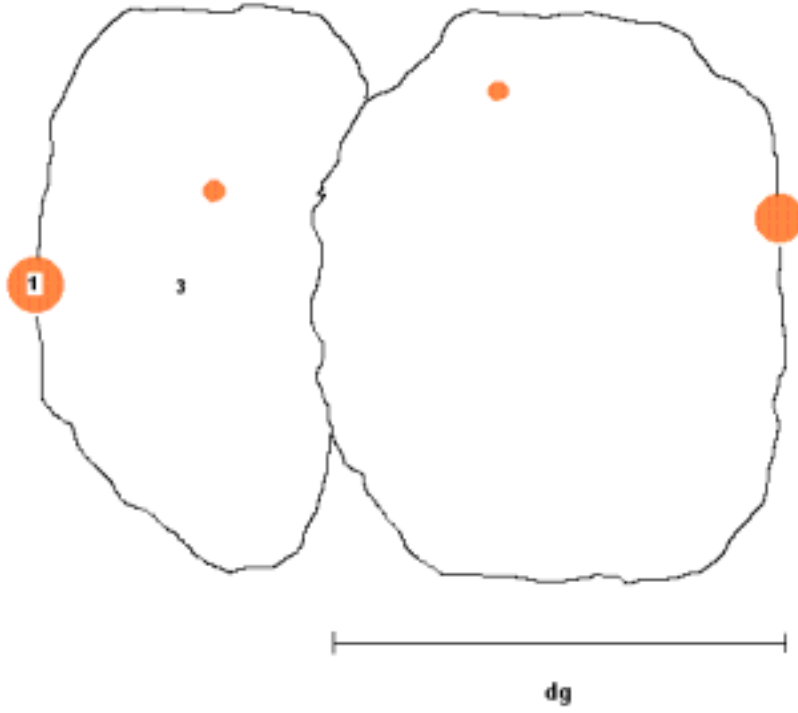
where σ is the true stress. As the deformation zone size, λ , increases, more embryos achieve conditions for nucleation. Increasing d_p and/or ε will increase λ , and, therefore, allow more embryos to satisfy this requirement.



Particles of diameter d_p (Region 1) and Deformation Zones (Region 2)



Deformation width, critical particle size and interval λ



Recrystallized grain size formed by PSN of grains given as $d_g \approx \lambda/2$

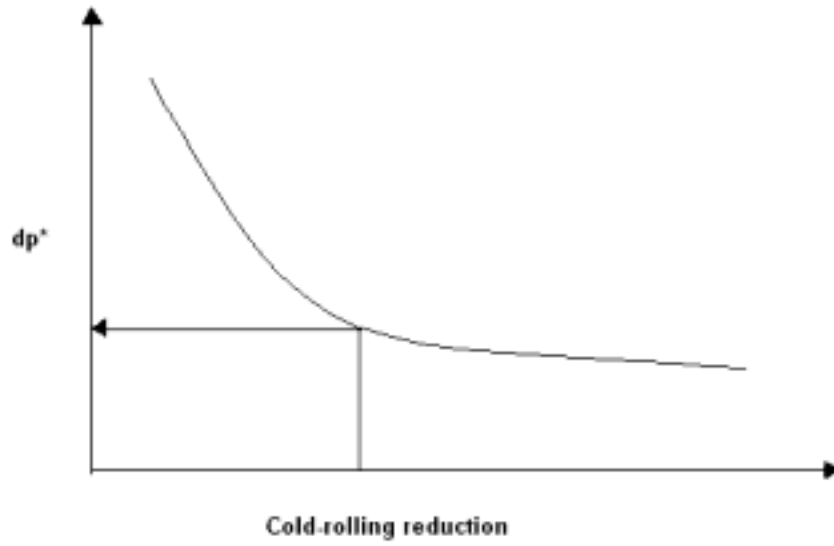
From equations (2) and (3), a relationship between particle size and strain necessary for PSN becomes:

$$A \epsilon_{p,crit}^{\frac{n}{n+1}} = \frac{4\Gamma}{E} \quad (5)$$

or

$$d_{p,crit} = \frac{4\Gamma}{A E} \epsilon_{p,crit}^{\frac{n}{n+1}} \quad (6)$$

Thus, as the true strain increases, the critical particle diameter necessary for PSN decreases as shown in Figure 6 [Ref. 21].



Effect of cold-rolling reduction on the critical particle size

Assuming that all nucleated grains grow until impingement with a neighboring grain, and that all particles are of the same size, where $d_p \geq d_{\text{pcrit}}$, the resultant grain size associated with a given precipitate particle size can be approximated by equating the grain size to the particle spacing, D_s [Ref. 21]:

$$D_s = \frac{d_p}{f^{1/3}} \quad (7)$$

Equation (7) shows that for the grain size, D_s , to be a minimum, the particle size must be a minimum (but $\geq d_{\text{pcrit}}$) for a given volume fraction, f . Nucleation must also occur at an appreciable rate, r , for recrystallization to take place. The rate of nucleation follows the relationship in equation (8): where ΔG^* is

$$r = A \exp \left(\frac{-\Delta G^*}{kT} \right) \quad (8)$$

the free energy of formation of a nucleus. For a high nucleation rate, the second term must be small which means that ΔG^* must be small and kT large. It necessary, therefore, that the processing temperature be as high as possible.

D. RESEARCH AT NPS

Recent research on thermomechanical processing at the Naval Postgraduate School (NPS) has sought, among other things, to devise processes that produce a superplastic response in existing Al-based alloys in order to avoid the addition of special alloying elements and the associated additional complexities and manufacturing costs. The PSN model previously described has been used in an effort to produce a microstructure that has both a fine grain size and large disorientation angle between neighboring grains, the two microstructural components believed necessary for superplastic behavior. Initially, an Al-10Mg-0.1Zr alloy was studied and has produced elongations of approximately 1100% at a tensile test temperature of 300° C. This alloy, however, represents a model system and subsequent efforts have examined Al 2519, nominally an Al-6.0Cu material.

Mathe initiated the research by employing a modified version of the TMP used with the AL-10Mg-0.1Zr alloy [Ref. 22]. Different combinations of cold rolling and overaging conditions were utilized to develop a superplastic microstructure similar to that found with the processed Al-10Mg-0.1Zr alloy. A ductility of 205% elongation was obtained when a 10 % prestrain at 200° C was applied to the material prior to overaging at 450 ° C for 10 hours. This TMP also produced a uniformly distributed θ -phase 1-2 μm in size, which was the size determined necessary for PSN [Ref. 20]. Bohman continued Mathe's work by adjusting overaging conditions [Ref. 23]. By increasing the overaging time at 450 degrees C to 50 hours, a significantly larger number of particles achieved a size greater than 1 micron which resulted in a refined grain size and an increased ductility of 260%. Dunlap further increased the averaging time from 50 hours to 100 hours and reduced the rolling temperature from 300 to 200 ° C to increase the stored strain energy [Ref. 24]. Neither of these changes resulted in further grain refinement. Zohorsky studied the effect of prestrain deformation temperature, overaging temperature, and other TMP variations on the production of second phase particles exceeding a critical size [Ref. 25]. It was concluded that a 10 % prestrain performed at room temperature instead of 200° C produced a more uniform distribution of particles exceeding a critical size [Ref. 25]. It was concluded that a 10% prestrain performed at room temperature instead of at 200 ° C

produced a more uniform distribution of second phase particles, and that the conditions of 50 hours at 200 ° C and 50 hours at 400° C produced the most promising microstructure. Peet subsequently varied the overaging temperature and times prior to rolling in an effort to further refine the grain size and varied the tensile test temperatures to further examine superplastic response [Ref. 26].

The preceding research sought to create a microstructure that contained precipitate particles of a critical size that would function as nucleation sites for recrystallization when subjected to a processing strain. In all cases, materials were rolled to strains of approximately 2.2 as dictated by initial billet thickness and available facilities. Moderate superplastic ductilities of up to 300 % resulted from these studies. To refine the grain size further, more of the precipitate particles must become active as nucleation sites. According to the PSN model, this can also be achieved by increasing the total processing strain on the material. In fact, McNelley et al. concluded that by increasing the processing strain on Al-10Mg-0.1Zr from 1.9 to 2.6 an increase in peak ductility from 450 to 1100% resulted [Ref. 21], which is in agreement with the PSN model. The current research with AA 5083 seeks to determine the effect of a variety of aging parameters followed by uniform cold reduction and constant recrystallization anneal on grain structure and intermetallic material.

III. EXPERIMENTAL PROCEDURE

A. MATERIAL

The material examined in this research was obtained from the General Motors Company via the University of Texas at Austin. The material, designated G1CC, had been produced by continuous casting (CC). Wrought conditions of the material had been subjected to various sequences of hot- and cold-rolling. The composition of the material is listed in Table 1 [Ref. 27]. Three different sets of sample material were received, representing the as-cast, the hot band, and as-rolled sheet forms. Of primary interest, the hot band material was received in the form of rectangular sheet samples 5mm in thickness, 210mm in length and 25mm in width. These had been sectioned from larger sheets of the material. Continuous cast aluminum typically is directly hot rolled and coiled after casting and the material is not homogenized, or held at a high temperature, prior to the rolling. This eliminates or decreases chemical segregation within the sheet before or during hot rolling. This structure characteristic is very important for aluminum alloys in subsequent processing. These alloys must have a uniform microstructure throughout the sheet in order to achieve the desired formability.

Mg	Mn	Fe	Si	Cu	Cr	Ti	Zn	Al
4.70	0.72	0.22	0.07	0.02	-	-	-	Balance

Table 1. **Aluminum Alloy AA 5083 (G1CC) Composition (Weight Percent)**
[Ref. 27]

B. PROCESSING

Prior to processing the hot band material, the plate was sectioned into billets with nominal dimensions of 5mm in thickness, 35mm in length and 25mm in width. The largest dimension was in the prior rolling direction. Each sample was stamped after initial milling with a number to distinguish it from the others.

The thermomechanical processing of the material consisted of three steps that are outlined in Figure 9. The as-cast material and the hot band material was sectioned prior to any processing so that the microstructure of the as-received material could be compared to that of the thermomechanically-processed material. The rest of the billets were then aged according to the annealing matrix as shown in Table 2.

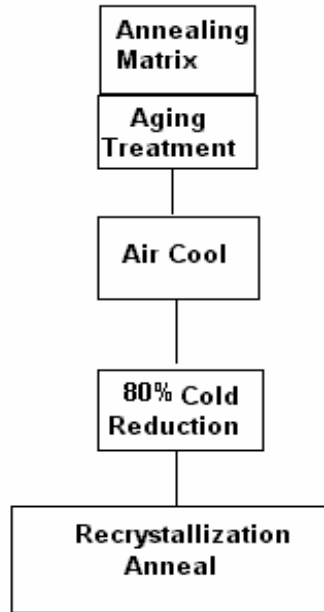


Figure 9. Thermomechanical Processing Steps

The aging treatments of 1 hour, 10 hours and 100 hours were intended to allow the second phase particles to coarsen and to allow second particles to precipitate out of solution. This was done in order to investigate the relationship between particle size and PSN. Thermocouples were placed in close proximity to each sample to ensure the necessary temperature was maintained during heat treatments. Following air-cooling of each sample to room temperature, the material was cold rolled in three passes from 5mm to 1mm in thickness (80% cold reduction). All thicknesses were measured with a standard micrometer. The cold reduction increased the dislocation density in the vicinity of the MnAl_6 particles so that the particles could become potential nucleation sites for recrystallization. Next, the material was given a recrystallization anneal at 450°C for 30 minutes.

This thermomechanical history is delineated in Figure 10. It includes the entire history of the AA 5083 Aluminum alloy from the initial as-cast state to the final recrystallization-annealed sample. Samples were obtained at key stages during the thermomechanical process to determine the microstructure at each stage.

500° C, 1 hour (R - P - C1)	500° C, 10 hours (S - P - C2)	500° C, 100 hours (T - P - C3)
525° C, 1 hour (U - Q - C1)	525° C, 10 hours (V - Q - C2)	525° C, 100 hours (W - Q - C3)
550° C, 1 hour (X - R - C1)	550° C, 10 hours (Y - R - C2)	550° C, 100 hours (Z - R - C3)

Table 2. **Annealing Matrix**

Specimens, approximately 5mm square in size, were sectioned from each aged billet using a Buehler Isomet high-speed saw. Sample grinding was carried out at 1000 rpm using an 11-4217 Buehler abrasive wheel with 800 grams of load applied to the sample. Buehler ISOCUT PLUS Fluid was used to cool and lubricate the specimen and to facilitate flushing away of all cutting debris. Samples of the cold-rolled material were sectioned from the final 1mm thick sheet product using a Buehler low-speed saw with a diamond-wafering blade. The low-speed saw was utilized to prevent any deformation from being introduced to the area for microscopic observation considering the 1mm thickness of the rolled samples.

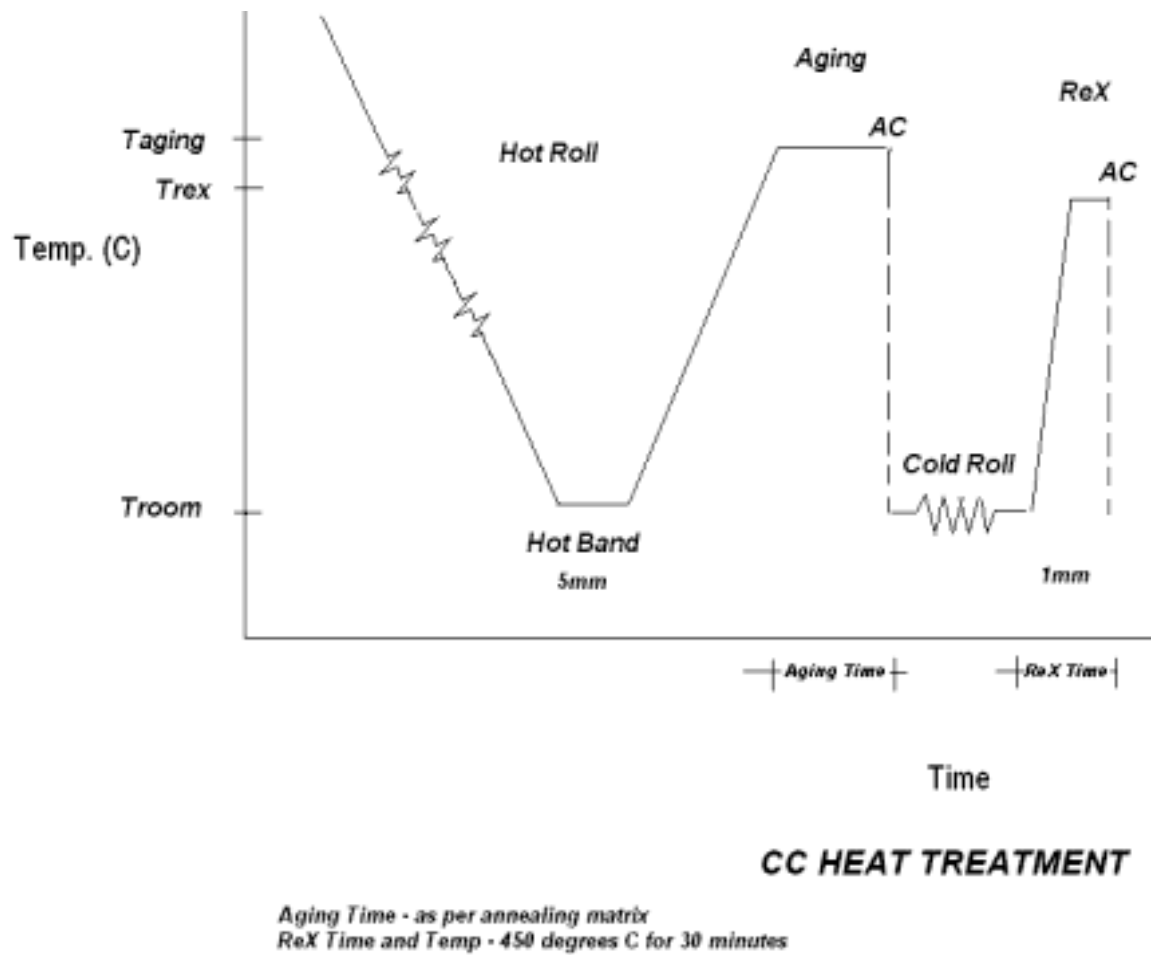


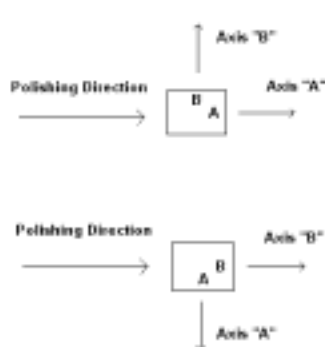
Figure 10. AA 5083 Heat Treatment History

C. METALLOGRAPHIC SAMPLE PREPARATION

Mechanical polishing of the samples was accomplished by carrying out the steps outlined in Table 3 for the indicated times. The sectioned specimens were ground using a Struers Knuth-Rotor-3 grinding wheel with Struers water-proof silicon carbide (SiC) paper of grits in the sequence of 500, 1000, 2400 and 4000. Light pressure was applied during the mechanical grinding during each grit stage. Grinding was conducted in one direction with water as the lubricant until all evidence of prior grinding was eliminated. The sample was then rotated 90° and the process was repeated. Rotating wheels were used for polishing, which was carried out in three stages. The specimens were polished first with a 3.0µm Metadi diamond compound on a Buehler MICROCLOTH polishing cloth for 10 minutes and then with a 1.0µm Metadi diamond compound on Buehler MICROCLOTH cloth for 10 minutes. All polishing was done using Metadi Fluid as a lubricant. The sample was then polished with a 0.05µm colloidal silica suspension on a Buehler MICROCLOTH cloth for 10 minutes. After each polishing stage, the specimen was rinsed with methanol, and ultrasonically cleaned and dried with warm air from a Buehler Torramet specimen dryer. Care was exercised to employ dilute diamond abrasive suspensions and a dilute colloidal silica suspension to avoid surface contamination with these abrasives.

A distortion-free final polish was required for electron backscatter pattern (EBSP) analysis in the scanning electron microscope (SEM). This is due to the very small interaction volume near the surface of the sample associated with formation of the EBSP's. Thus, the final polishing step was an electropolish conducted in a Buehler Electromet 4 apparatus using a 20% Perchloric Acid – 70% Ethanol electrolyte solution that was cooled to –25° C. After electropolishing, the specimen was rinsed with methanol and then air dried with cool air from the specimen dryer. All samples were examined in the as polished condition.

Step	Abrasive	Time	RPM
1	500 Grit SiC Paper	4 minutes*	140
2	1000 Grit SiC Paper	2 minutes**	140
3	2400 Grit Sic Paper	2 minutes**	140
4	4000 Grit SiC Paper	2 minutes**	140
5	Clean Ultrasonically	10 minutes	
6	3 μ m Metadi Diamond Suspension	10 minutes	90
7	Clean Ultrasonically	10 minutes	
8	1 μ m Metadi Diamond Suspension	10 minutes	90
9	Clean Ultrasonically	10 minutes	
10	0.05 Colliodal Silica	10 minutes	50
11	Clean Ultrasonically	10 minutes	
12	Electro Polish	20 sec (20 Volts) #	



* One minute per axis until sample is flat.

** One minute per axis or until previous scratches are no longer visible.

Electropolish with 20% HClO₄, 70% C₂H₅OH, 10% Glycerol.

Table 3. **Mechanical Polishing**

D. OPTICAL MICROSCOPY

The polished samples were first examined using optical microscopy to assess any defects that may have been introduced during sample preparation. The optical microscope was also used for a preliminary assessment of the size and size distributions of the second phase particles.

E. ORIENTATION IMAGING MICROSCOPY

Subsequently the polished samples were placed in a TOPCON SM-510 SEM, operating with a tungsten filament, for data collection and analysis. The microscope was operated at an accelerating voltage of 20kV. The samples were placed in the SEM holder that inclines the sample surface at 70° to the vertical. This was done in order to utilize the EBSP analysis capability of the Orientation Imaging Microscopy (OIM) hardware and software provided by EDAX / TexSEM, INC. Figure 11 represents the orientation of the sample in the chamber and the orientation of the sample as viewed from the camera position, respectively. Photomicrographs of the processed and annealed material showed good grain orientation. This procedure allowed grain size information to be obtained.

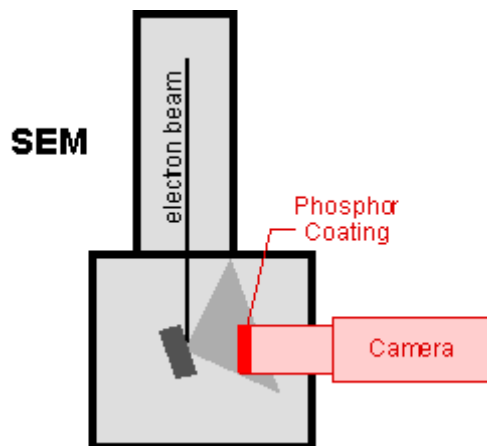
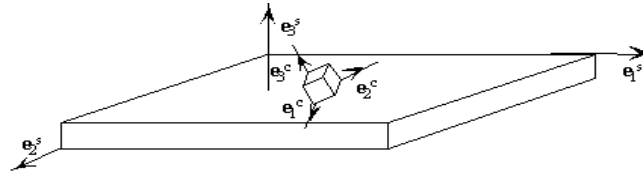


Figure 11. Sample Orientation and Camera position [Ref. 28]

The fixed reference axes are assigned in the software. The Euler angles were calculated and are defined as follows: the RD direction is assigned as positive downward; ND is positive toward the phosphor screen; and TD is parallel to the horizontal. Figure 12 illustrates the orientation and direction of the Euler angles. The SEM was operated in spot mode with an electron beam diameter of about 0.15 mm. The diffracted electrons impinge upon a phosphor screen, thus illuminating it.



Lattice orientation is specified in terms of the Euler angles ϕ_1 , ϕ , and ϕ_2 that describe rotations from the crystal coordinates to the sample coordinates.

Figure 12. Euler Angle Orientation and Direction [Ref. 29]

The SEM was set for 1000X magnification and 20.0 kV accelerating voltage. The working distance was set to maintain the geometry of the sample relative to the center of the phosphor-coated screen and to improve the image quality of the diffraction pattern. Once the specimen was positioned, the secondary electron image was focused to improve the image quality of the diffraction pattern. From the camera control unit, background noise was captured for later subtraction. The spot option was then selected on the SEM console corresponding to a specific area approximately equal to μm in extent on the sample. A fiber optic attachment to a low-light camera (viewing the backside of the phosphor screen) provided input to a monitor that displayed the BKD pattern. The BKD pattern appeared blurred until the background noise was subtracted from the image. The pattern of Kikuchi bands and the major zone axes then became clear. For this face-centered cubic (FCC) Al alloy, each pattern usually contained two of the following three major zone axes: $\langle 100 \rangle$, $\langle 110 \rangle$, and $\langle 111 \rangle$. Figure 13 shows a representative BKD pattern before and after indexing. After careful calibration of the software using the recognized major zone axis, the grain orientation information was given in the form of

three Euler angles, ϕ_1 , ϕ , and ϕ_2 with the z-axis corresponding to the normal of the specimen surface and the x-axis along the rolling direction axis. In practice, each pattern is analyzed several times, and resulting solutions are then ranked in the software. The patterns are then assigned a best-fit solution called the Confidence Index (CI). There is 95% probability that the indexing is correct when the CI values are greater than 0.1. OIM data collection is accomplished by progressively displacing the electron beam over a preselected area on the sample-surface area in a raster pattern. The resulting data file may then be employed to construct an image based on these orientation measurements. The OIM software allowed the production of OIM grain maps, pole figures representing the texture and other data. Grain maps are color-coded maps with a common color assigned to contiguous points of common orientation as is evident for grains.

F. BACKSCATTER ELECTRON IMAGING

The SEM is equipped with a tungsten filament to capture the backscatter electron (BSE) images. Samples were placed in a flat position in the microscope. The accelerating voltage was set to 20 kV and the working distance was reduced to less than 10 mm in order to obtain acceptable orientation contrast. The BSE imaging was used to provide an independent assessment of the microstructure. An important limitation of BSE imaging is that obtaining accurate grain sizes is only possible when each image is carefully calibrated. Also, grain-to-grain disorientations cannot be determined by this method.

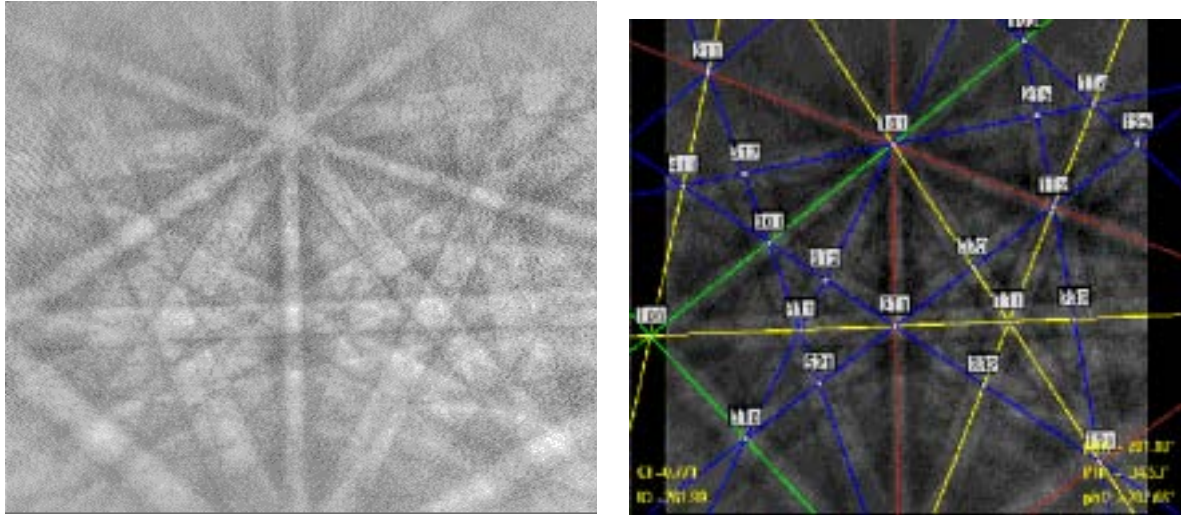


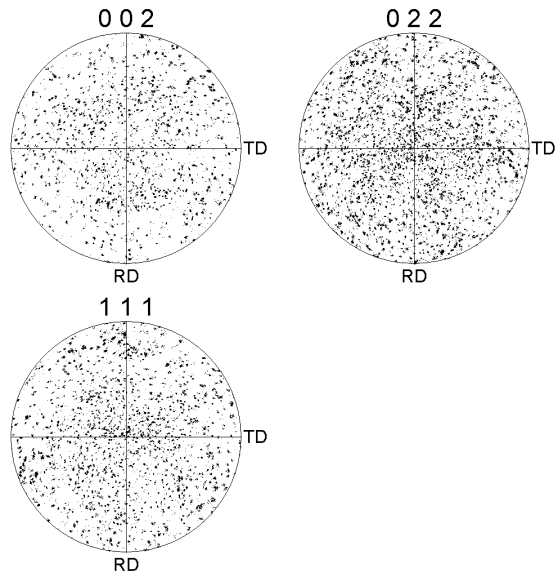
Figure 13. KBD Pattern (before and after indexing)

IV. RESULTS AND DISCUSSION

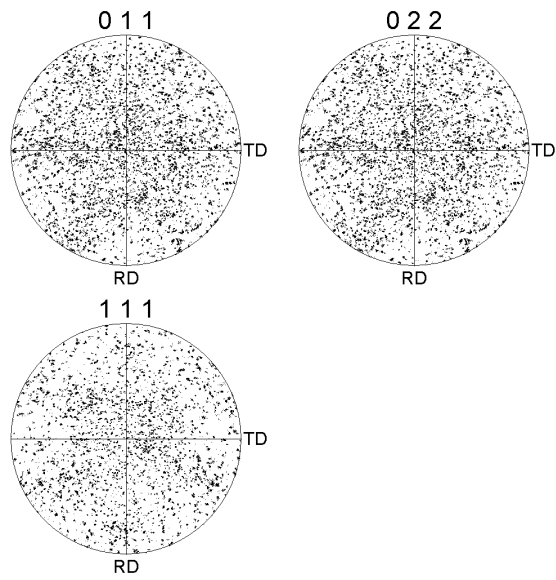
A. ROLE OF PARTICLES IN PSN

1. GICC Texture and Grain-to-grain Orientations

Wrought aluminum alloys require deformation and recrystallization to achieve grain refinement and enable superplasticity. Empirical approaches have lead to the development of two distinct thermomechanical processing (TMP) routes. Computer-aided electron backscatter diffraction (EBSD) analysis methods have provided insight into the mechanism of recrystallization and formation of grain boundaries for both of theses routes [Ref. 30]. In the following studies the TMP involves discontinuous recrystallization. The discontinuous reaction that is capable of creating fine-grained, wrought aluminum material is particle-stimulated nucleation, PSN, of recrystallization following deformation of alloys containing dispersions of second-phase particles. Overaging treatments are used to develop coarse precipitates approximately 1 μ m in size prior to any cold working. The second-phase particles are intended to become sites for PSN of recrystallization. The complex deformation patterns in regions surrounding particles result in fine cells or subgrains, of random lattice orientation, some of which are surrounded by high-angle boundaries. Because lattice orientations within deformation zones around particles tend to be random the resulting grain orientations due to PSN also tend to be random. Figure 14 shows pole figures for samples R and Z. Examination shows that the texture for both samples is random. Figure 15 illustrates histograms of the grain-to-grain disorientations for boundaries as well; these distributions correspond closely to the Mackenzie distribution [Ref. 31] for disorientations of randomly oriented cubes. Thus, these samples contain boundaries that are predominantly high-angle in nature. The OIM data then implies PSN. The focus of the study was then directed to analyzing the effects of annealing and strain on the dispersion of the particles, the particle size distribution and the grain size. The study provides insight into the effect of annealing, constant cold reduction and recrystallization annealing within the framework of Humphreys' PSN model [Ref. 20].

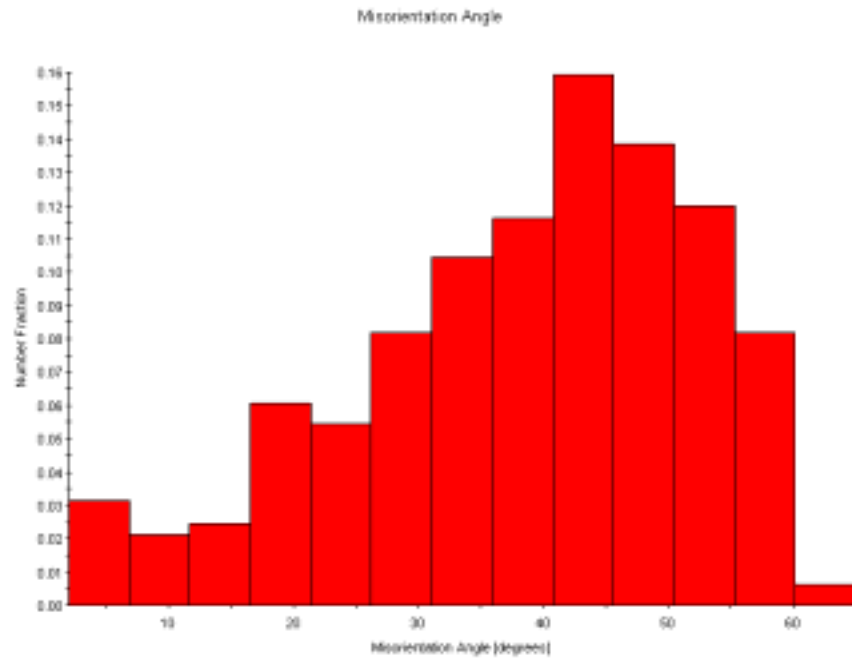


Sample R

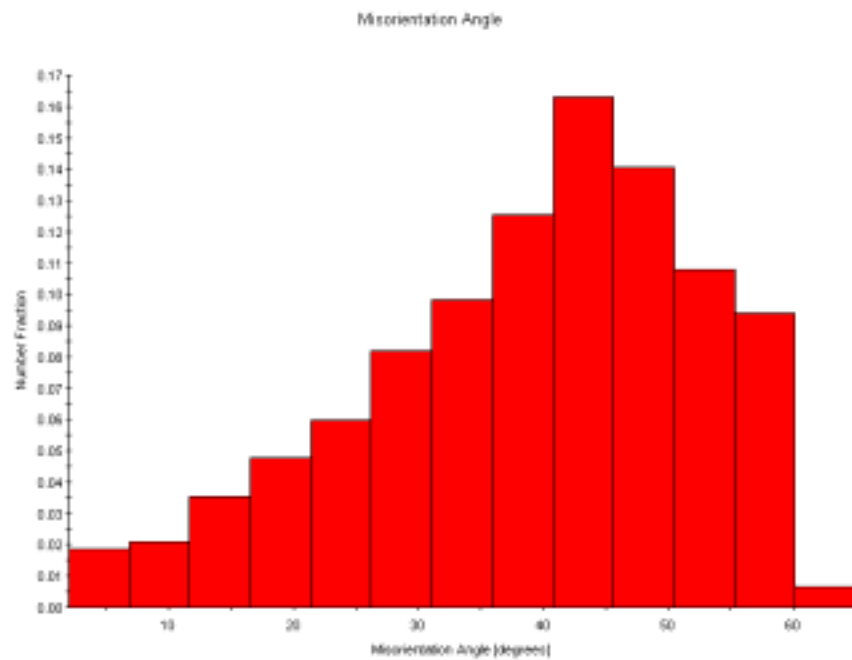


Sample Z

Figure 14. Textures of Sample R and Sample Z.



Sample R



Sample Z

Figure 15. Misorientation Angles for Sample R and Sample Z.

2. Optical Microscopy

The G1CC material was provided in both the as-cast as well as the hot band condition; samples of both conditions are shown in Figure 16. Initially, the materials were evaluated by optical microscopy to determine the effects of the warm rolling on the as-cast material. Optical micrographs of these materials show large, irregular primary particles of the MnAl_6 phase in as-cast material, suggesting that a large portion of the Mn in the alloy has come out of solution during solidification as MnAl_6 . This is evident in Figure 17(a), wherein the primary particles are $5\mu\text{m}$ to $15\mu\text{m}$ in size. The rolling leading to the hot band condition has resulted only in the aligning of these primary particles with the rolling direction.

PSN theory provided the basis for selection of the aging times and temperatures. The goal of using longer aging times was to coarsen the particles already present in order to increase the proportion of particles exceeding the critical size for PSN while also providing time for others to precipitate from solution. The longer aging times in essence amount to a prolonged homogenization treatment. Aging would also aid in creating a uniform dispersion of particles. This would provide better control of grain size in subsequent cold rolling / recrystallization treatments wherein larger particles would then act as sites for nucleation of recrystallization. Dispersed particles have a direct effect on grain-boundary mobility and thus grain growth. Fine precipitates in the dispersion can also inhibit grain growth even if too small to serve as sites for nucleation and recrystallization. In preliminary work it was attempted to homogenize AA5083 as near as possible to the alloy melting point (estimated to be 576°C) to determine whether the Mn could be re-dissolved prior to overaging. At temperatures approaching the melting range, “sweating” of the material, reflecting the onset of melting, was observed and it was deemed impractical from an industrial perspective to employ temperatures above 550°C .

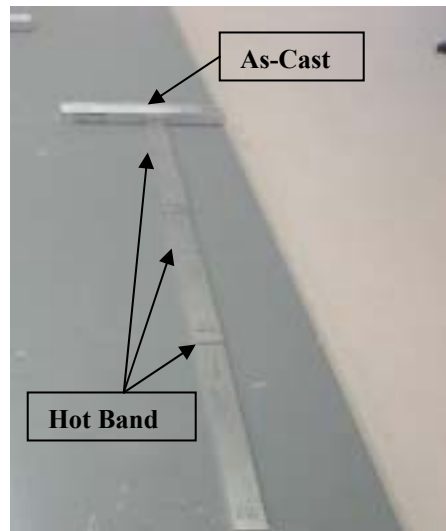
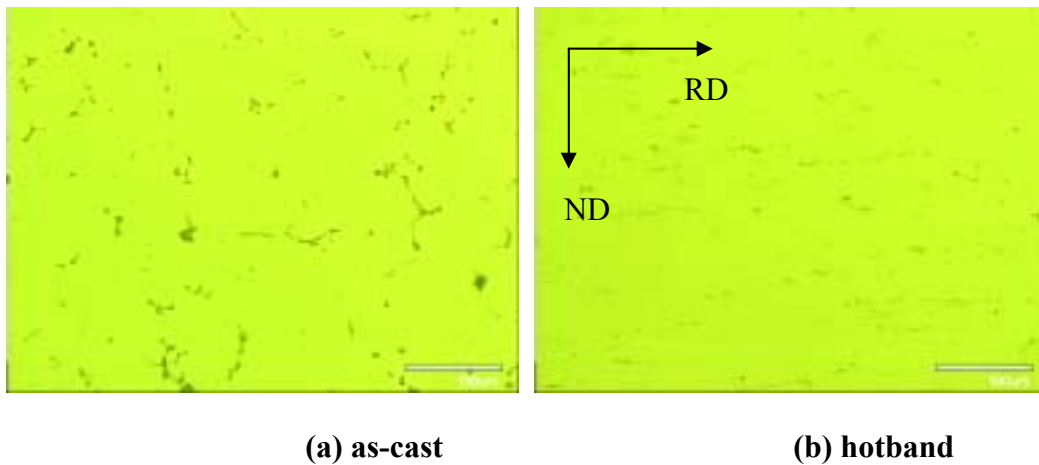


Figure 16. G1CC, As-Cast and Hot Band materials prior to TMP



(a) as-cast

(b) hotband

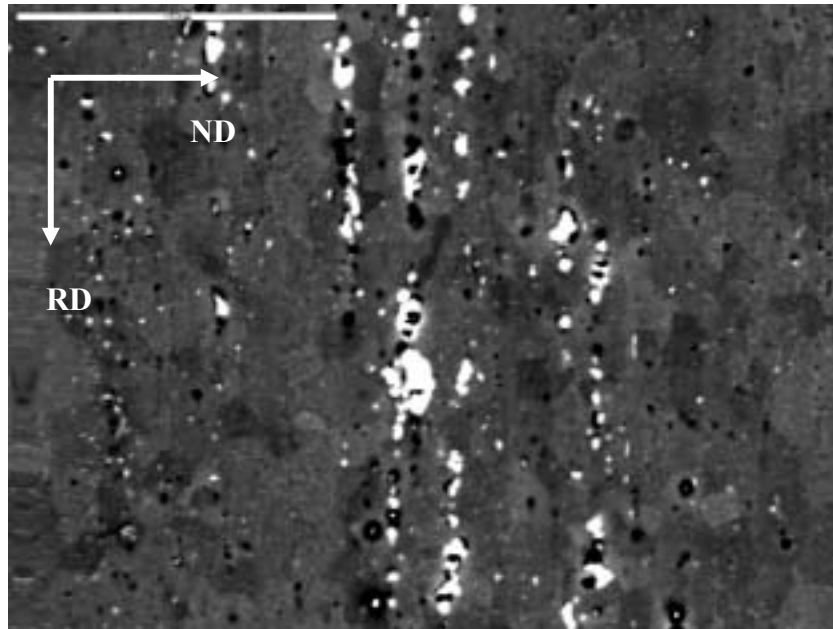
(scalemarker bar is 100 μ m)

Figure 17. Optical Micrographs of G1CC As-cast and Hotband Materials

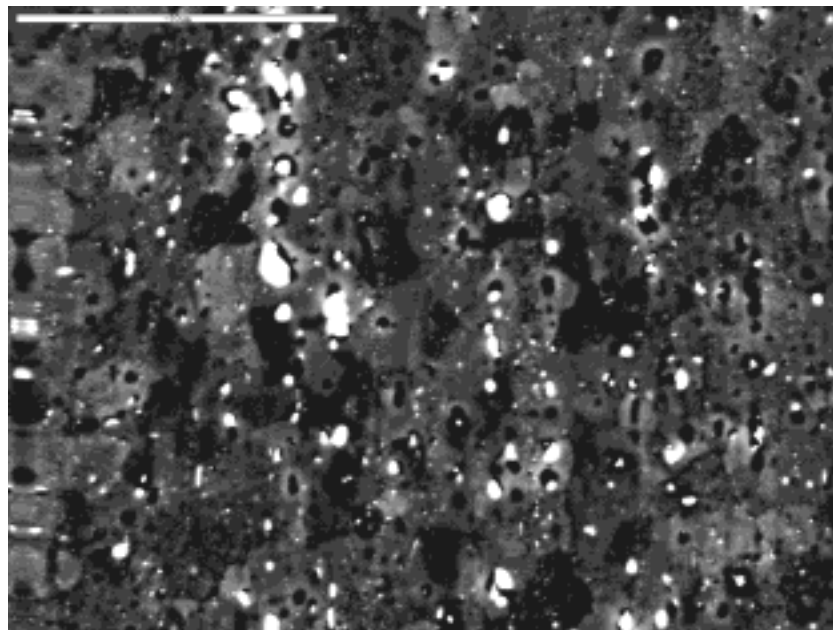
As will be shown, some of the Mn in the alloy has precipitated as coarse MnAl_6 during solidification of the continuous casting process and the remainder has subsequently formed fine particles of this phase. The coarse particles are insoluble at any temperature below the melting range. The fine particles are relatively stable against coarsening during annealing and so there is limited opportunity to control grain size through control of particle dispersions in this alloy.

3. Backscatter Electron (BSE) Imaging

Backscatter electron (BSE) images were utilized to analyze second phase particles in the G1CC material. The microscope was carefully adjusted for each image in order to enhance contrast. Of primary interest were samples that had been aged, subjected to 80% cold rolling strain (true strain of 1.25) and a recrystallization anneal at 450° C for 30 minutes. During the following presentation of results and discussion, the BSE images and OIM data for samples R and Z only will be shown. These represent the extremes of the matrix (shortest time + lowest temperature; and longest time + highest temperature). BSE images and OIM data for the remaining samples are provided in the appendices. Figure 18 illustrates the presence of stringers of large MnAl_6 second-phase particles. Identical results were obtained using Wavelength Dispersive Spectrometry (WDS) methods [Ref. 32]. It is clear that increased temperature and time during homogenizing anneals has little effect on these large particles.



Sample R



Sample Z

(scale marker bar is 50 μ m)

Figure 18. BSE images. Second Phase. Samples R and Z

Some overall coarsening was evident in sample Z (aged at the 550° C for 100 hours) in that a mean particle size of 1.29µm was obtained from statistical analysis of the data. In the analysis, 59 particles exceeded a size of 1.5µm, the largest count of within the entire set of samples, for this assumed value of d_p^* . Comparison of samples R and Z in figure 18 suggest a reduced number of MnAl₆ particles in sample Z brought about by coarsening at a higher temperature and longer aging time. However, such a comparison also indicates the need for detailed statistical analysis of these images.

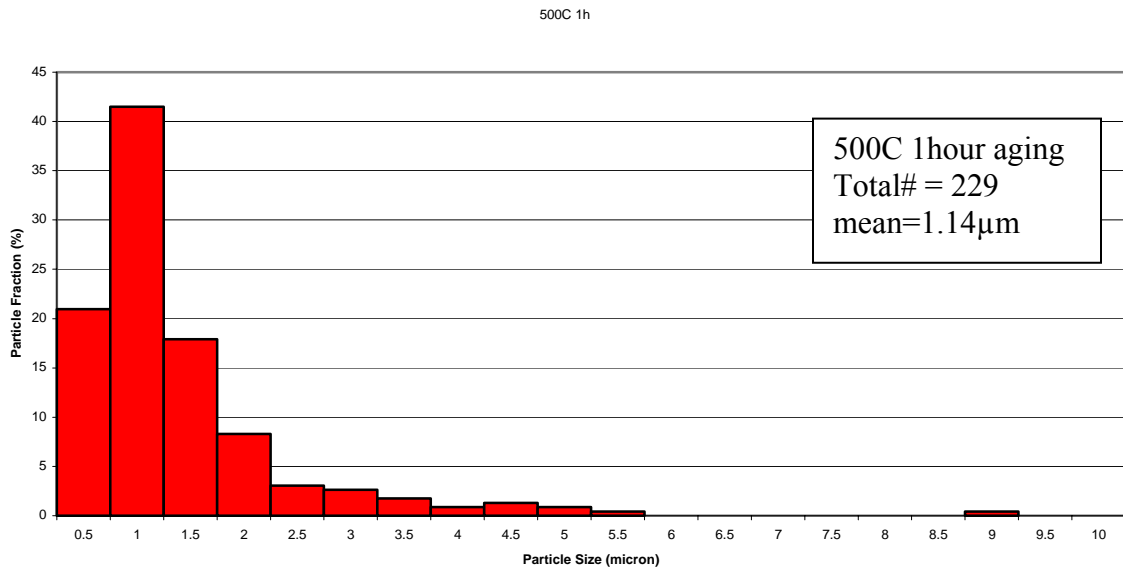
4. Particle Fractions and Particle Size Studies

Various micrographs were used for each of the nine samples in order to obtain representative images of each sample. This was done because the particle fractions varied from image to image and from sample to sample. Figure 19 shows the particle fractions for sample R and for sample Z. The Scion image software provided area fractions of each particle within the total area of each image. The particle sizes were extracted from the area fractions based on a number-weighted averaging. The number-weighted mean particle size was calculated as follows:

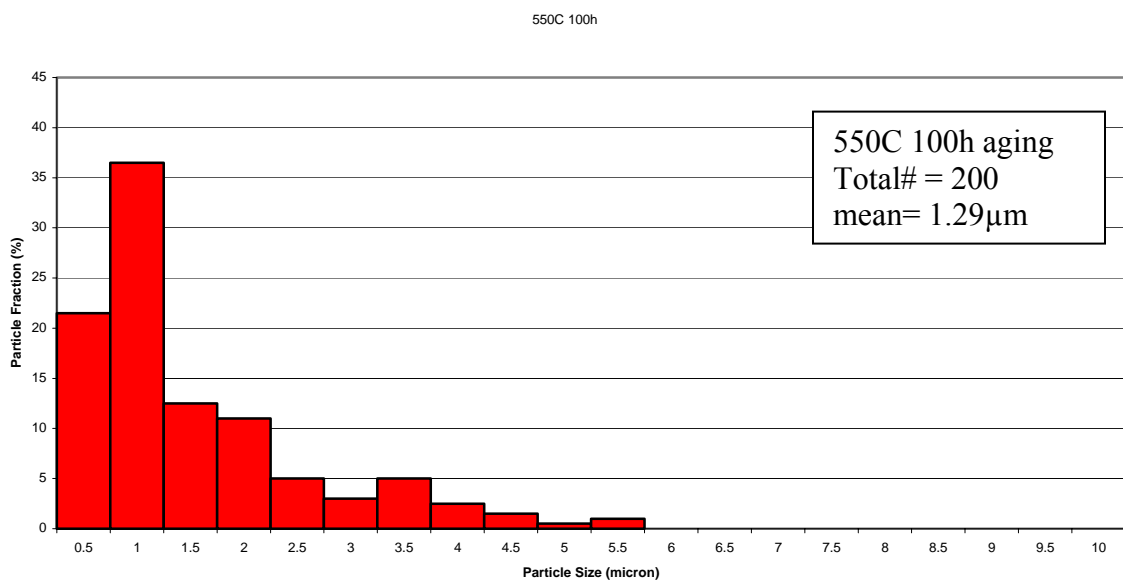
$$d_{p,mean} = \frac{1}{n} \sum_i^n \sqrt{\left(\frac{4A_i}{\pi}\right)} \quad (9)$$

where $d_{p,mean}$ represents the mean particle size and A_i is the area of each particle.

The particle fractions were then plotted versus particle size. Figure 20 displays histograms of particle size distributions for samples R and Z. Each histogram was constructed by taking the total number particles counted within bins of 0.5µm width for particle diameters 0.5µm to 10µm, and then normalizing these data by the total number of particles counted. Normalization removes differences in particle densities from comparisons between samples. While these data suggest an increase in mean particle size and an increasing number of coarse particles as the expense of small particles, the effect is small and the particle size distribution is quite stable throughout this matrix of annealing conditions.



Sample R



Sample Z

Figure 19. Particle Fractions for Samples R and Z

Detailed statistical analysis was employed with the data set in order to assess the dependence of particle size and size distribution on annealing parameters. Thus, particle sizes were determined for each sample and a number weighted mean particle size was calculated. The standard deviation and the standard error were then calculated for each sample. The following equations were used to find the statistical values [Ref. 33].

$$s^2 = \frac{\sum (d_{p,i} - d_{p,mean})^2}{n - 1} \quad (10)$$

$$s = \sqrt{s^2} \quad (11)$$

$$s_{\bar{x}} = s / \sqrt{n} \quad (12)$$

In equations 10-12, s represents the sample standard deviation, $d_{p,i}$ is the size of the particle, $d_{p,mean}$ is the mean particle size and $s_{\bar{x}}$ is the standard error. Figure 22 summarizes the statistical analysis of the particle size distribution. The error bars represent a range of plus or minus the standard error centered about the sample mean. What is clearly evident is that the size distributions of particles nearly overlap across all samples suggesting no change within the statistical significance of the data. The distribution in size is close to normal for each sample and so the standard deviations were determined. This allowed for the application of confidence intervals (CI) and confidence levels for each of the three aging temperatures and times.

Sample	\overline{x} microns	S	$S_{\overline{x}}$
R	1.14	1.01	0.07
S	1.16	1.01	0.06
T	1.21	0.97	0.07
U	1.13	0.79	0.08
V	1.25	0.99	0.10
W	1.36	1.21	0.09
X	1.13	0.92	0.07
Y	1.24	1.10	0.08
Z	1.29	1.07	0.07

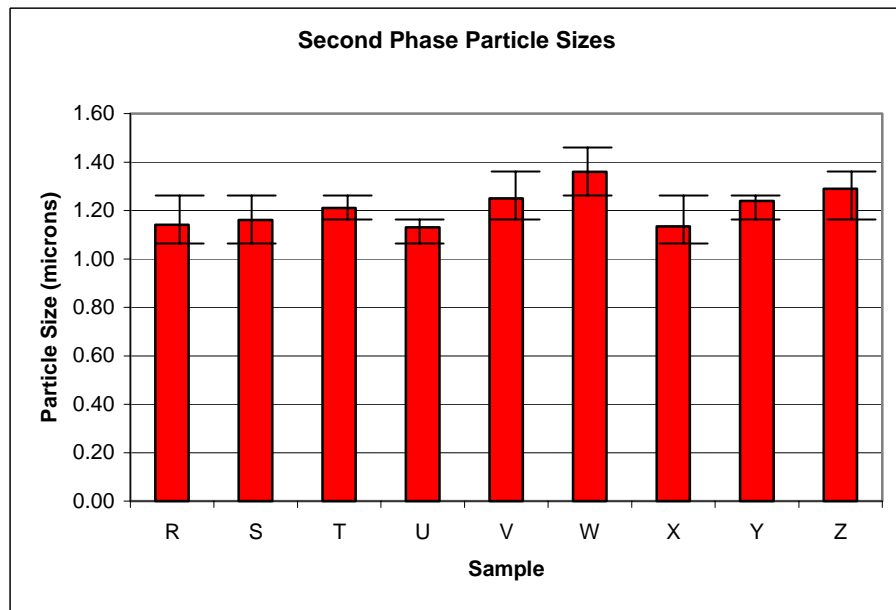


Figure 20. Particle Sizes for all samples with standard error bars

While a cursory examination of the histograms suggests that slight coarsening may be occurring at each temperature a more detailed statistical analysis suggests that such a conclusion should not be made. A point estimate, because it is a single number, provides no information by itself about the precision and reliability of estimation. Instead of reporting a single value for the parameter being estimated it is necessary to report an entire interval of plausible values. Confidence intervals were calculated by first selecting confidence levels. This best measured the degree of reliability of the intervals within each of the various temperatures and times of the annealing matrix. For this study a 95% confidence level was applied. A 95% confidence level implies that 95% of particle sizes within any given image or sample chosen would give an interval that included the mean particle size, $d_{p,mean}$. This would also imply 5% of all samples would yield an erroneous interval. For this portion of the study the following equation was used:

$$d_{p,mean} - 1.96 \frac{\sigma}{\sqrt{n}}, d_{p,mean} + 1.96 \frac{\sigma}{\sqrt{n}} = \text{CI (95\%)} \text{ for } d_{p,mean} \quad (13)$$

where σ is the population standard deviation, $d_{p,mean}$ is once again the mean particle size and CI stands for confidence interval. At 500° C samples R, S and T were analyzed for a confidence level of 95%. The mean particle sizes were 1.14 μm , 1.16 μm and 1.21 μm , respectively. The effect of increasing time at 500° C had no effect on particle size because the confidence intervals overlap. The same overlap in confidence intervals was observed for samples U, V and W at 525° C and samples X, Y and Z at 550° C. This implies that if the aging treatments were conducted several times between 500° C and 550° C, there is a 95% probability that mean particle sizes within the spread of standard error will overlap. The same conclusion was reached when each sample was compared at different temperatures but with the same time constraint. What the study ultimately implies is that the annealing treatment followed by the 80% cold reduction had a minimal effect on particle size.

B. EFFECTS OF ANNEALING ON GRAIN SIZE CONTROL

1. Backscatter Electron (BSE) Imaging

Various micrographs were used for each of the nine samples in order to obtain the best representative image of each sample. This was done because the grain sizes varied from image to image and from sample to sample. Figure 22 shows grain sizes for sample R and sample Z. After careful calibration of each image, each grain was measured at its minimum and maximum diameter using the ISIS software provided with the SEM. Figure 21 shows the method in which each grain was measured. Once each grain diameter was found the average-area-weighted grain size was calculated. The following equations show how each area-weighted grain size was calculated. A_{mean} is the mean grain area, D_i is one of the grain diameters, and $D_{g,mean}$ is the mean grain diameter.

$$A_{mean} = \frac{1}{n} \sum_i^n \left(\frac{\pi D_i^2}{4} \right) \quad (14)$$

$$D_{g,mean} = \sqrt{\left(\frac{4A_{mean}}{\pi} \right)} \quad (15)$$

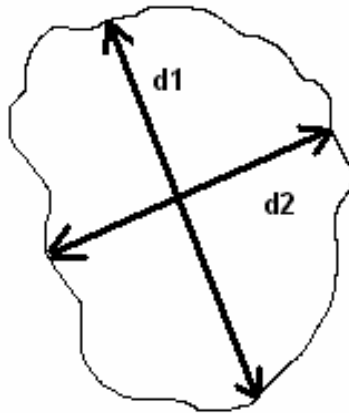
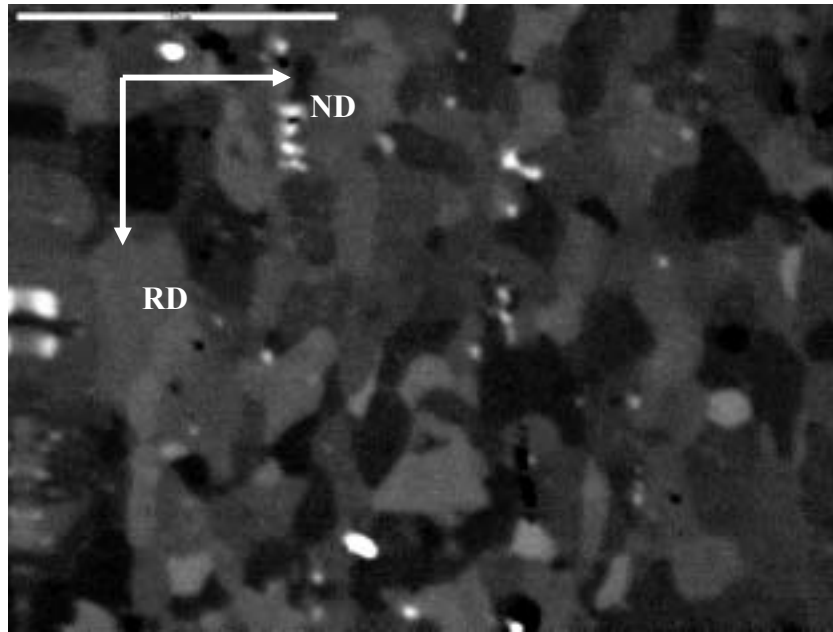
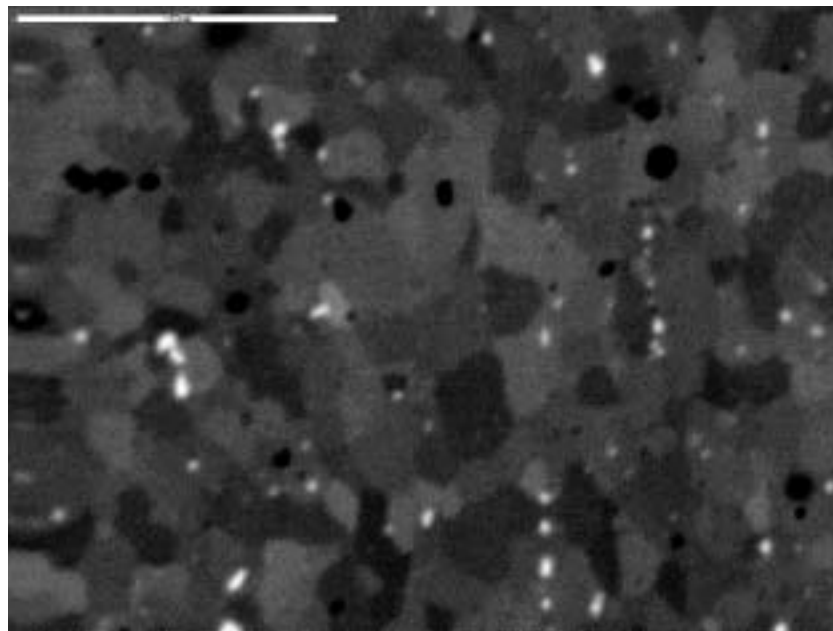


Figure 21. Grain Size measurements along major and minor diameters



Sample R



Sample Z

(scalemarker bar is 50 μ m)

Figure 22. BSE images of Grains in Samples R and Z

2. Grain Size Study

After viewing the data obtained through backscatter electron imaging a statistical analysis of each grain size within each image was conducted. This was done in order to compare the results of each condition quantitatively so that any relationship to the TMP could be found. To determine the variation in data a statistical approach was taken to investigate the fluctuation in data. Area-weighted grain sizes were calculated for each sample. The standard deviation and the standard error were then calculated for each sample. The following equations were used to find the statistical values [Ref. 33].

$$\text{Sample Variance} \quad s^2 = \frac{1}{n-1} \sum_i^n (D_i - D_{g,mean})^2 \quad (16)$$

$$\text{Standard Deviation} \quad s = \sqrt{s^2} \quad (17)$$

$$\text{Standard Error} \quad s_{\bar{x}} = s / \sqrt{n} \quad (18)$$

In equations 16-18, S is again the sample standard deviation, D_i is the size of the grain diameter, $D_{g,mean}$ is the mean grain diameter and $s_{\bar{x}}$ is the standard error. Figure 23 summarizes the analysis of the grain size data from all BSE images. The figure also shows standard error bars representing the standard error centered about the mean grain size for each sample. While cursory examination again suggests there is some dependence on the annealing treatments, e. g., in sample Z the standard error bar doesn't appear to overlap the standard error bars of the other sample mean grain-size diameters. A confidence level study was applied as had been done with the particles.

Sample	\overline{x} microns	S	$S_{\overline{x}}$
R	7.83	2.80	0.27
S	7.55	2.55	0.24
T	7.99	2.50	0.24
U	7.83	2.39	0.23
V	7.70	3.18	0.30
W	7.50	2.46	0.23
X	7.64	3.16	0.30
Y	7.99	2.89	0.28
Z	7.42	2.20	0.21

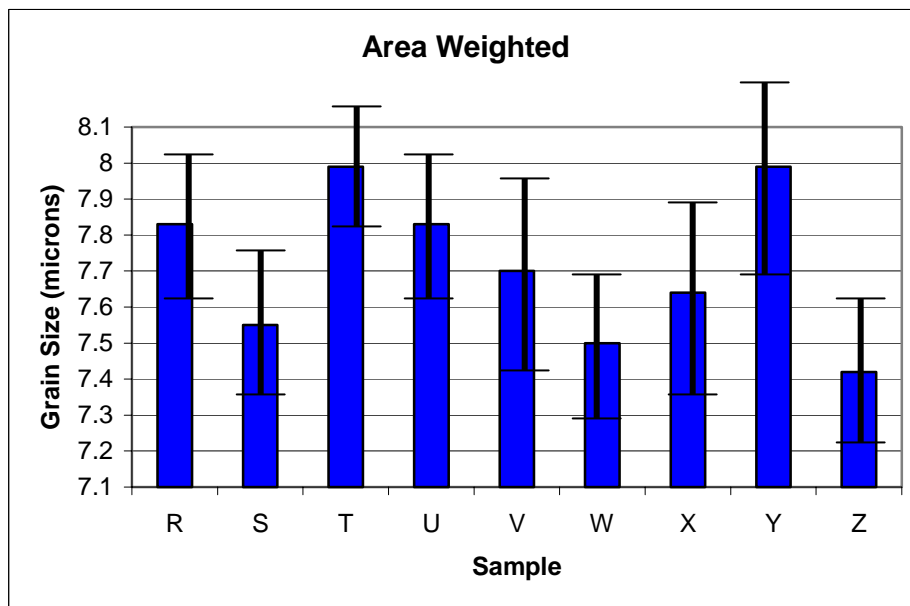


Figure 23. Grain Size Results of BSE Imaging

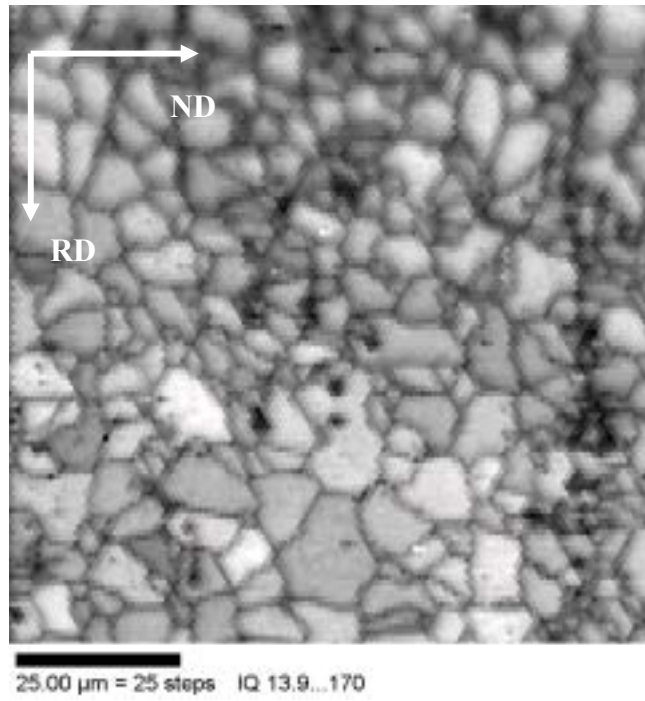
Confidence intervals best measured the degree of reliability of the intervals within each of the various temperatures and times of the annealing matrix. For this study a 95% confidence level was applied. A 95% confidence level implies that 95% of grain sizes within any given image or sample chosen would give an interval that included the mean grain size, $D_{g,mean}$. This would also imply 5% of all samples would yield an erroneous interval. Once again the study used the following equation:

$$D_{g,mean} - 1.96 \frac{\sigma}{\sqrt{n}}, D_{g,mean} + 1.96 \frac{\sigma}{\sqrt{n}} = \text{CI (95\%)} \text{ for } D_{g,mean} \quad (19)$$

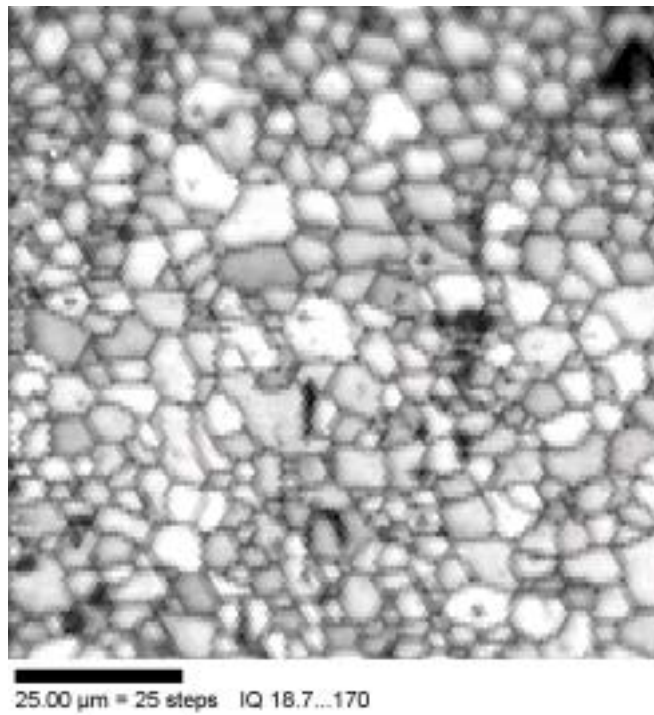
where σ is the population standard deviation, $D_{g,mean}$ is the mean grain diameter and CI stands for the confidence interval. At 500° C samples R, S and T were analyzed for a confidence level of 95%. The mean grain sizes were 7.83 μm , 7.53 μm and 7.99 μm , respectively. The effect of increasing time at 500° C had no effect on grain size because the confidence intervals overlap. The same overlap in confidence intervals was observed for samples U, V and W at 525° C. For samples X, Y and Z at 550° C a 98% CI was calculated. It was determined from the analysis that the although CI's for samples X and Y overlapped, the CI's for samples X and Y did not overlap with the CI for sample Z. The data statistically implies that if the aging treatments are conducted several times between 500° C and 550° C there is a 95% probability that the mean grain sizes within the spread of standard error will overlap for all samples except sample Z. The study was then conducted within the range of temperatures and the same conclusion was reached. The grain size is essentially independent of annealing in samples R, S, T, U, V, W, X and Y. The analysis does show an apparent but very weak dependence of annealing treatment in sample Z. This sample underwent the longest aging time at the highest temperature.

3. Orientation Imaging Microscopy (OIM)

The OIM was also applied as an alternative method of determining grain size in relation to PSN in the TMP; it is important to note that the texture was random for all samples, which is indicative of this recrystallization mechanism. The textures for all samples are included in the appendices. The disorientation angle distributions for all samples also indicated random, high angle boundaries predominate in these microstructures. Fine grains and high angle boundaries support grain boundary sliding. The OIM data was analyzed to provide grayscale grain maps, which were then used to evaluate the grain sizes for comparison to the BSE imaging results. Figure 24 shows grain maps for sample R and sample Z. The image for sample Z confirms the appearance of fine grains as had been determined in the BSE study of grain sizes. Sample Z also appears to give a homogenous microstructure of fine, equiaxed grains that are narrowly distributed in size. Equiaxed grains are characteristic of PSN. The areas scanned for the analysis were all 100 μ m by 100 μ m in size and they were scanned with a step size of 1 μ m. The rolling and normal directions are shown on the figure. The OIM software was used to provide both number-weighted and area-weighted grain size averages. The grain dilation was accomplished in software, and the grain tolerance angle was set at 2 while the minimum grain size was set at 1 pixel. The neighbor correlation was applied. The minimum confidence index was set to 0.1. These values were set to get the most accurate results possible from the OIM data output. The final results are illustrated in Figure 25. Histograms of grain sizes are shown for sample R and sample Z. The histograms suggest that the distribution is narrower for sample Z. The overall number-weighted and area-weighted grain size average is smaller for sample Z but otherwise exhibits no dependence on annealing conditions. The histograms for samples S to Y are shown in the appendix. The distributions are similar for all samples suggesting grain size is essentially independent of annealing time and temperature. Although the variability is greater in the OIM results the effect is essentially the same as was found in the BSE study.



Sample R



Sample Z

(scanned area is 100 microns X 100 microns)

Figure 24. OIM images. Grayscaled Grain Maps. Samples R and Z

Sample	\overline{x} Dg (μm)
R	7.68
S	6.39
T	8.36
U	7.95
V	6.47
W	6.46
X	6.49
Y	8.48
Z	6.35

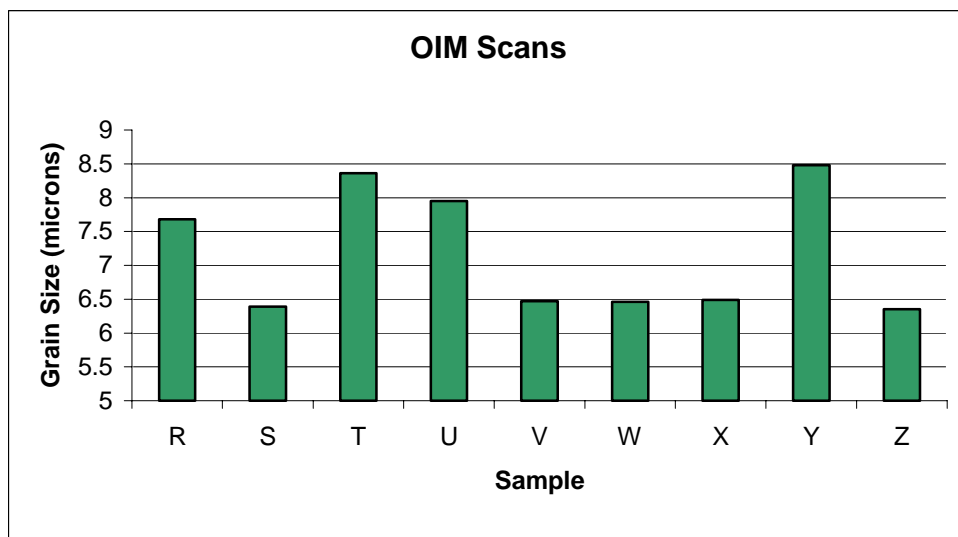


Figure 25. Grain Size Results of OIM Scans

C. PARTICLES AND GRAINS WITHIN THE SCHEME OF PSN

1. Heat Treatments and the Al-Mn Binary Phase Diagram

For the nominal Mg-content of AA5083, the Al-Mg phase diagram (Figure 3) shows that all of the magnesium in AA5083 is in solution during the annealing treatments of this research. The Mn-rich end of the Al-Mn phase diagram is shown in Figure 26; the complete diagram was given in Figure 4. There is a eutectic at 2.0 percent Mn at 658.5° C, a temperature just 1.5 degrees below the freezing point of pure aluminum. The maximum solubility of Mn in the terminal Al solid solution is 1.82 percent at the eutectic temperature. AA5083 is a ternary alloy; the solid solubility of manganese in aluminum is slightly decreased by addition of magnesium. In the Al-Mg alloy of this study the solidus temperature is 576° C; as discussed previously, the annealing temperature was limited to 550° C in order to avoid liquation. The Al-Mn phase diagram was used to estimate the volume fraction of MnAl₆ at the 500° C, 525° C and 550° C annealing temperatures.

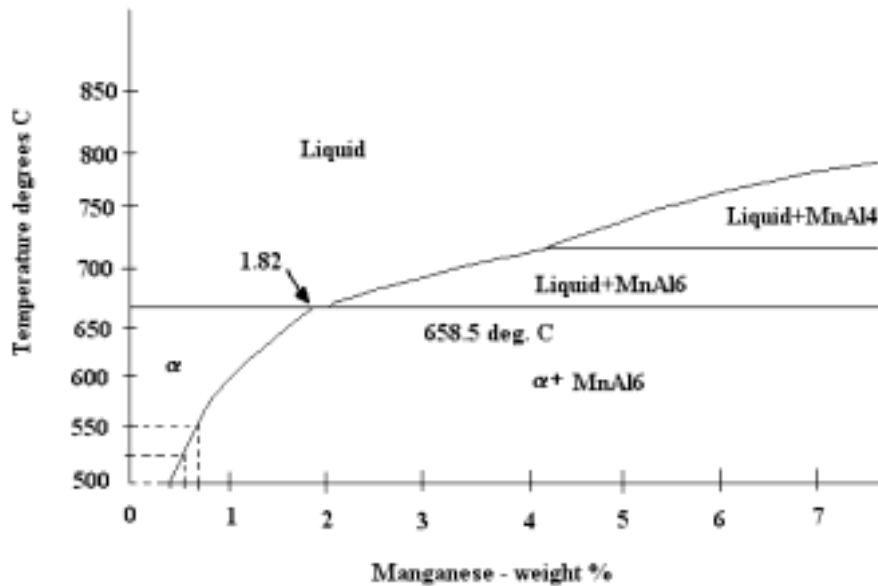


Figure 26. Al-Mn Phase Diagram with Aging Temperatures

2. Volume Fraction Studies

Estimates of the volume fraction of MnAl_6 may be coupled with particle size data to estimate the grain size according to the PSN model. The model assumes that the final grain size, $D_g \approx \lambda/2$, where λ is the particle spacing. This relationship is supported by experimental data; in turn, assuming a regular array of particles, the grain size is given by

$$D_g = \frac{1}{2} d_p \left(\frac{\pi}{6V_f} \right)^{\frac{1}{3}} \quad (10)$$

where d_p is the particle size and V_f is the volume fraction of particles.

OIM texture results for this material support recrystallization by PSN in that random textures are characteristically observed. Figure 27 is a plot of grain size predicted by equation 10 where D_g is the final grain size as a function of volume fraction V_f of particles. Experimental grain size values for the various annealing temperatures are plotted versus the volume fractions V_f estimated from the phase diagram; grain size values for number weighting of the data are plotted as open symbols and for area weighting are plotted as filled symbols. Because of the size distribution of the grains it is unclear what measure of grain size that correlates most closely with the particle spacing data. The dashed lines represent the standard error of the data. This plot suggests that grain size and volume fraction data are consistent for PSN of recrystallization at particles $3.5\mu\text{m} - 5\mu\text{m}$ in size or larger.

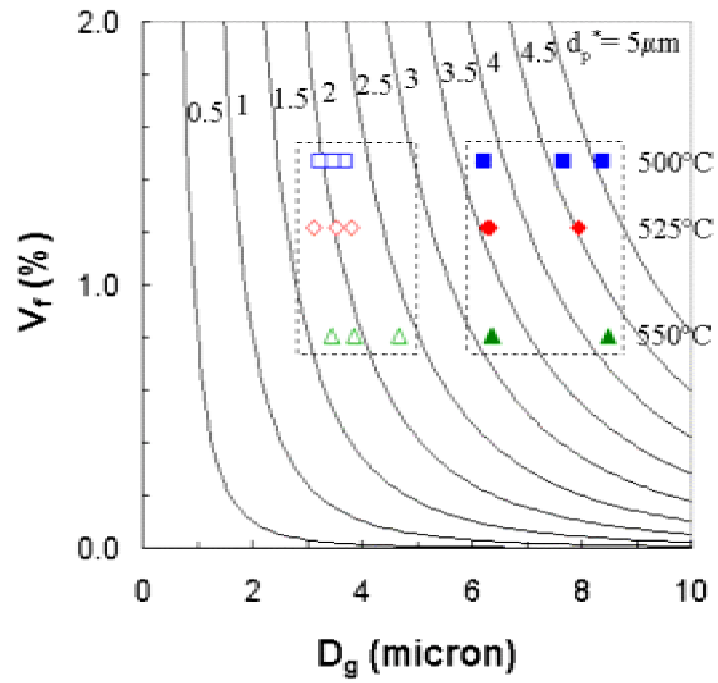


Figure 27. Phase Diagram Volume Fraction of Particles

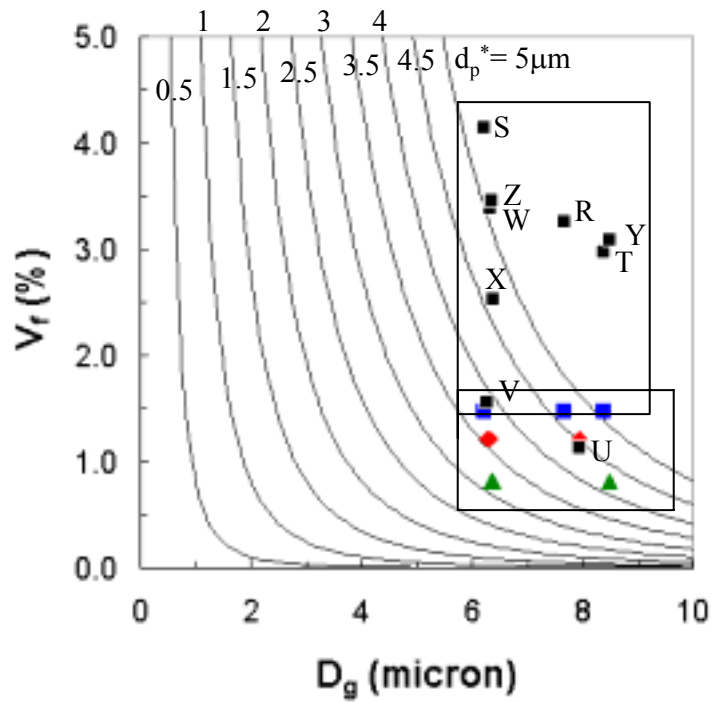


Figure 28. Volume Fraction vs. Final Grain Size

Temperature (°C)	V _f (%)
500	1.471
525	1.218
550	0.808

Table 4. **Volume Fractions acquired from Al-Mn Phase diagram**

Temp (°C)	Sample	d _p (μm)	D _g (μm)	# (d _p >d _p *)
500	R	1.135	7.681	2
500	S	1.159	6.225	9
500	T	1.213	8.385	1
525	U	1.130	7.947	0
525	V	1.252	6.284	5
525	W	1.358	6.322	7
550	X	1.128	6.322	12
550	Y	1.244	8.481	4
550	Z	1.292	6.351	16

d_p*=3μm

Table 5. **Particle Sizes and Grain Sizes from Volume Fraction Plot**

Table 4 summarizes the volume fraction data and Table 5 summarizes estimates based on a critical particle size of $3\mu\text{m}$. This data suggests that the majority of second phase particles do not participate as sites of nucleation and recrystallization.

Instead of using estimates of volume fractions of particles from phase diagram data the area fractions from each of the images may be used to determine corresponding volume fractions [Ref. 34]. Figure 28 represents the volume fraction plot using the distribution of area-weighted grain sizes based on image-area fractions. There is significant spread in the data. Clearly, the assumptions made in the PSN model have a large impact on the calculated final grain size, D_g . In examining all of the data, the experimental particle size distributions varied little with overaging and so the fact that the grain size also varies little is consistent with this. It is noteworthy that sample Z, which was aged at the highest temperature of 550°C for a period of 100 hours, had the smallest grain size and the largest number of particles greater than a value of $d_p^* \approx 3.0\mu\text{m}$.

If the critical particle size, d_p^* , is reduced then the resulting grain sizes will be finer as shown in figure 29. This may be accomplished by introducing greater strains in the cold rolling operations prior to recrystallization, although this may be impractical in an industrial sense. In this study, samples were reduced by 80% corresponding to a true strain of 1.25. The final thickness of the recrystallized samples was $\sim 1\text{mm}$. However, a larger strain to produce a thinner final sheet, e.g., 0.5 mm final thickness, would entail a smaller critical particle size thus increasing the number of particles that are involved in nucleation. This would enable a better test of the PSN model.

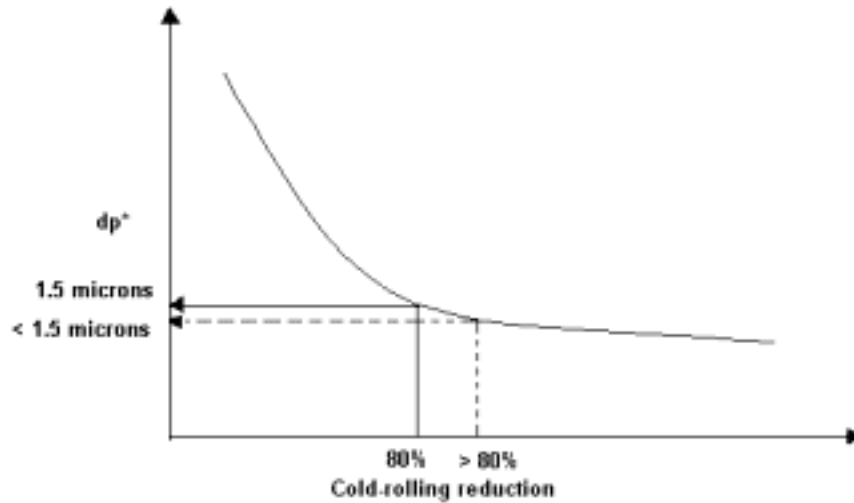


Figure 29. Increased strain to decrease d_p^*

3. Particle Spacing within the PSN Model

The PSN model was derived assuming a uniform size and a regular distribution of particles in a cubic array in space, and that all act as nucleation sites. Then, the grain size is approximately half the particle spacing [Ref. 20]. Computer simulations of random particle distributions have shown that such distributions approach the Poisson distribution for dilute (i.e., area or volume fractions < 0.05) dispersions, and that the average spacing in such dispersions is about one-half that of a cubic array [Ref. 35]. This result applied whether the particles were of uniform size, or log-normally distributed in size [Ref. 35]. On this basis, equation 10 can be viewed only as an estimate accurate only to within a factor of two to four.

4. Particle Distributions and the Critical Particle Size

The annealing treatments evidently failed to place the MnAl_6 back into solution and thus the particle distribution remained highly non-uniform. Texture data for the GICC material are consistent with PSN, but comparison of the grain size and particle size data suggest that most of the second phase particles do not participate as sites for nucleation of recrystallization. Continuing to increase prior strain during rolling is an option but would require altering the hot band thickness if the final sheet thickness is to remain constant.

Control of the second-phase particle distribution is necessary if improved grain size control is to be attained through the PSN model. The model ultimately relies on the idea that there is a critical size, d_p^* , above which the particles are sites for PSN. This is illustrated in Figure 30 for three theoretical particle size distributions, which are labeled I, II and III. It is assumed that d_p^* is the same for all three distributions. Assuming that only particles with diameters of greater than d_p^* participate in PSN, more particles may become nucleation sites in distribution III, despite a larger mean particle size and a smaller total number of particles in the microstructure. In the current investigation, prolonged annealing had little effect on the distribution, i.e., I compared to II, and, consequently, little effect on the number of nucleating particles. This may be seen in the calculated probability density function (PDF) plots for all the data of this research as shown in Figure 31. In this representation, a value of $d_p^* \approx 3.0\mu\text{m}$ is assumed. Essentially the same number of particles exceed this size in all distributions and so little effect of the overaging anneals is anticipated.

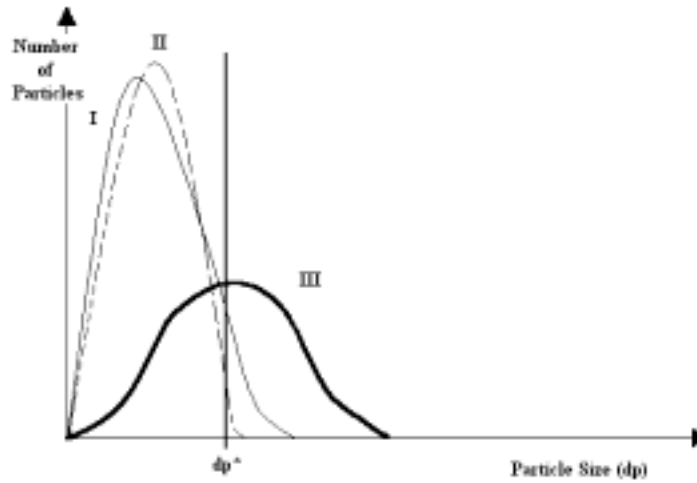


Figure 30. Theoretical Precipitate Distributions

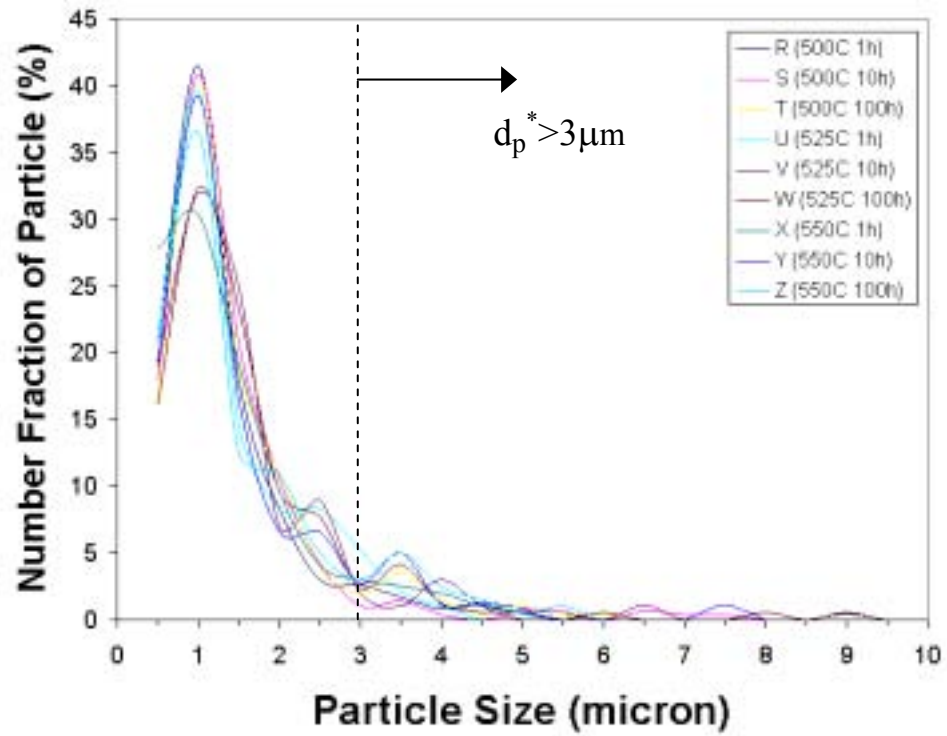


Figure 31. Superimposed Particle Fractions

In Figure 31, the PDFs are smoothed representations of the particle fraction histograms and the oscillations at large particle sizes are artifacts of the smoothing. Also, due to resolution limitations in the SEM particles smaller than $0.5\mu\text{m}$ are not included. Again, this plot clearly shows that the majority of second phase particles do not participate as sites for nucleation of recrystallization. Also, the distribution vividly illustrates that the TMP essentially had no effect on the MnAl_6 particles within the G1CC AA5083 material.

Altogether, the data of this research suggest that alternative methods of control of the particle size distribution be sought. These may include alloy modifications to enable the Mn to be fully re dissolved or modified melting and casting procedures, again with a view to improving control of the particle size distribution. Finally, use of larger or smaller strains during rolling would provide an alternative method of assessing the validity of the PSN model for grain size control in this alloy.

V. CONCLUSION

A. CONCLUSION

1. The MnAl_6 particles largely formed during the casting process and formed large clusters.
2. Most of the MnAl_6 had already precipitated out during solidification and so very little additional Mn was available to precipitate during the annealing treatments. The MnAl_6 that had already precipitated out coarsened only slightly during the aging at 550°C .
3. The annealing treatments at 500°C and 525°C essentially had no effect on the distribution of particles.
4. A rolling strain of 1.25 after the annealing treatments was sufficient to obtain refinement to grain sizes of $\sim 7\mu\text{m}$.
5. Grain size was almost independent of annealing time and temperature. The MnAl_6 particles are extremely stable and require a very high-temperature aging treatment to coarsen the particles.

B. RECOMMENDATIONS FOR FURTHER STUDY

1. Apply a different casting process which precipitates as little MnAl_6 as possible during solidification.
2. Continue to collect more data with the longer and high-temperature annealing treatments. There seemed to be relatively weak effect on both particle distribution and grain size control as was seen in sample Z.
3. Examine other aluminum alloys with less magnesium which would in turn raise the solidus temperature and enable the study of aging treatments above 600°C .
4. Induce greater strains in as much as practically possible. A 1.25 strain for an 80% cold reduction was induced on the G1CC material in this study. Recommend inducing additional strain up to a 90% cold reduction to achieve a final thickness of 0.5 mm in the G1CC hot band material.

APPENDIX A. OPTICAL MICROSCOPY

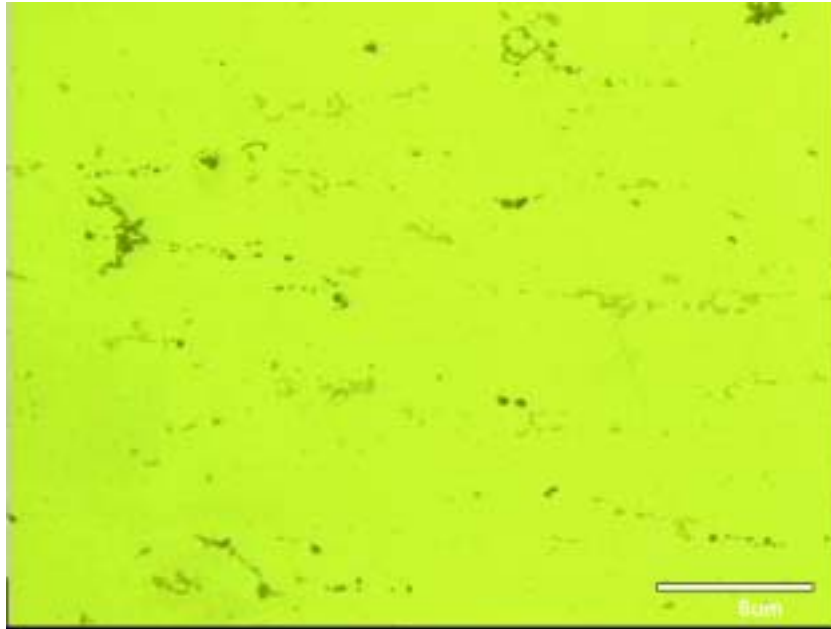


Figure 34. Sample S. Aged 500° C, 10 hours. 750X

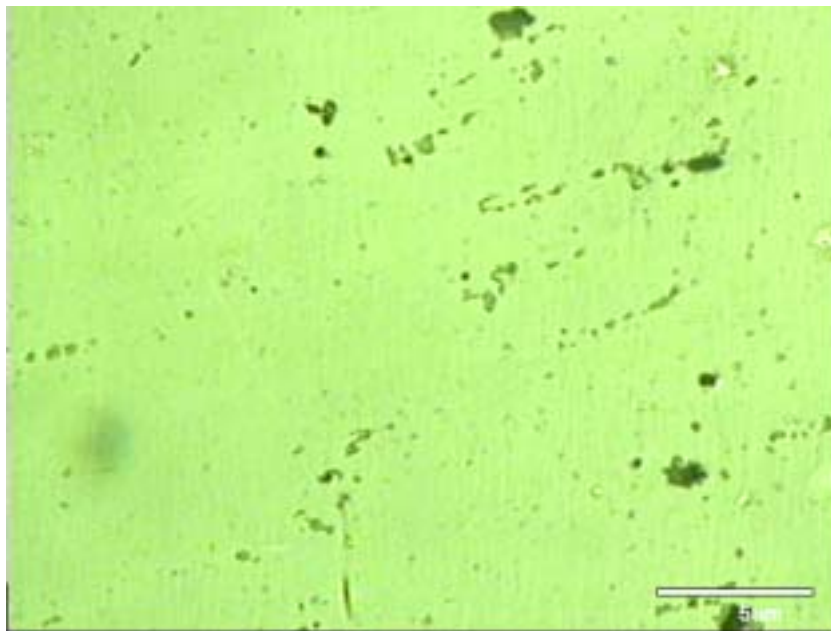


Figure 32. Sample T. Aged 500° C, 100 hours. 750X

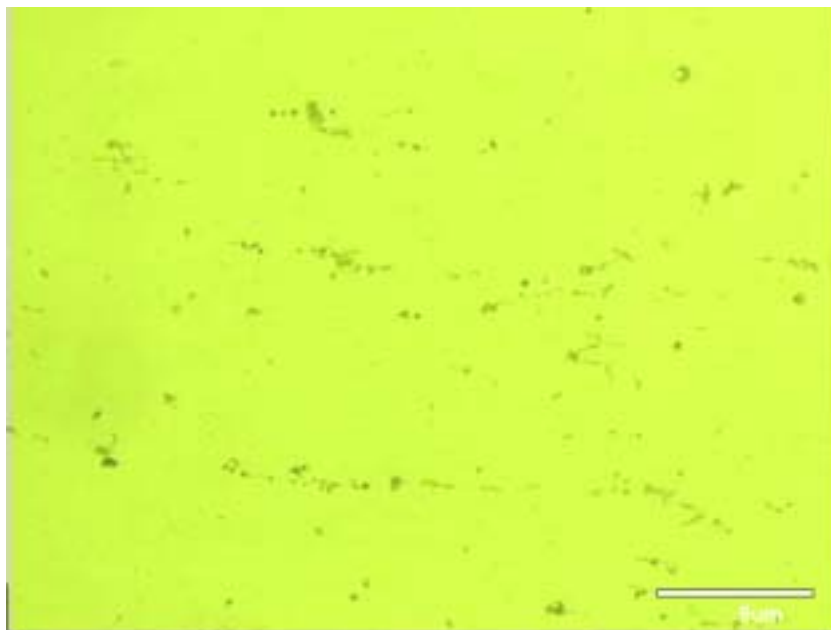


Figure 33. Sample U. Aged 525° C, 1 hour. 750X

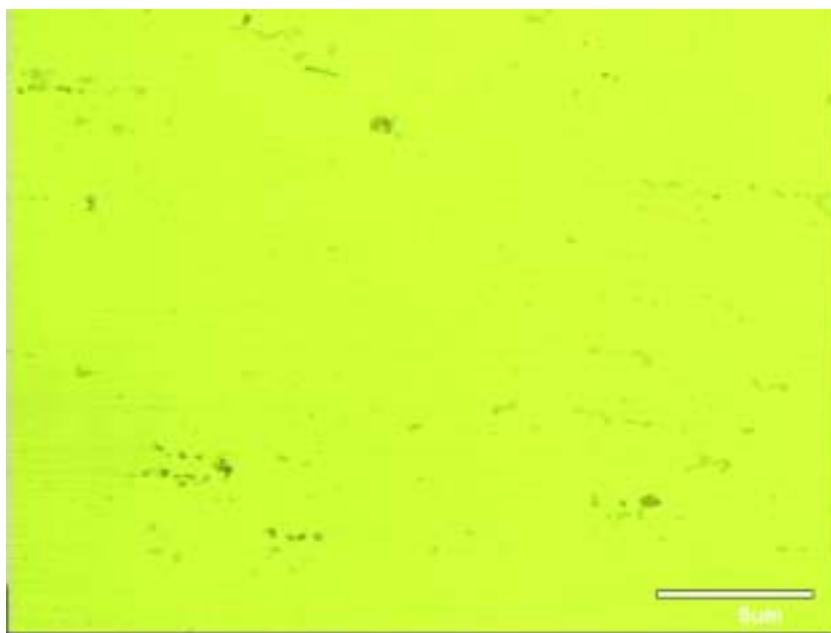


Figure 34. Sample V. Aged 525° C, 10 hours. 750X

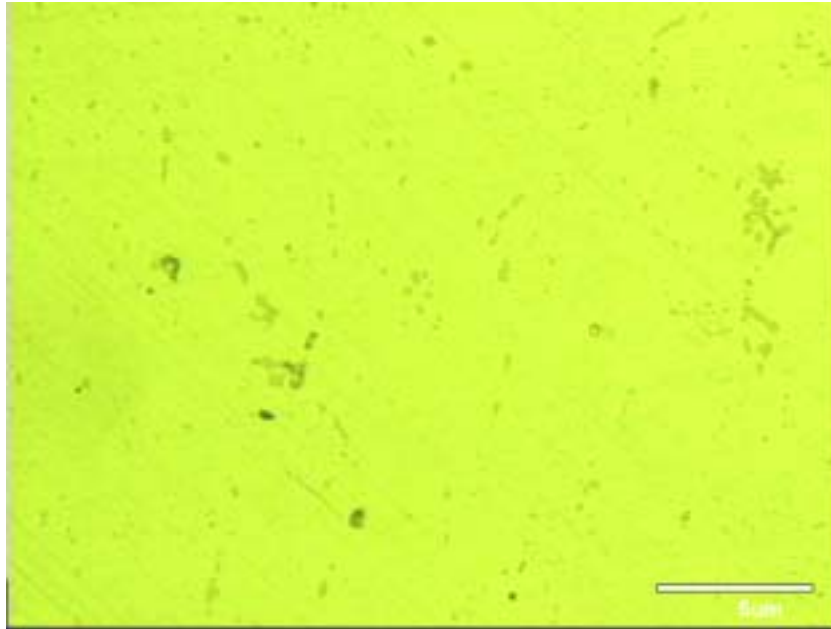


Figure 35. Sample W. Aged 525° C, 10 hour. 750X

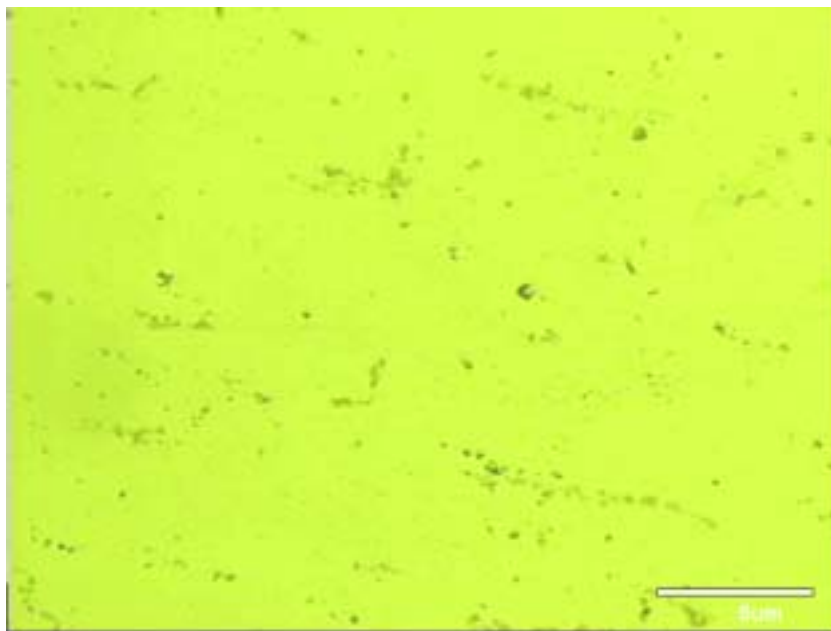


Figure 36. Sample X Aged 550° C, 1 hour. 750X

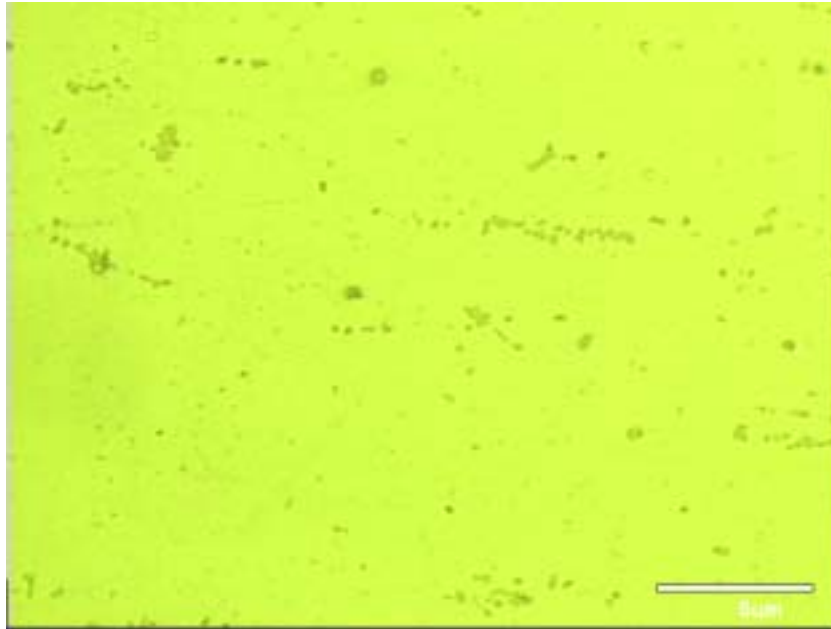


Figure 37. Sample Y. Aged 550° C, 10 hours. 750X

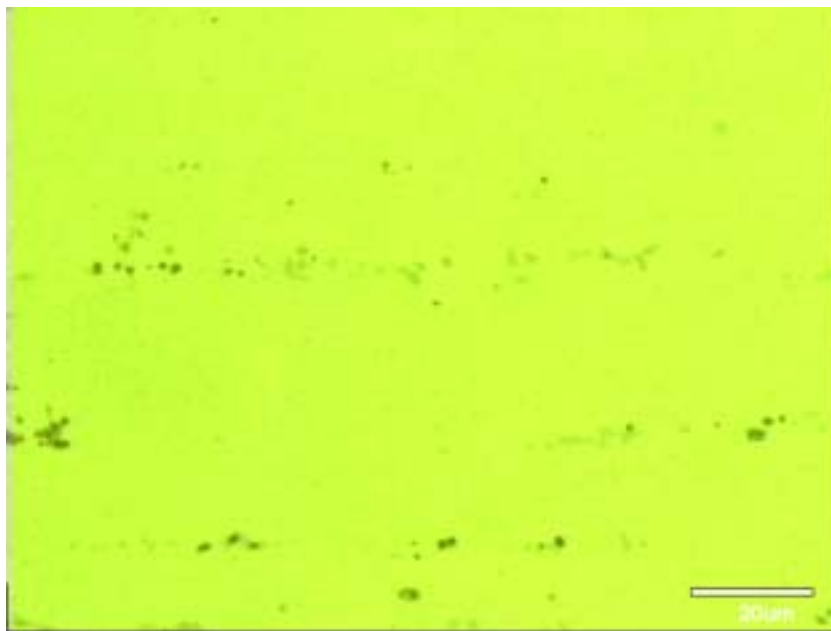


Figure 38. Sample S. Aged 500° C, 10 hours, 80% CW, ReX. 1500X

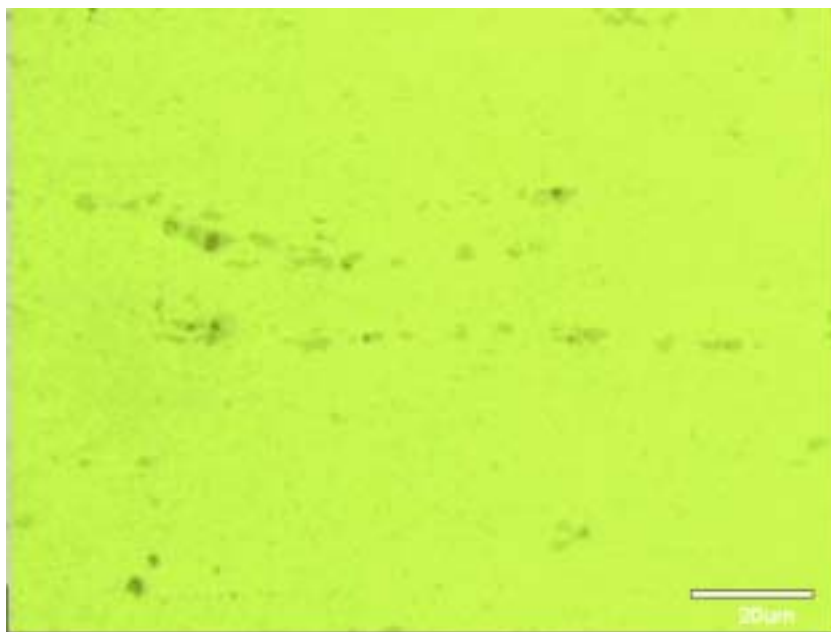


Figure 39. Sample T. Aged 500° C, 100 hours, 80% CW, ReX. 1500X

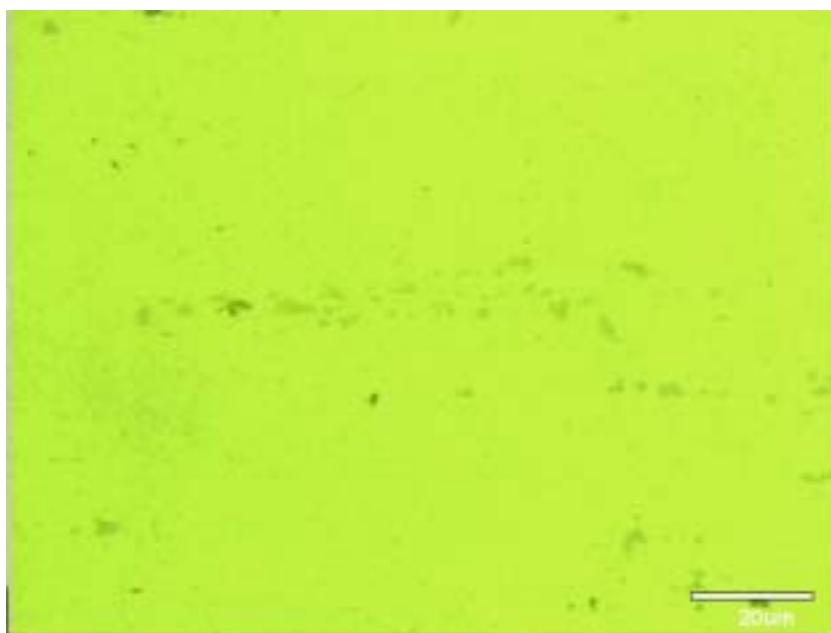


Figure 40. Sample U. Aged 525° C, 1 hour, 80% CW, ReX. 1500X

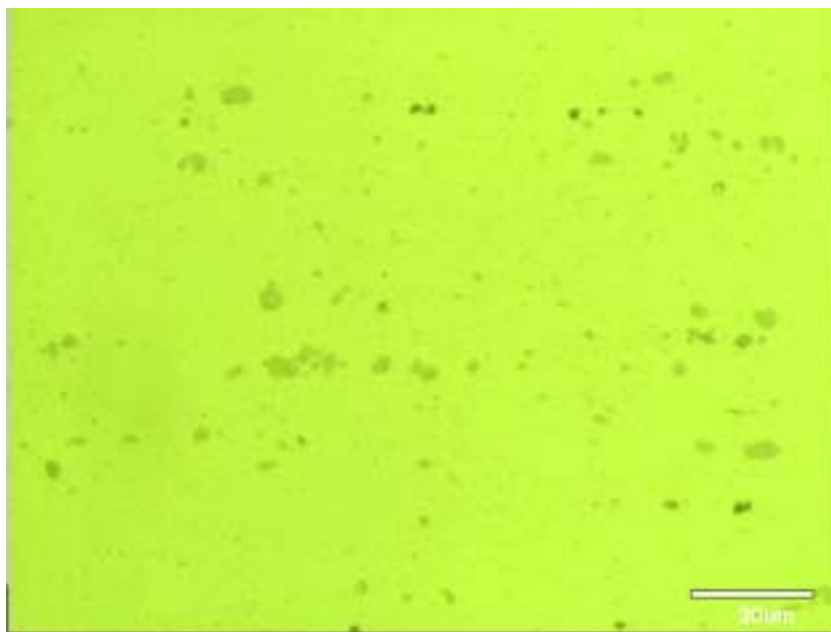


Figure 41. Sample V. Aged 525° C, 10 hours, 80% CW, ReX. 1500X

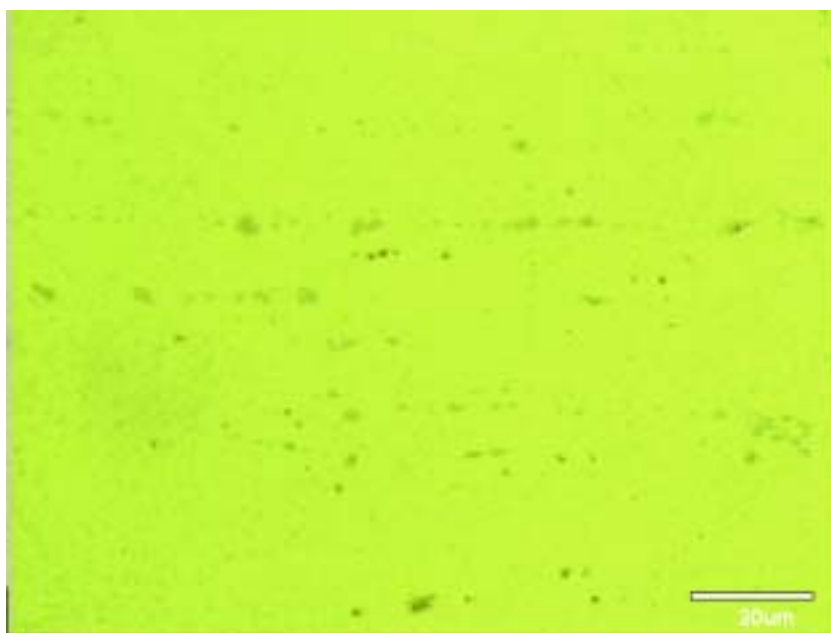


Figure 42. Sample W. Aged 525° C, 100 hours, 80% CW, ReX. 1500X

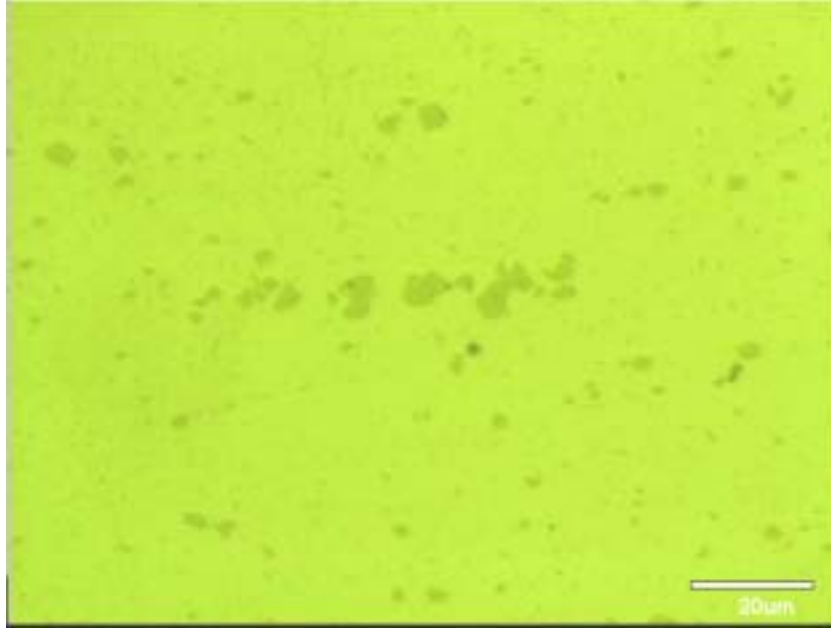


Figure 43. Sample X. Aged 550° C, 1 hour, 80% CW, ReX. 1500X

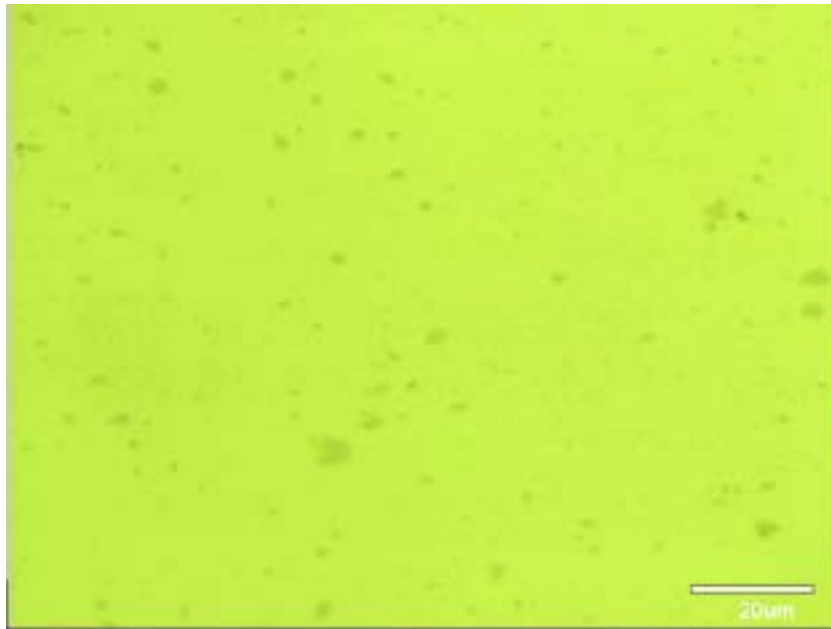


Figure 44. Sample Y. Aged 550° C, 10 hours, 80% CW, ReX. 1500X

THIS PAGE INTENTIONALLY LEFT BLANK

APPENDIX B. BSE IMAGES (PARTICLES)

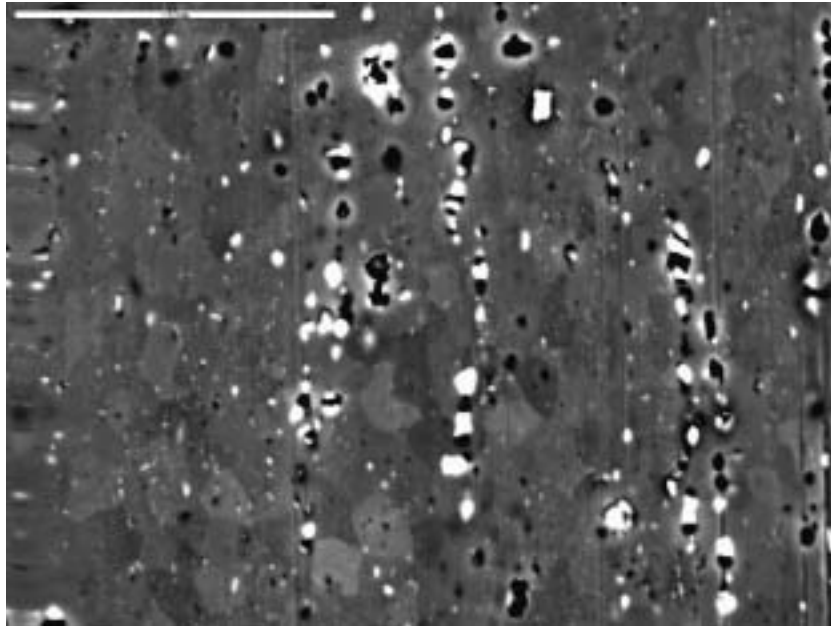


Figure 45. Sample S. Aged 500° C, 10 hours. 1000X

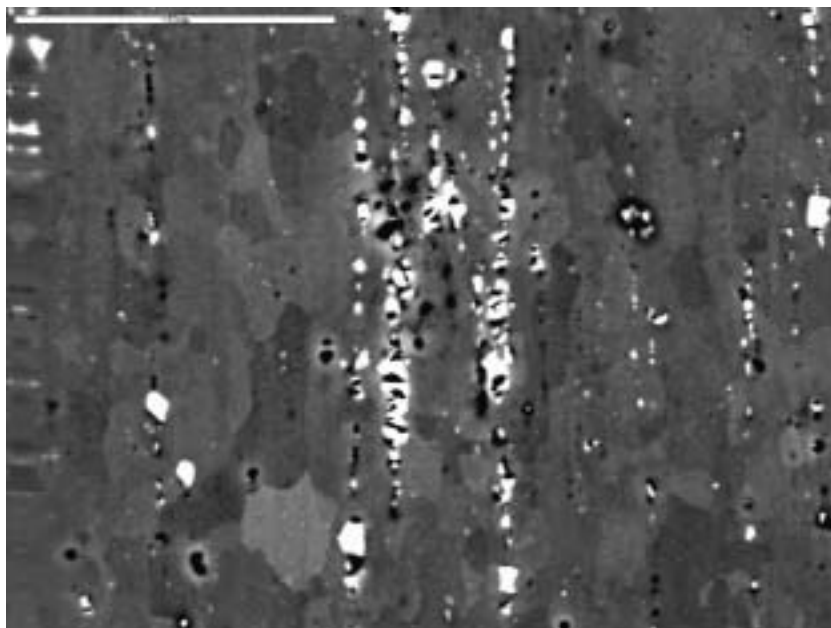


Figure 46. Sample T. Aged 500° C, 100 hours. 1000X

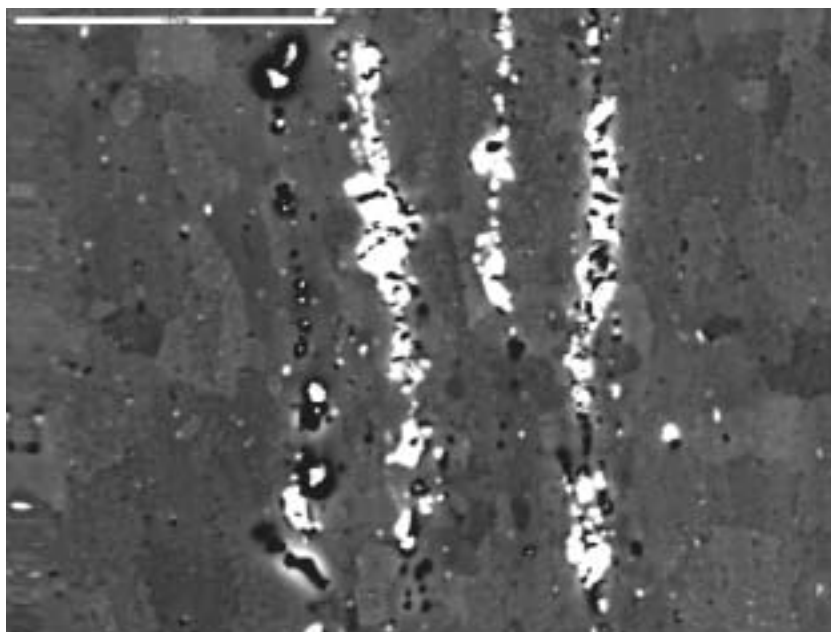


Figure 47. Sample U. Aged 525° C, 1 hour. 1000X

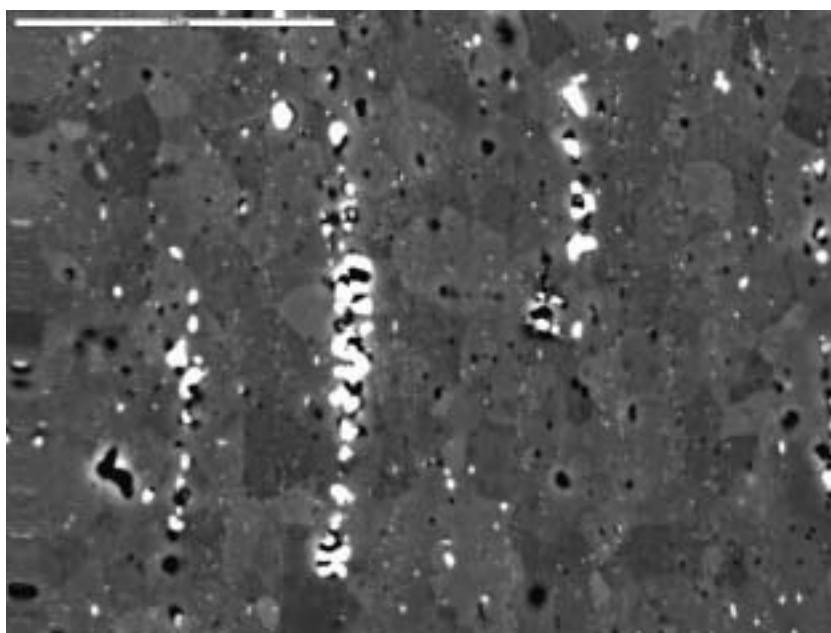


Figure 48. Sample V. Aged 525° C, 10 hours. 1000X

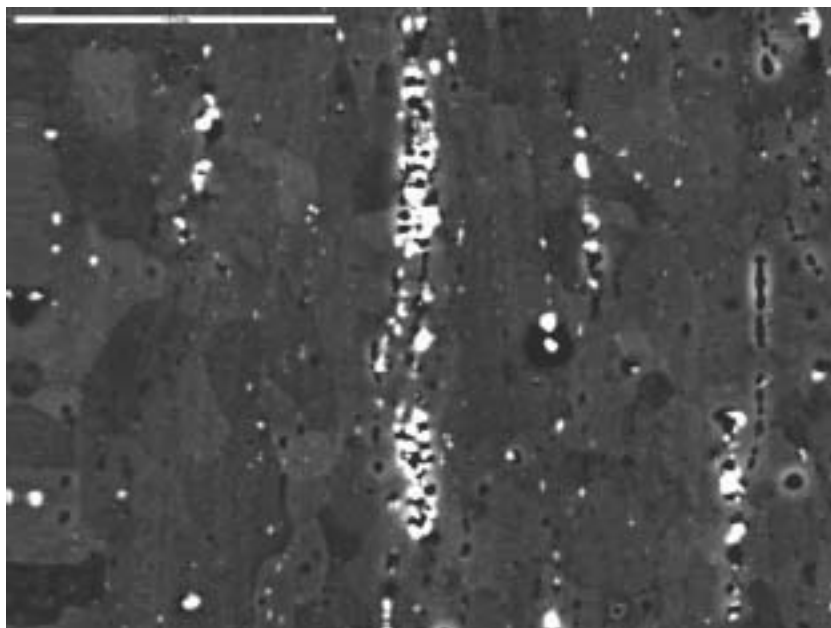


Figure 49. Sample W. Aged 525° C, 10 hour. 1000X

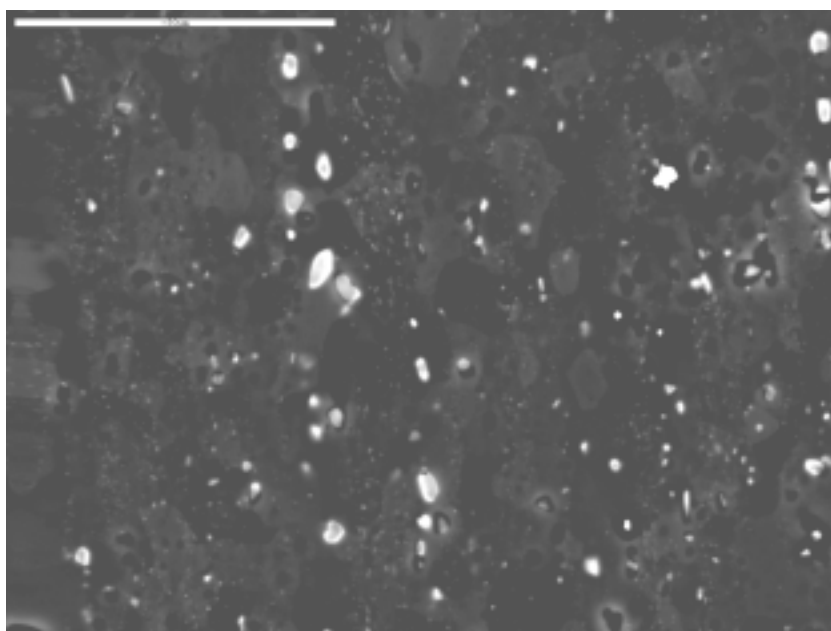


Figure 50. Sample X Aged 550° C, 1 hour. 1000X

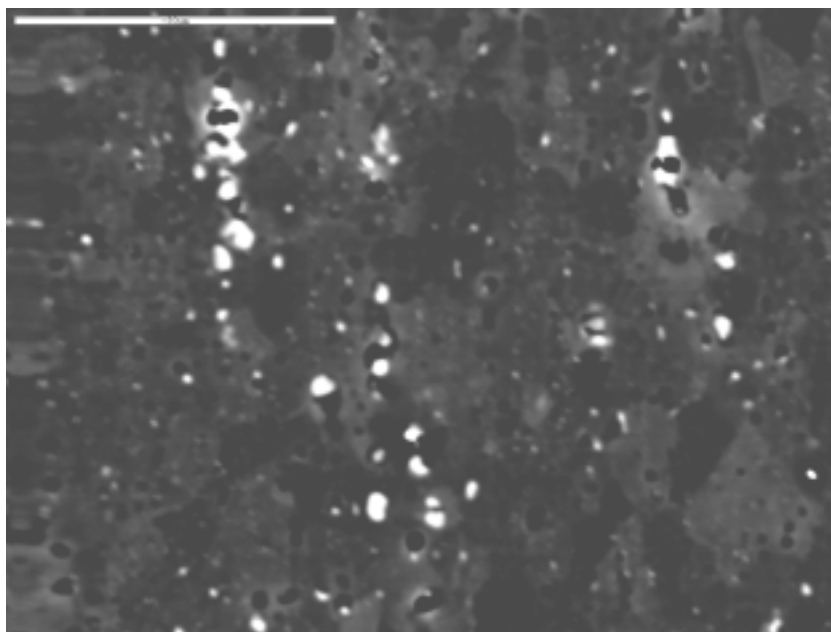


Figure 51. Sample Y. Aged 550° C, 10 hours. 1000X

APPENDIX C. PARTICLE FRACTION CHARTS (PARTICLES)

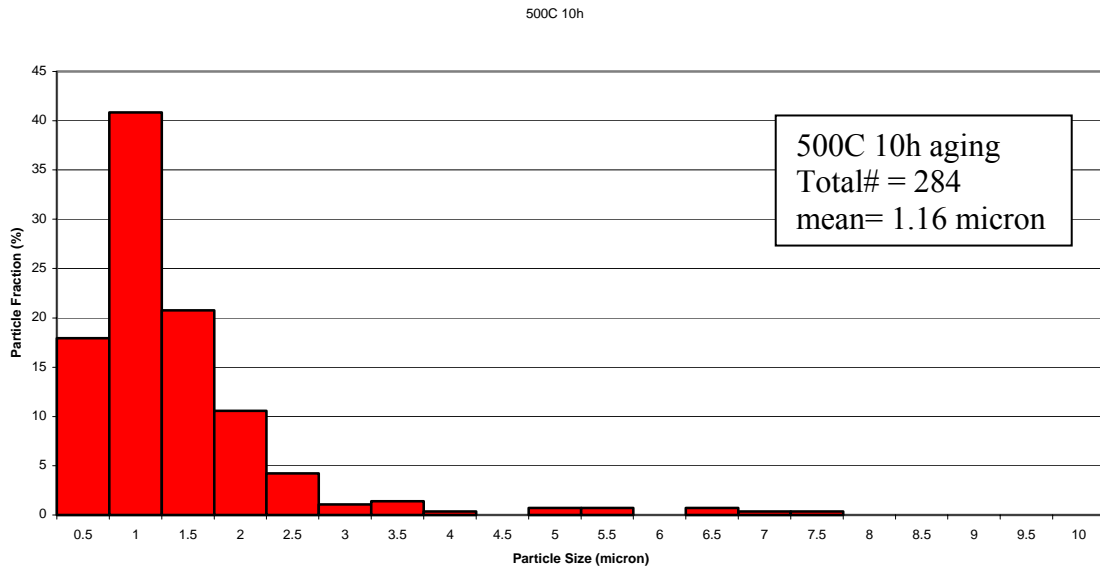


Figure 52. Sample S. Aged 500° C, 10 hours, 80% CW, ReX.

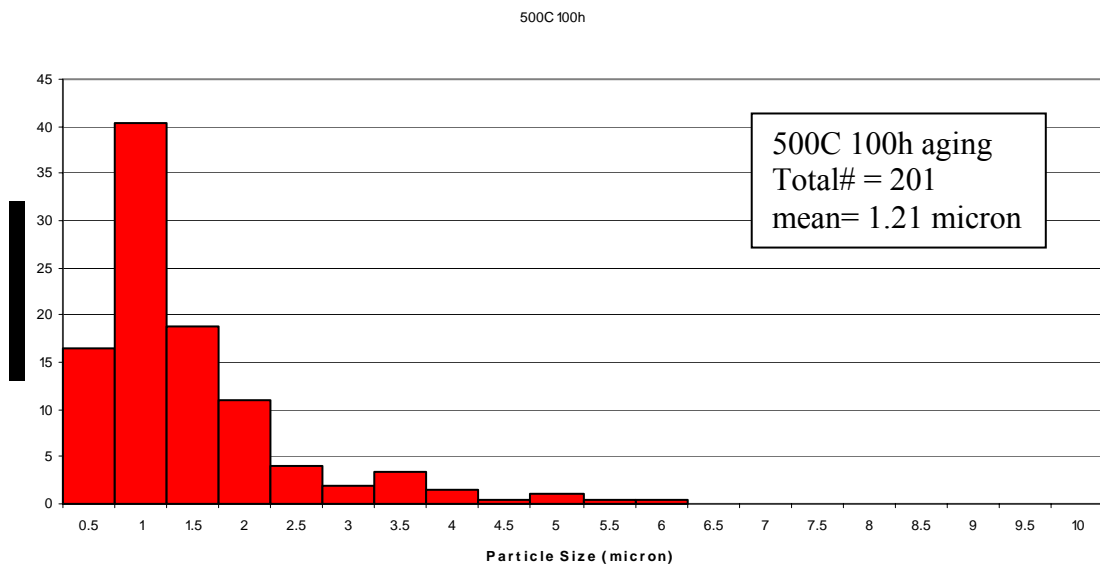


Figure 53. Sample T. Aged 525° C, 1 hour, 80% CW, ReX.

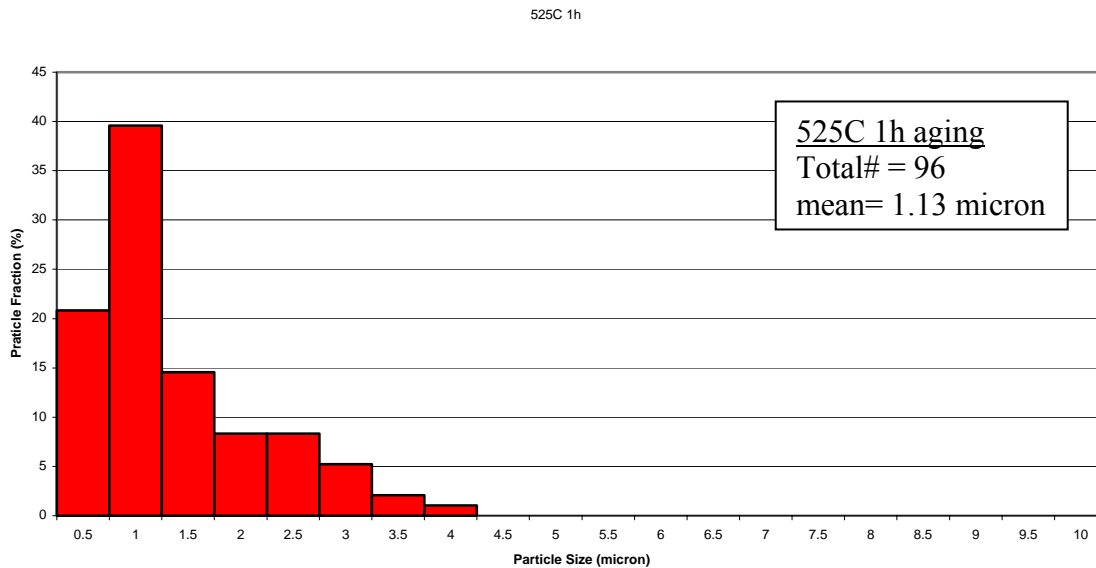


Figure 54. Sample U. Aged 525° C, 1 hour, 80% CW, ReX.

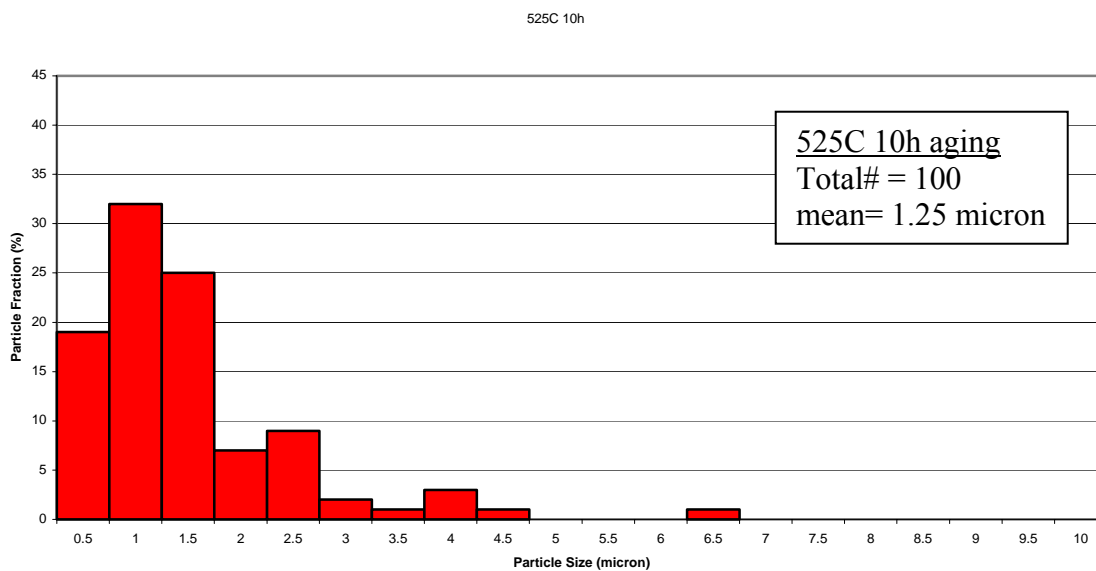


Figure 55. Sample V. Aged 525° C, 10 hours, 80% CW, ReX.

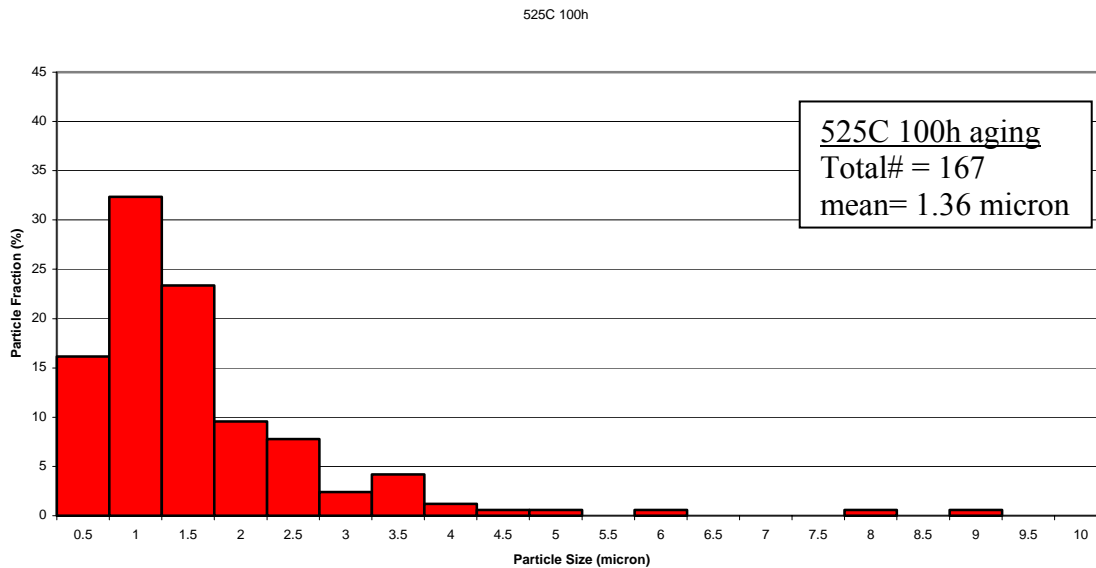


Figure 56. Sample W. Aged 525° C, 100 hours, 80% CW, ReX.

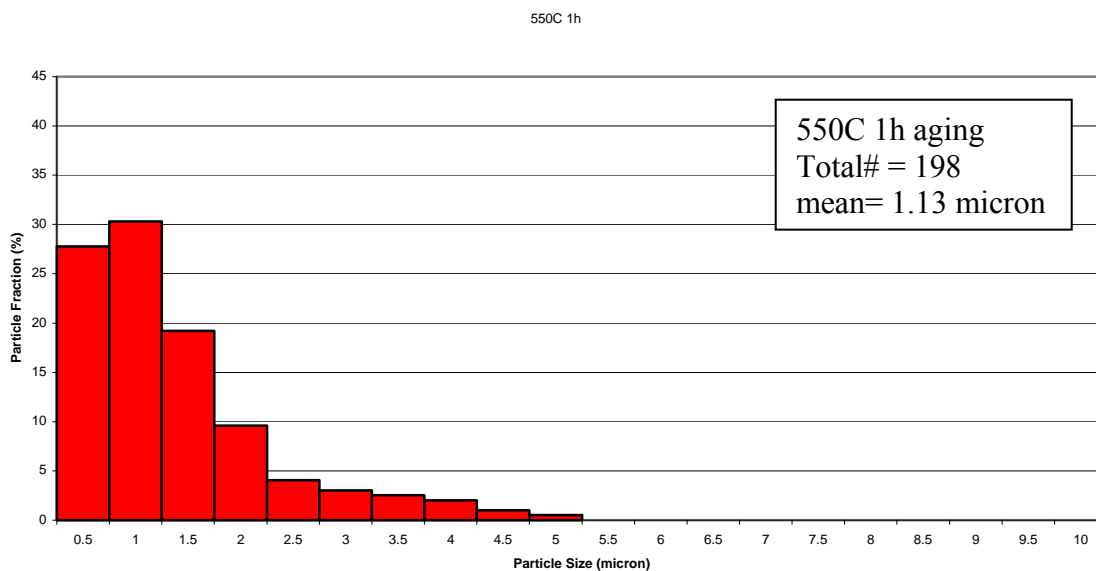


Figure 57. Sample X. Aged 550° C, 1 hour, 80% CW, ReX.

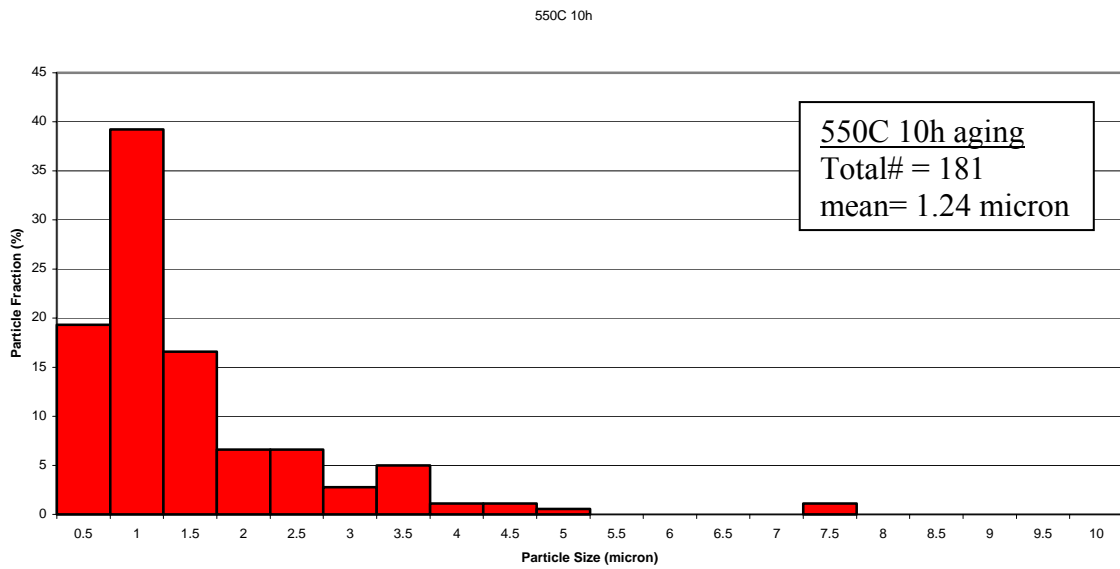


Figure 58. Sample Y. Aged 550° C, 10 hours, 80% CW, ReX.

APPENDIX D. BSE IMAGES (GRAINS)

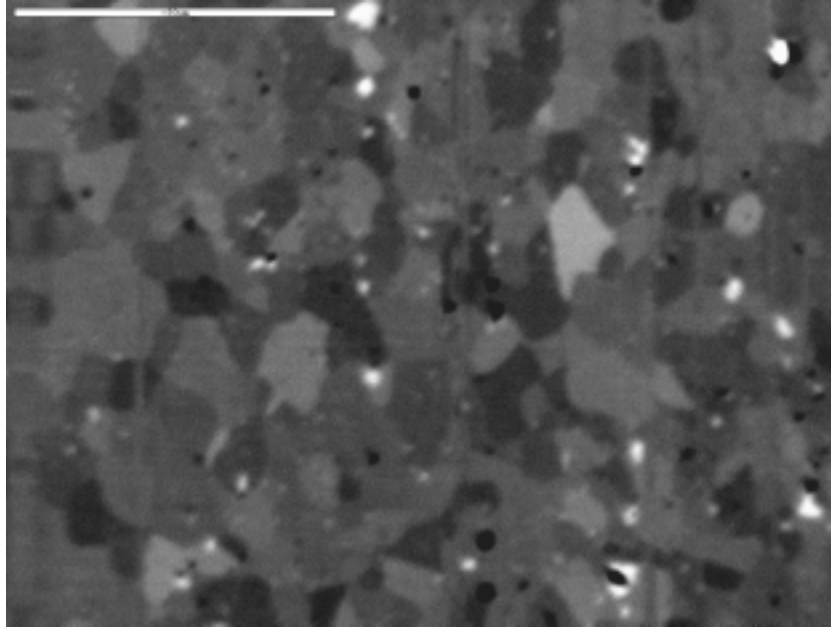


Figure 59. Sample S. Aged 500° C, 10 hours, 80% CW, ReX. 1000X

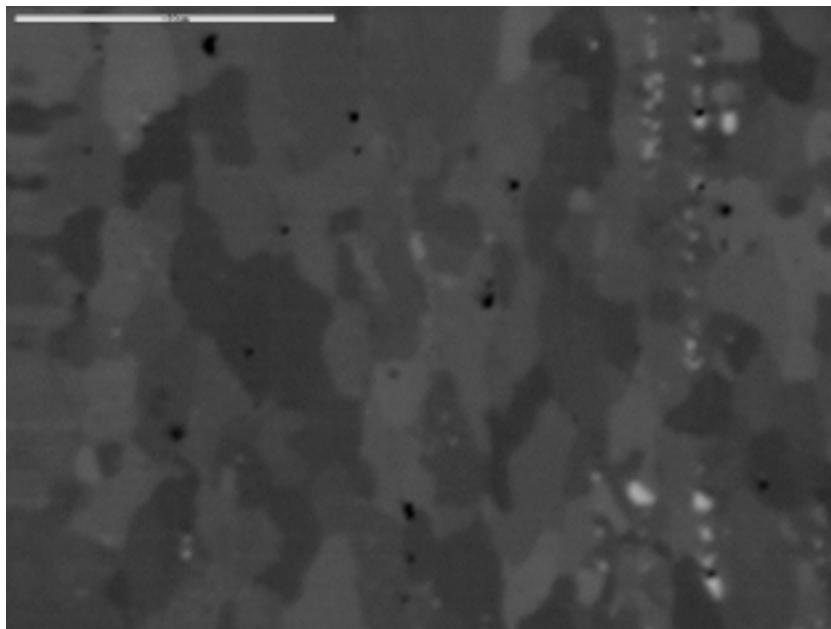


Figure 60. Sample T. Aged 500° C, 100 hours, 80% CW, ReX.

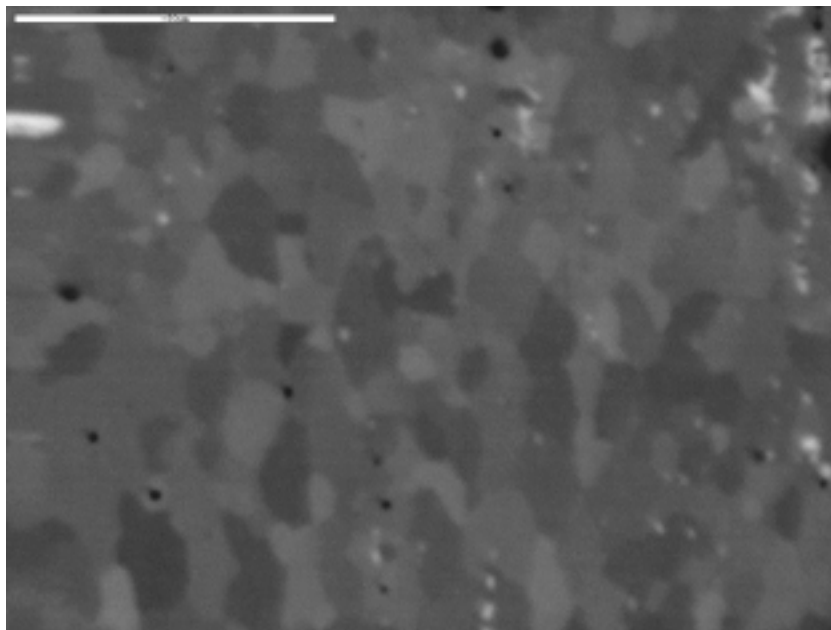


Figure 61. Sample U. Aged 525° C, 1 hour, 80% CW, ReX. 1000X

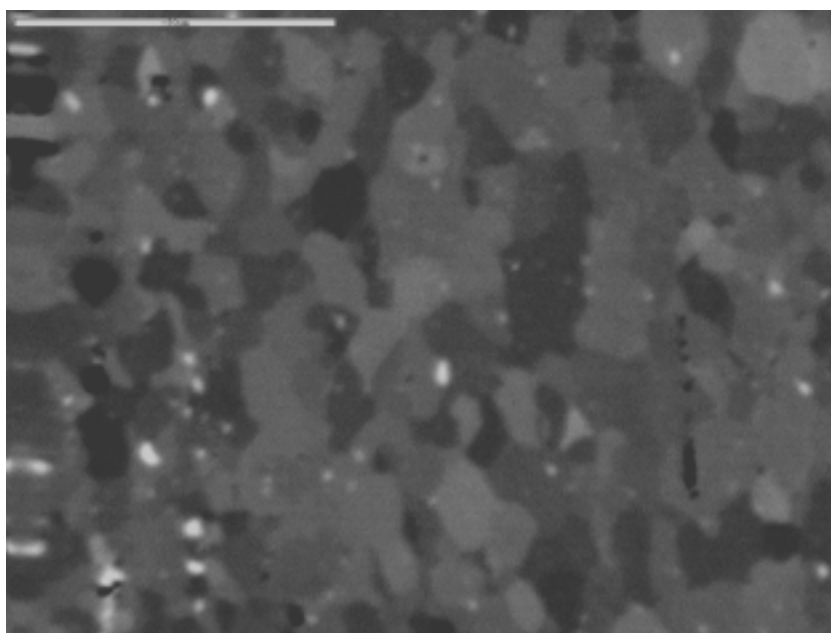


Figure 62. Sample V. Aged 525° C, 10 hours, 80% CW, ReX. 1000X

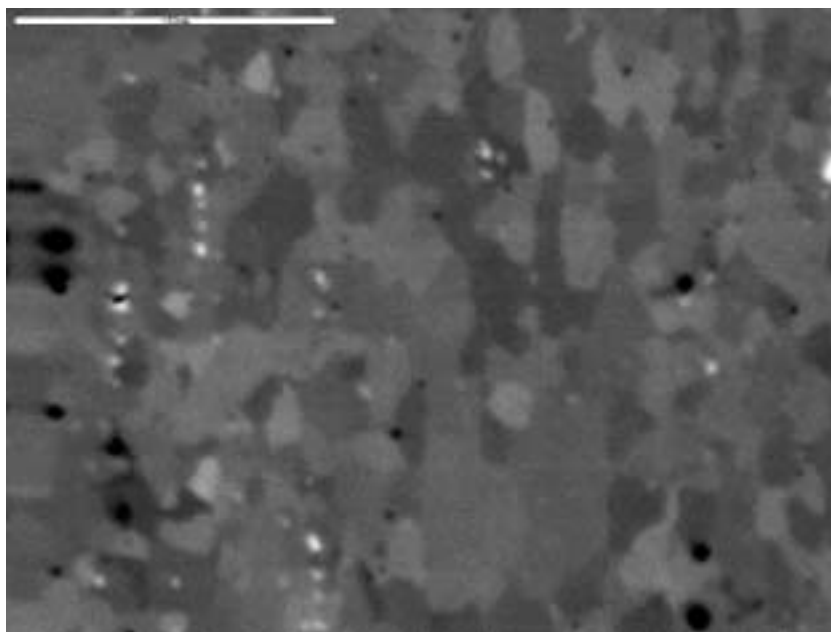


Figure 63. Sample W. Aged 525° C, 100 hours, 80% CW, ReX. 1000X

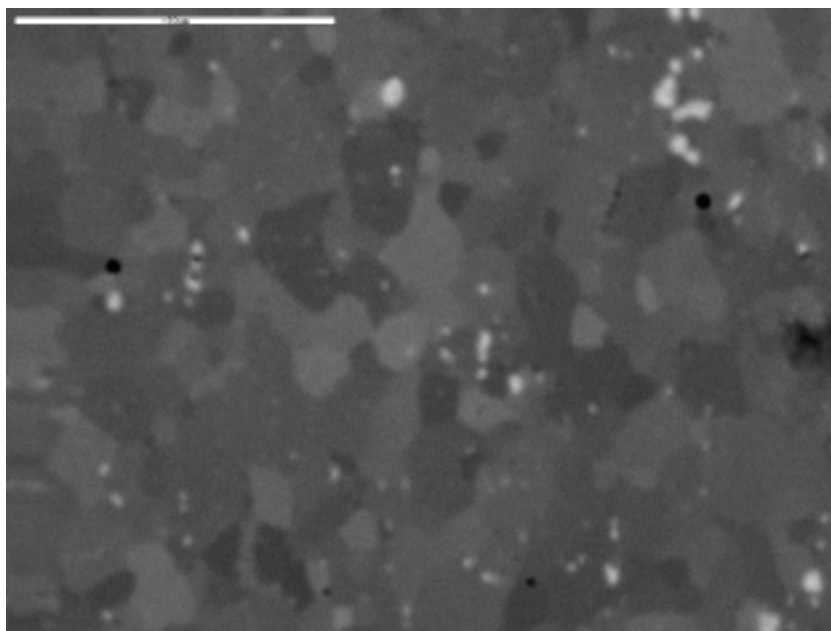


Figure 64. Sample X. Aged 550° C, 1 hour, 80% CW, ReX. 1000X

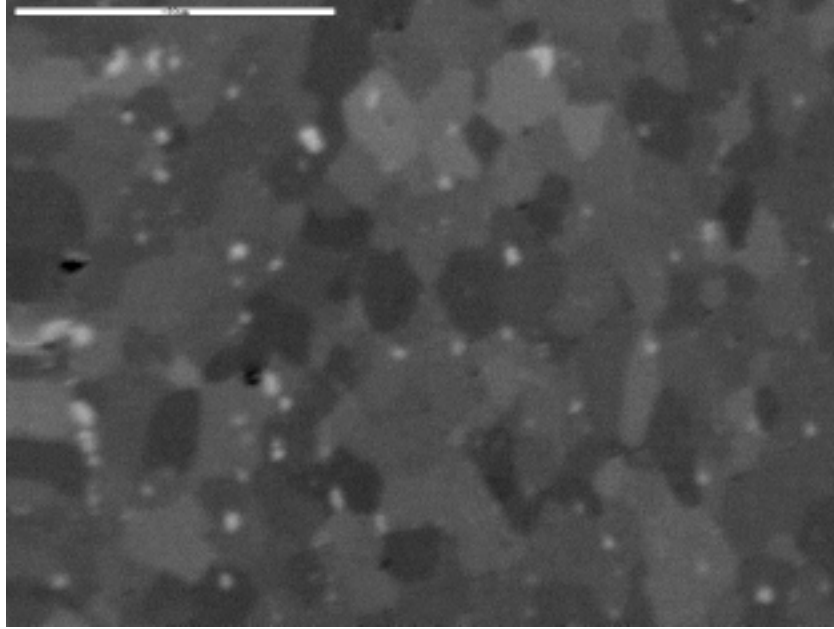


Figure 65. Sample Y. Aged 550° C, 10 hours, 80% CW, ReX. 1000X

APPENDIX E. BSE GRAIN SIZE CHARTS

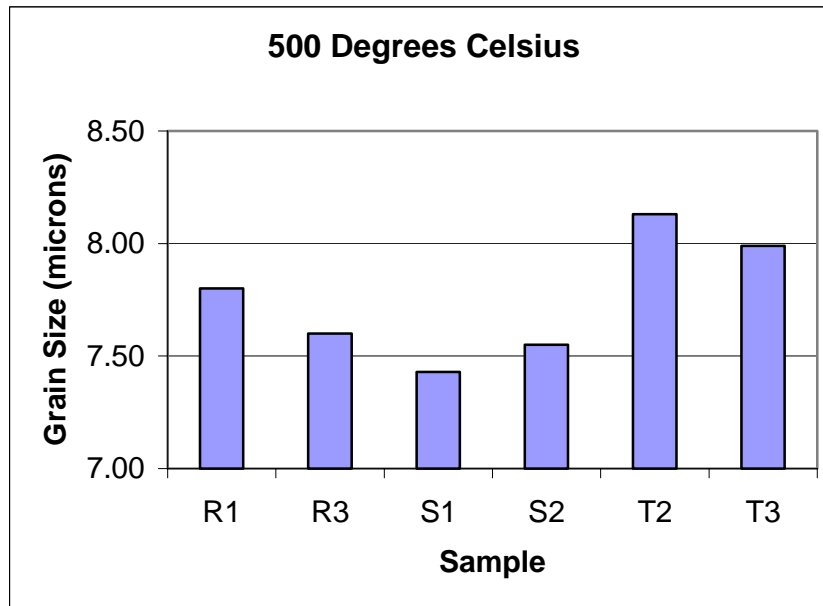


Figure 66. Grain Size Comparison at 500° C, 80% CW, ReX.

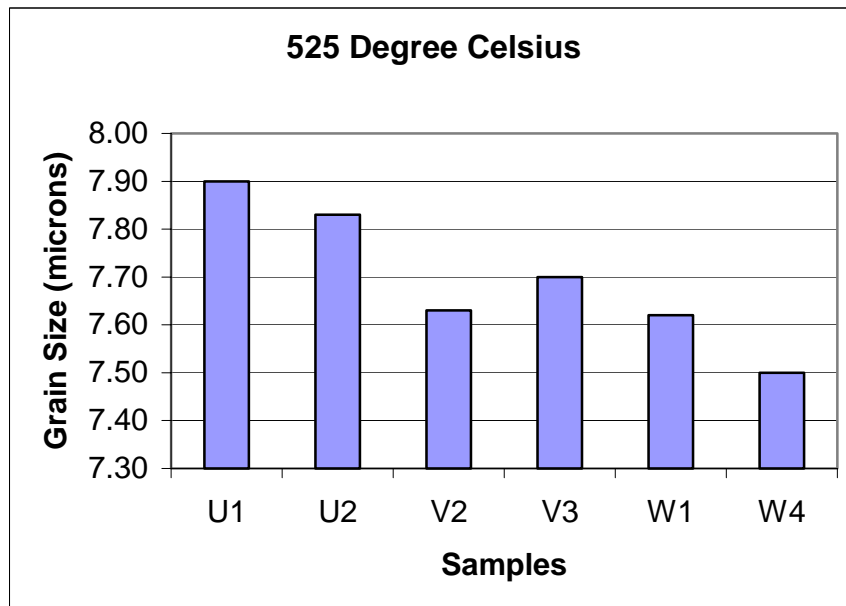


Figure 67. Grain Size Comparison at 525° C, 80% CW, ReX.

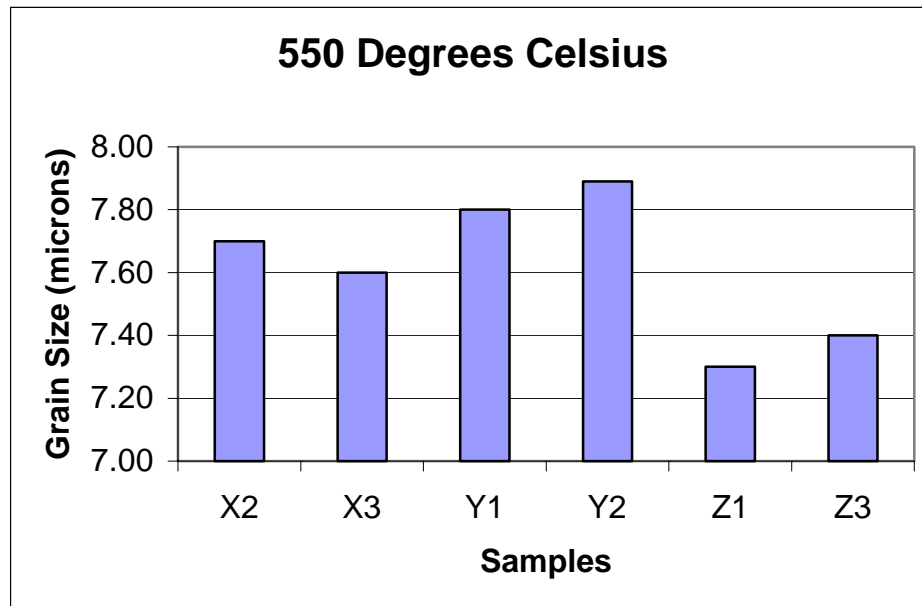


Figure 68. Grain Size Comparison 550° C, 80% CW, ReX.

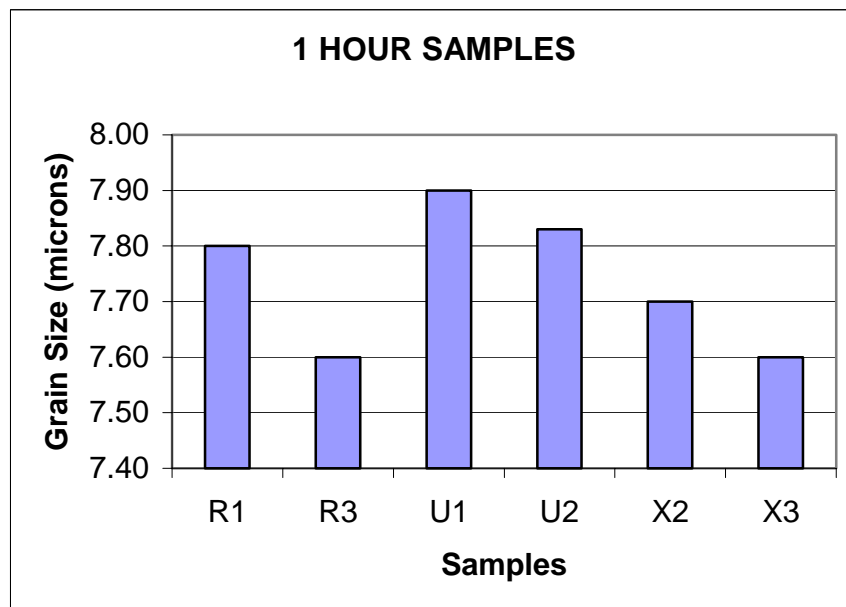


Figure 69. Grain Size Comparison for hour, 80% CW, ReX.

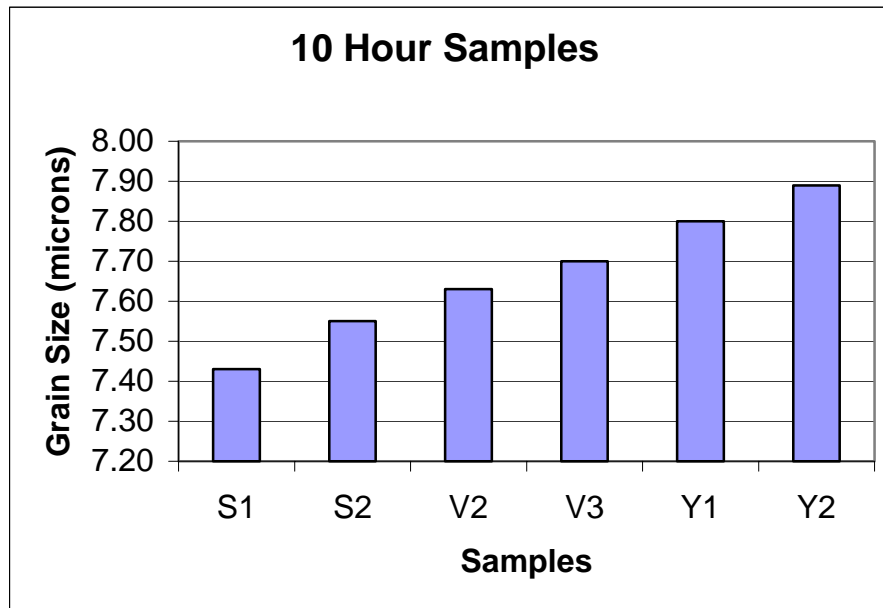


Figure 70. Grain Size Comparison for 10 hours, 80% CW, ReX.

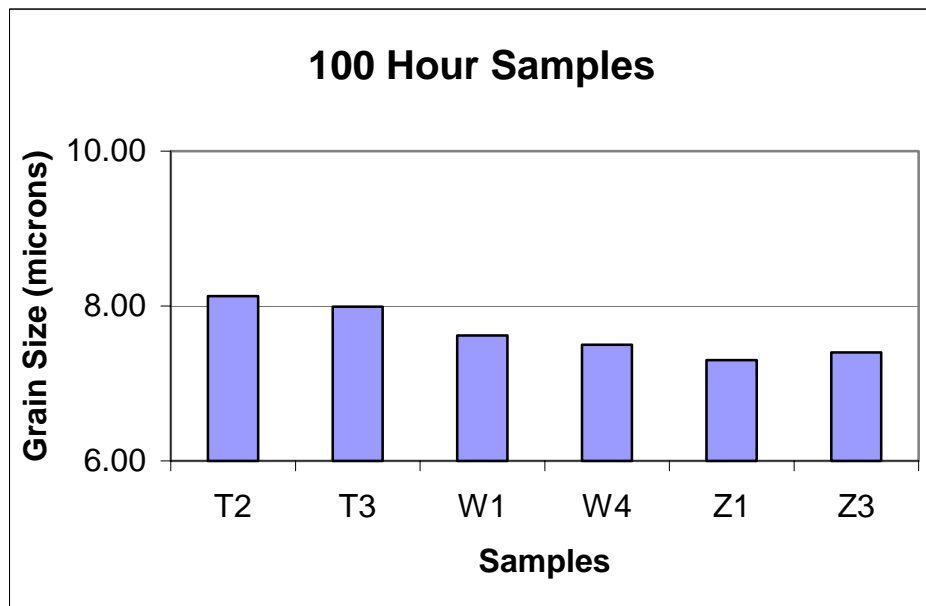


Figure 71. Grain Size Comparison for 100 hours, 80% CW, ReX.

THIS PAGE INTENTIONALLY LEFT BLANK

APPENDIX F. OIM GRAIN MAPS

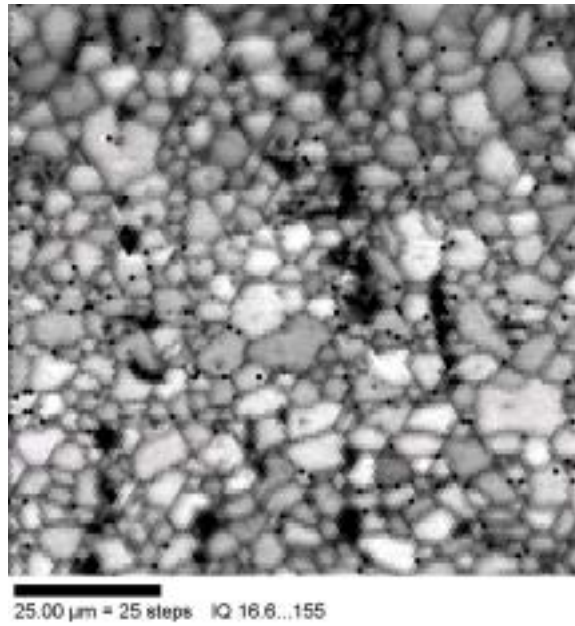


Figure 72. Sample S. Aged 500° C, 10 hours, 80% CW, ReX.

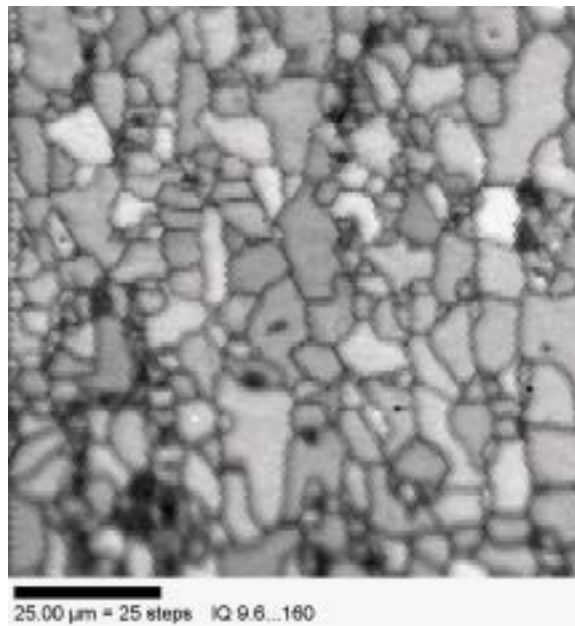


Figure 73. Sample T. Aged 500° C, 100 hours, 80% CW, ReX.

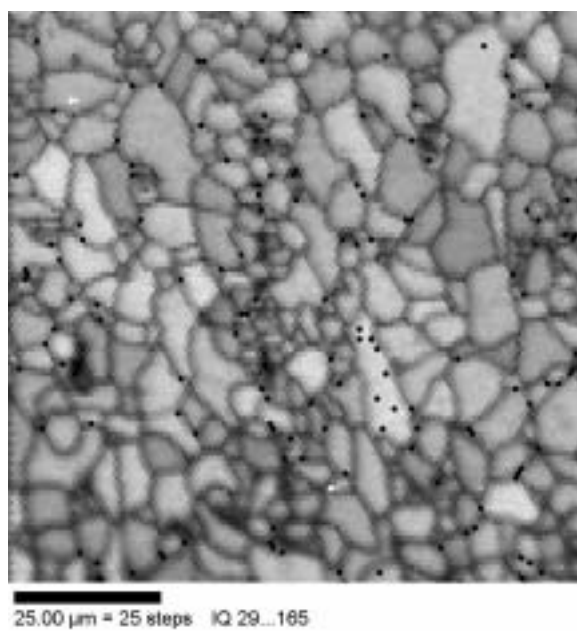


Figure 74. Sample U. Aged 525° C, 1 hour, 80% CW, ReX.

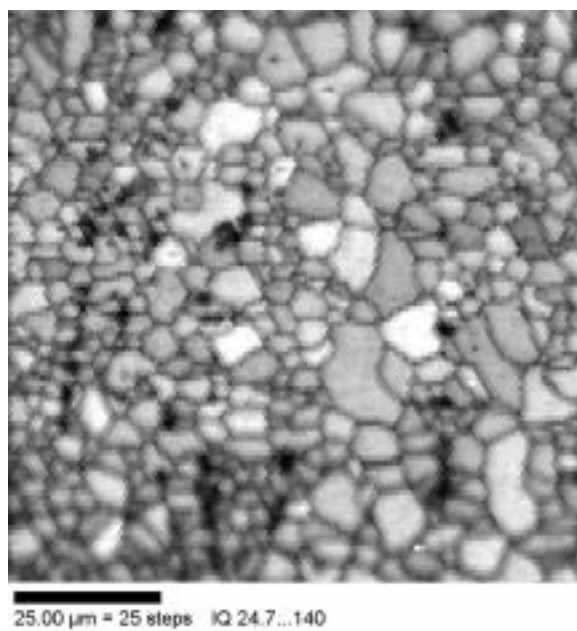


Figure 75. Sample V. Aged 525° C, 10 hours, 80% CW, ReX.

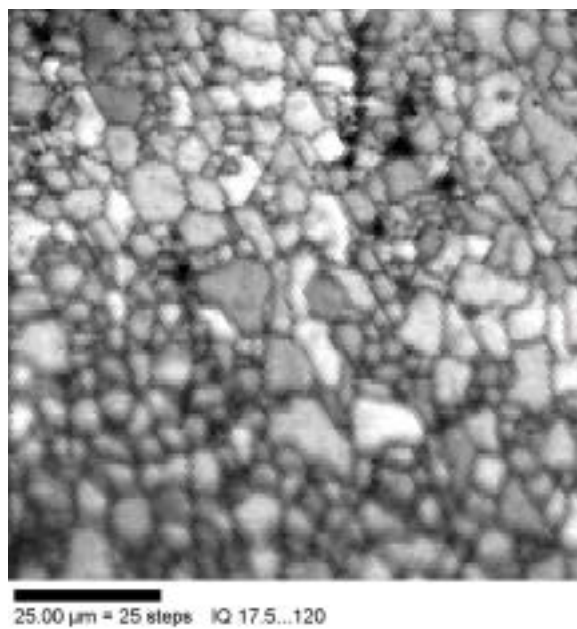


Figure 76. Sample W. Aged 525° C, 100 hours, 80% CW, ReX.

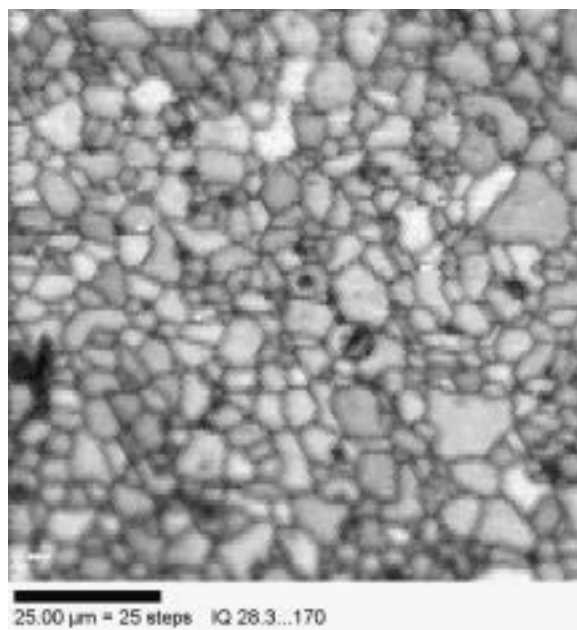


Figure 77. Sample X. Aged 550° C, 1 hour, 80% CW, ReX.

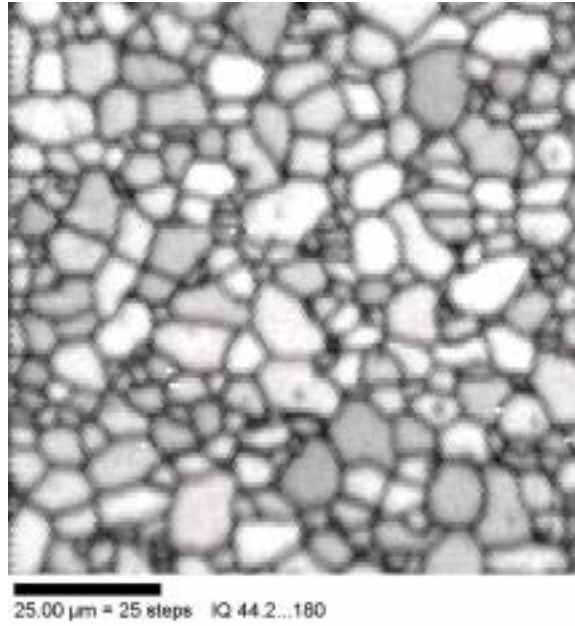


Figure 78. Sample Y. Aged 550° C, 10 hours, 80% CW, ReX.

APPENDIX G. OIM GRAIN SIZE CHARTS

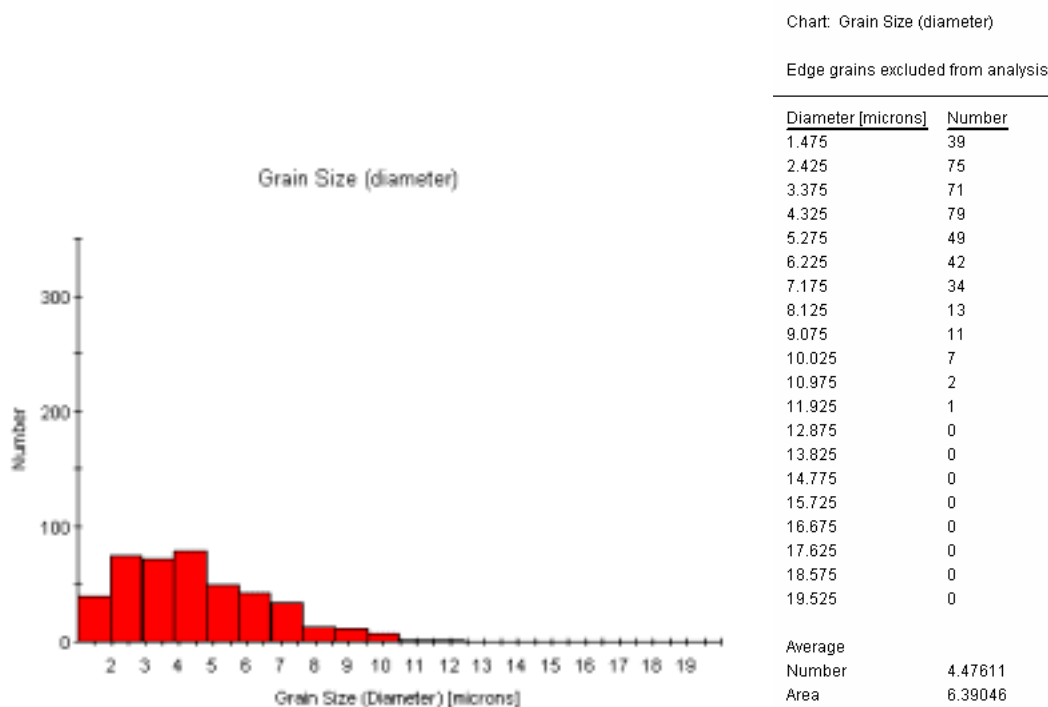


Figure 79. Sample S. Aged 500° C, 10 hours, 80% CW, ReX.

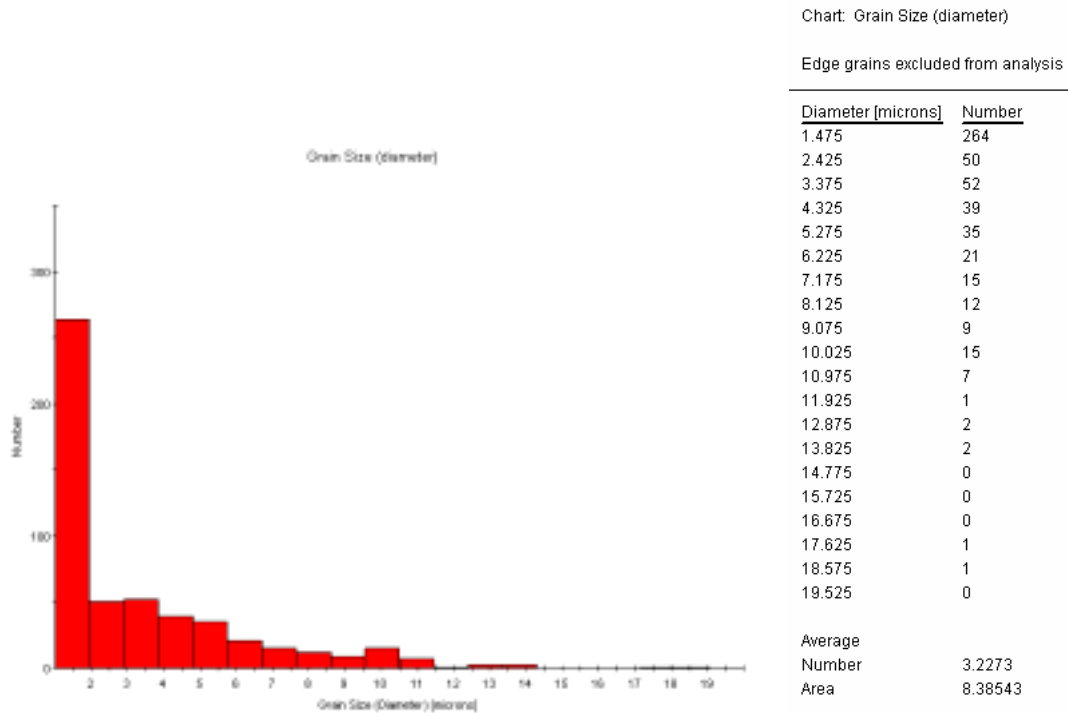


Figure 80. Sample T. Aged 500° C, 100 hours, 80% CW, ReX.

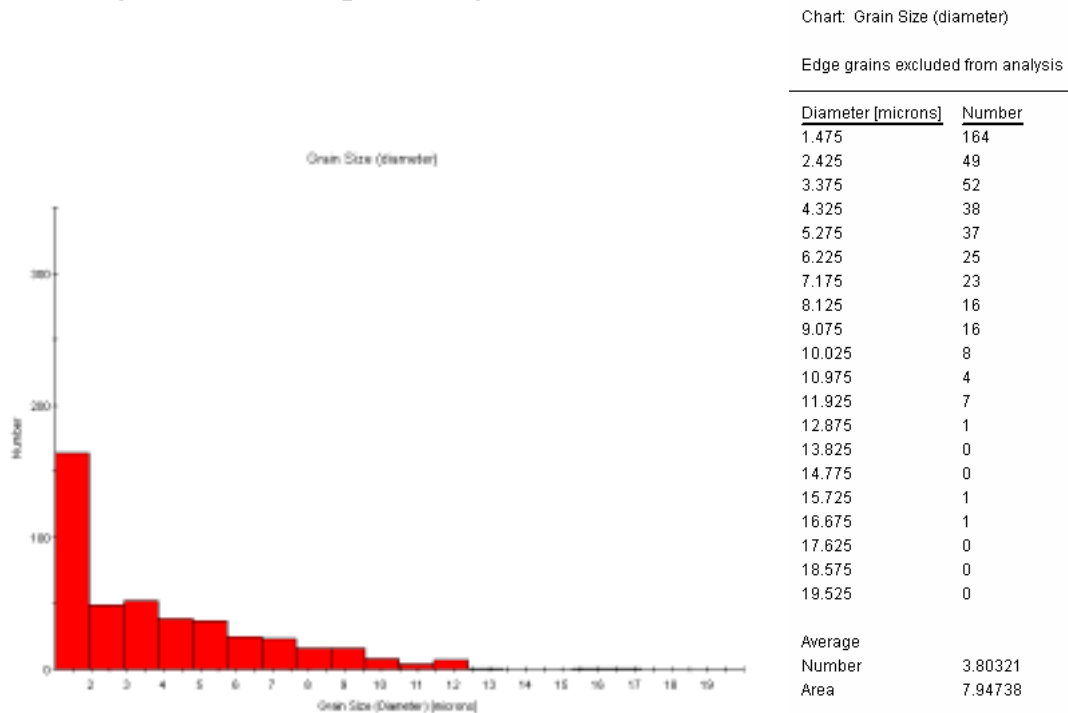


Figure 81. Sample U. Aged 525° C, 1 hour, 80% CW, ReX.

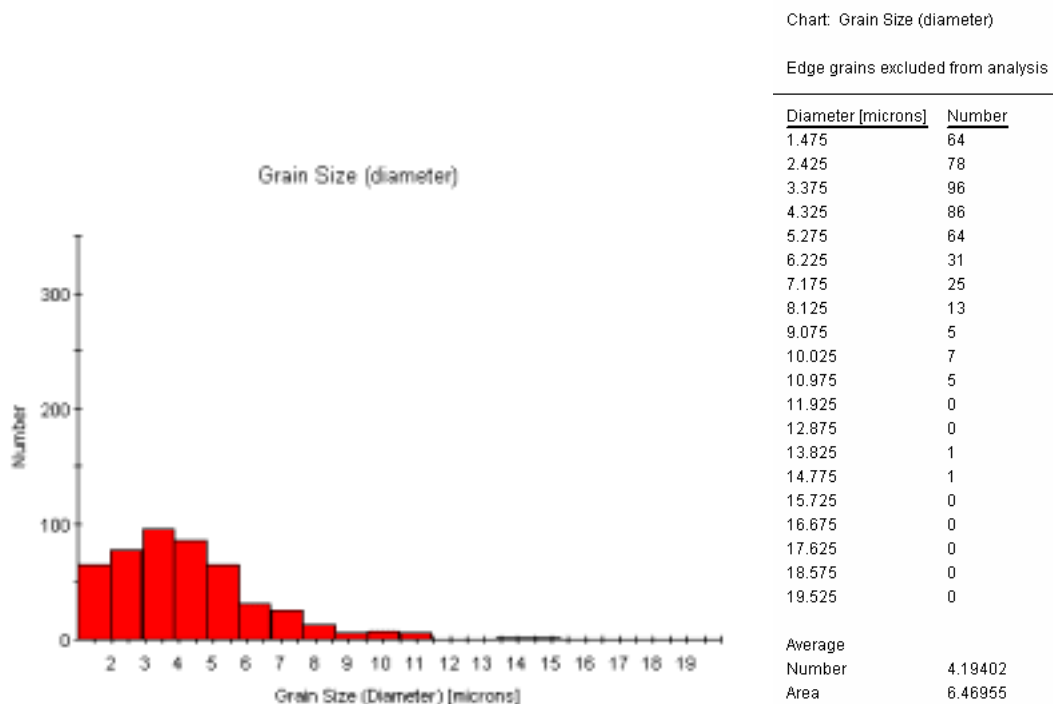


Figure 82. Sample V. Aged 525° C, 10 hours, 80% CW, ReX.

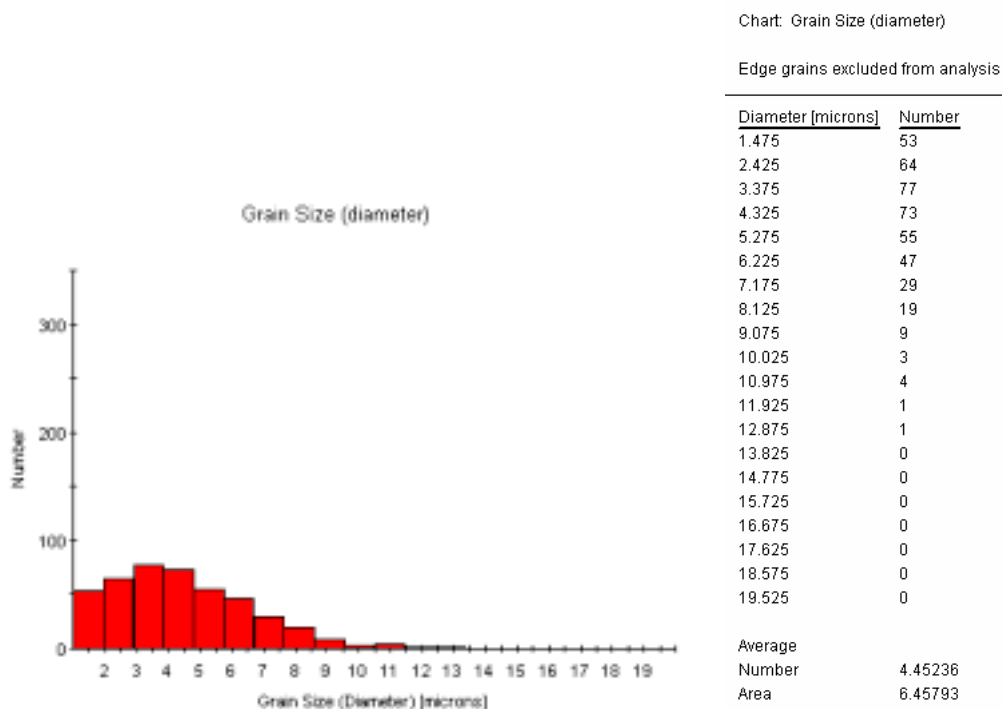


Figure 83. Sample W. Aged 525° C, 100 hours, 80% CW, ReX.

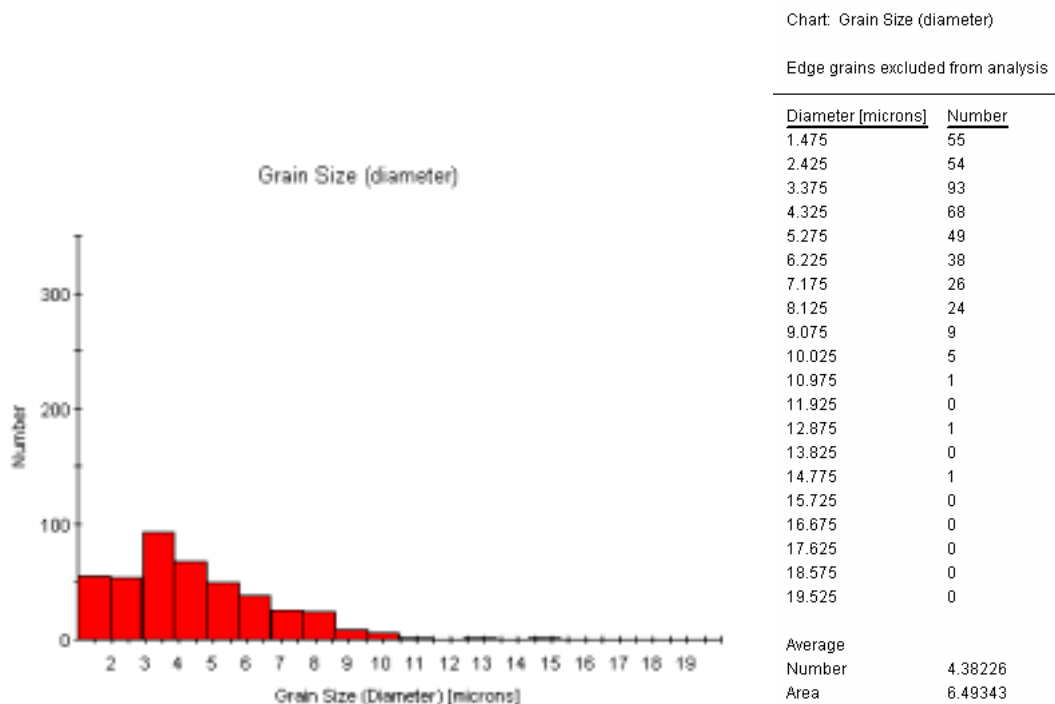


Figure 84. Sample X. Aged 550° C, 1 hour, 80% CW, ReX.

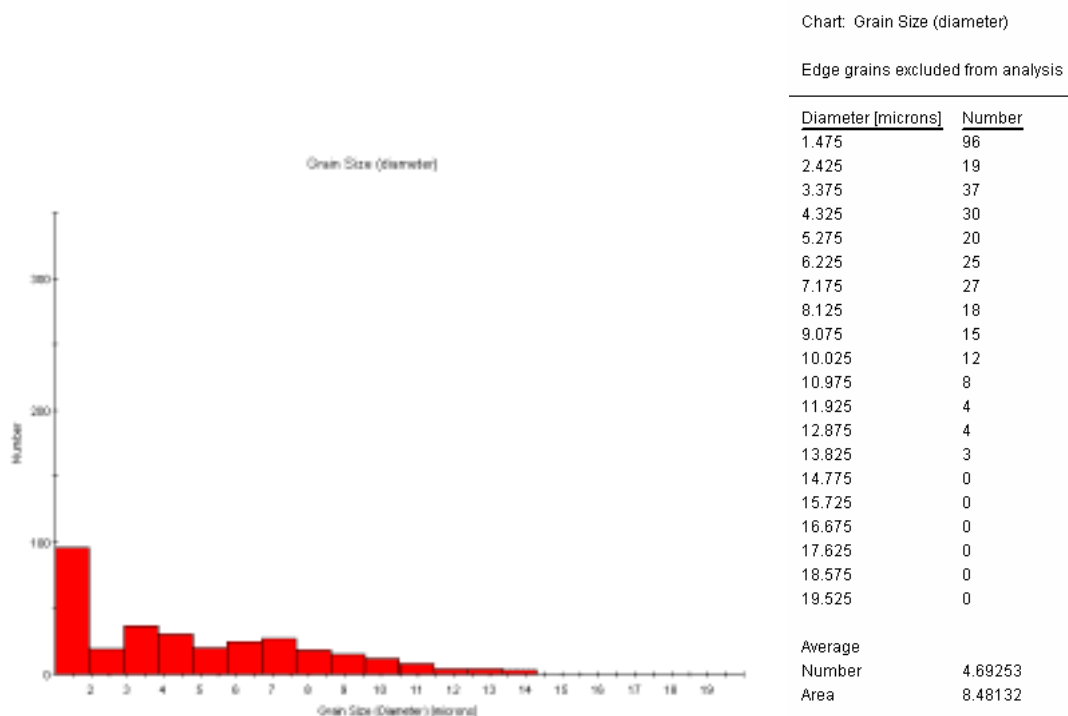


Figure 85. Sample Y. Aged 550° C, 10 hours, 80% CW, ReX.

LIST OF REFERENCES

1. Edington, Jeff W., "Microstructural Aspects of Superplasticity," *Metallurgical Transactions*, Vol. 13A, pp. 703-715, 1982.
2. Hamilton, C.H., "NATO/AGARD Lecture Series on Superplasticity," *Superplastic Sheet Forming*, Washington State University, pp. 2.1-2.24, 1987. Ashby, M. F., *Acta Met.*, v. 37, pp. 1273-1293, 1989.
3. Superform USA, www.superformusa.com, accessed August 2003
4. Ashby, M.F., *Acta Met.*, v. 37, pp. 1273-1293, 1989.
5. Nieh, T.G., Wadsworth, J., and Sherby, O.D., *Superplasticity in Metals and Ceramics*. Cambridge University Press, New York, 1997.
6. University of Liverpool. www.aluminum.matter.org, accessed August 2003
7. Ruano, O.A., Miller, A.K., and Sherby, O.D. *Mater. Sci. Eng.*, v. 51, p.9, 1981.
8. Sherby, O.D. and Ruano, O.A., *Superplastic Forming of Structure Alloys*, ed. N.E. Patton and C. H. Hamilton, TMS-AIME, New York,, 1982, p241.
9. Ruono, O.A. and Sherb, O.D., *Rev. Metal, Madrid*, v. 19, p. 261, 1983.
10. Gifkins, R. C., *Metall. Trans.*, v. 7a, p. 1225, 1976.
11. Ball, A. and Hutchison, M. M., *Met. Sci. J.*, v. 3, p.1, 1969.
12. Sherby, O.D. and Wadsworth, J., *Deformation Processing and Structure*, p.355, 1984.
13. Kokawa, H., Watanabe, T., and Karashima, S., *Phil. Mag. A*, v. 44, p. 1239, 1981.
14. Doherty, R.D., Hughes, D.A., Humphreys, F.J., Jonas, J.J., Juul Jensen, D., Kassner, M.E., King, W.E., McNelley, T.R., McQueen, H.J., and Rollett, A.D., "Current Issues in Recrystallization: A Review, " *Mater. Sci. Eng.*, v. A238, p. 219-274, 1997.
15. Waldman, J. Sulinski, H. and Markus, H., *Metall. Trans. A*, v. 5, p. 573, 1974.
16. Wert, J.A., Paton, N.E., Hamilton, C.H., and Mahoney, M.W. *Metallurgical Transactions*, v. 12a, p. 1267, 1981.
17. Humphreys, F. J., *Acta metal.*, v. 25, p. 1323, 1977.

18. ASM Handbook, 10th ed., Vol. 4, pp. 823-880, American Society for Metals, 1991.
19. Ashby, M.F., *Philos Metall.*, 21 (1970) 399.
20. Humphreys, F.J., "The Nucleation of Recrystallization of Second Phase Particles in Deformed Aluminum," *Acta Metallurgica*, Vol. 25, pp. 1323-1344, 1977.
21. McNelly, T.R., Crooks, R., Kalu, P.N., Rogers, S.A., "Precipitation and Recrystallization During Processing of a Superplastic Al-10Mg-0.1Zr Alloy," *Material Science and Engineering, A* 166, pp. 135-143, 1993.
22. Mathe, W., *Precipitate Coarsening During Oveaging of 2519 Al-Cu Alloy: Application to Superplastic Response*, Master's Thesis, Naval Postgraduate School, Monterey, CA, March 1992.
23. Bohman, S., *Thermomechanical Processing of Aluminum Alloy for Grain Refinement and Superplasticity*, Master's Thesis, Naval Postgraduate School, Monterey, CA, June 1992.
24. Dunlap, J., *Study of Refinement in Al Alloy 2519 Using Backscatter Orientation Contrast Made in the Scanning Electron Microscope*, Master's Thesis, Naval Postgraduate, Monterey, CA, December 1992.
25. Zohorsky, P., *Study of Precipitation and Recrystallization of Al Alloy 2519 by Backscattered Electron Imaging Methods*, Master's Thesis, Naval Postgraduate School, Monterey, CA, September 1993.
26. Peet, B., *Thermomechanical Processing of an Al 2519 Alloy, and an Assessment of Its Supeplastic Response*, Master's Thesis, Naval Postgraduate, Monterey, CA, March 1995.
27. Taleff, M. and McNelley, *Quarterly Report 12*, July 2003.
28. Cullity, B.D., *Elements of X-Ray Diffraction*, Addison-Wiley, 1978.
29. Randle, V., Ralph, B., and Dingley, D., "The Relationship Between Microtexture and Grain Bounary Parameters," *Acta Metallurgica*, Vol. 36, pp. 267-273, 1988.
30. Sherby, O.D. and Ruano, O.A., *Superplastic Forming of Structural Alloys*, ed. N.E. Patton and C.H. Hamilton, TMS-AIME, New York, 1982. p. 241.
31. Mackenzie, J. K., *Biometrika*, v. 45, p.229, 1958.
32. Kulas, M. A., *Elevated Temperature Forming Limits for AA5083 Aluminum Sheet*, GM summer project, University of Texas-Austin, 2003.

33. Devore, J.L., "Probability and Statistics for Engineering and the Sciences", Duxbury, 2000, p. 259-269.
34. ASM Handbook, 10th ed., Vol. 9, American Society for Metals, 1991.
35. Manfredi, Mark S., Computer Simulation of Random and Non-Random Second Phase Particle Distribution for Both Constant and Varying Particle Size, Master's Thesis, Naval Postgraduate School, Monterey, CA, September 1992.

THIS PAGE INTENTIONALLY LEFT BLANK

INITIAL DISTRIBUTION LIST

1. Defense Technical Information Center
Ft. Belvoir, VA
2. Dudley Knox Library
Naval Postgraduate School
Monterey, CA
3. Engineering and Technology Curricular Office, Code 34
Naval Postgraduate School
Monterey, CA
4. Department Chairman, Code ME/Mc
Naval Postgraduate School
Monterey, CA
5. Professor Terry McNelley, Code ME/Mc
Naval Postgraduate School
Monterey, CA
6. Professor Eric Taleff
The University of Texas at Austin
Austin, TX
7. Dr. Paul E. Krajewski
General Motors Corp.
Warren, MI
8. LT Ramiro E. Orellano, Jr.
Naval Postgraduate School
Monterey, CA